ScuDo
Scuola di Dottorato ~ Doctoral School
WHAT YOU ARE, TAKES YOU FAR

Doctoral Dissertation
Doctoral Program in Aerospace Engineering (30th Cycle)

# Self-excited vibrations controlled by damping at blade root joints of turbine disks

By

**Marco Lassalle**

******

**Supervisor(s):**
Prof. C. M. Firrone, Supervisor
Eng. P. Calza (PhD), Co-Supervisor

**Doctoral Examination Committee:**
Prof. L. Carassale, Referee, Università di Genova
Prof. L. Panning, Referee, Leibniz Hannover University

Politecnico di Torino
2018

# Declaration

I hereby declare that, the contents and organization of this dissertation constitute my own original work and does not compromise in any way the rights of third parties, including those relating to the security of personal data.

Marco Lassalle

2018

* This dissertation is presented in partial fulfillment of the requirements for the **Ph.D. degree** in the Graduate School of Politecnico di Torino (ScuDo).

*I would like to dedicate this thesis to my girlfriend Lorenza that supports and encourages me every days. It is also dedicated to my parents that love me and that are an example to follow.*

# Acknowledgments

To begin, I would like to express my gratitude to my advisor Prof. Christian M. Firrone for his continue support to my PhD activity. His guidance helped me to overcome the obstacles that I found in my research path and his passion for his job is a source of inspiration for me. In these three years I learned a lot from him, both in professional and in human fields and I hope to put this into practice in my life.

Secondly, I wish to thank GE Avio Aero for the opportunity to work with them on an extremely interesting topic. In particular I am thankful to Paolo Calza and Marco Moletta that have supported me in the PhD, helping me to understand the difference between the academic and industrial worlds. Thanks to them, I have the foundations to face the world of work.

I wish also to thank the engineers Francesco Poli and Lorenzo Pinelli of the Department of Industrial Engineering of University of Florence, travel friends in this three years of PhD in our two-week meetings. Their help was fundamental to understand the flutter phenomenon by aero-dynamic side and I am impressed by their knowledge.

Furthermore, I want to thank all the members of the LAQ AerMech Laboratory for the pleasant working environment and the time spent together.

Naturally, a particular thank goes to my parents that gave me the opportunity to study and that support my choices helping with their advice. Finally, a great thank goes to my girlfriend Lorenza that lights up my days with her presence.

# Abstract

The purpose of this thesis is the development of a methodology for the calculation of the non-linear aero-elastic behavior of a bladed disk to be used in an industrial process. The non-linear aero-elastic phenomena of a bladed disk for aeronautical applications are studied in the presence of friction contacts using a one-way coupled method. The calculation is performed using a method based on the Harmonic Balance Method (HBM) and the balance between the energy introduced by the unsteady aerodynamics on the blade airfoil and the dissipative energy. The HBM method is preferred with respect to the Direct Time Integration (DTI) for the strong reduction of the computation time that HBM technique allows in spite of an acceptable level of approximation when nonlinearities are introduced and the response is periodic.

The nonlinearity is introduced by purposely developed contact elements, placed at the blade root-joints, that produce additional stiffening and damping in the system due the introduction of contact stiffnesses and friction forces based on Coulomb's law. The aero-elastic equilibrium will be investigated through a Parameter variation of the Limit Cycle Oscillations (LCO) of the system using two different approaches: the physical approach and the modal approach. The effect of such variations will be highlighted in order to demonstrate what are the parameters that influence most the blade amplitude, both for the CFD and the mechanical simulation. In particular, the uncertainty in the definition of the contact parameters at the blade root will be taken into account by varying the friction coefficient and the normal force distribution on the blade root joint. Finally, the results of the analysis will be compared with the experimental data produced with a cold-flow test rig to verify if the sensitivity study associated to the simplifications introduced in the method are compatible with the measured response.

# Contents

# List of Figures

# List of Tables

# Chapter 1

# Introduction

## 1.1 ACARE goals 2020

Aviation contributes to climate change by producing about 2% of $CO_2$ and this threshold is expected to increase by up to 3% by 2050. The ACARE document "Vision 2020" drawn up at the beginning of the decade assigns ambitious goals especially to the propulsion system, hoping for a drastic improvement compared to the last generation of engines entered into service. These objectives can be only achieved through significant technological break-through for the most part of components of the propulsion system developing innovative and unconventional engine architectures.

The main ACARE 2020 guidelines are an important reference for guiding the development of the next generation of engines. The general goals for the aviation are reported in Figure 1.1, while Figure 1.2 shows the targets assigned to the propulsion system.

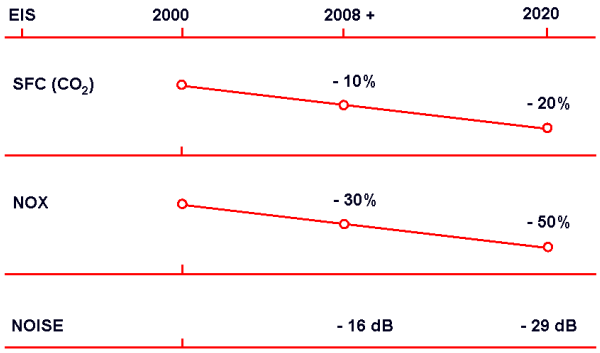


Figure 1.1: ACARE 2020 goals for 'green' engine

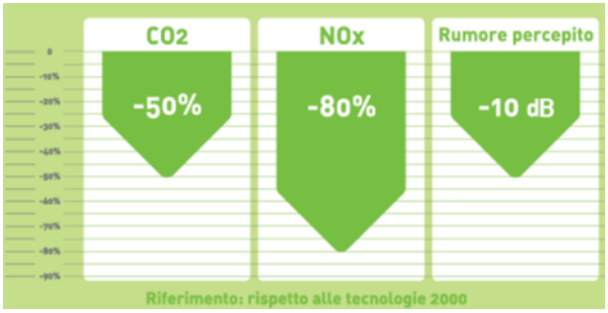


Figure 1.2: Percentage of ACARE 2020 goals assigned to the propulsion system

The first requirement for the 2020 is the reduction of 20% of $CO_2$. At propulsion system is assigned the largest share of the goal (50%) and therefore the effort in this direction is substantial. The main axes of technological development in this direction concern the development of new lightweight materials, the improvement of the performance of the components and thermodynamic cycle through the increase of by-pass ratio and compression ratio, the development of innovative architectures and the continuous development of optimized and integrated calculation systems that allow for a better understanding of the physical phenomena.

The second ACARE requirement concerns with the emissions of $NO_X$. The target for the propulsion system is to achieve an 80% reduction in emissions of these harmful compounds compared to in-service engines in 2000. This chemical compound has a significant environmental impact, both on the increase of "ozone-

hole" and on the health of people. However, the increase of by-pass ratio and compression ratio in the engine to reduce the $CO_2$ emissions produces an increase of $NO_X$ emission because higher combustion temperatures are required. To allow a reduction of $NO_X$, a new configuration of combustor has to be studied. This configuration provides a higher ratio between air and fuel to limit the peak temperature and the residence time at high temperatures.

The third ACARE requirement concerns the eco-propulsion and it is related to noise emissions. The goal is to reduce the noise generated by the entire aircraft by 50%. The target for the engine is the reduction of 10dB for the three main operative conditions (take-off, cruise and landing). The impact of this requirement on the engine is significant because the engine contributes to the maximum noise impact in the take-off phase, while in the landing phase contributes about 50% of the produced noise (the rest of noise pollution is mainly caused by the auxiliary support systems and landing gear). New solutions, such as passive noise control system, but also new soundproofing techniques of structures and engine cases, are being studied to satisfy this requirement.

## 1.2 Aero-elastic problem

The existence of reducing fuel consumption and pollution produced by air traffic has so led to the need to improve the various aircraft systems, including the propulsion system. This improvement, in the aircraft engine, has been translated by the engineers in the reduction of the weight and in the increase of the efficiency of the turbo-machinery. To realize that, high aspect ratio airfoils have been developed and this means to have airfoils more slender and thinner. The problem links to this new architecture of blades produced a reduction of the natural frequency of the blade and an increase of the amplitude of the vibrations with a consequent reduction of fatigue life and reliability of the component in the engine.

The vibrations in the turbo-machinery's turbine are mainly caused by two factors:

1. the excitation by time-varying forces loading turbines disks caused by the considerable non-uniformity of the flow of the hot gases that pass through the turbine blades and vanes;
2. the self-excitation that can occur in the absence of the excitation forces and when the unsteady work performed by the fluid exceeds the energy dissipated by the material and mechanical damping in the system (flutter).

The problem of the self-excited vibrations is one of the most important problems that has been studied by aircraft structural engineers in the last decades as soon as the weight reduction and flight performance had to be maximized. In the turbo-machinery area, turbine blade cascades underwent the same process in order to meet requirements of larger turbine disks (wider cross section) and higher rotation speed that means high aspect ratio and higher aerodynamic loads.

The best effort to predict and avoid the occurrence of this problem was given in the fluid-dynamic physics by means of CFD calculations through the solution of the Reynolds-Averaged Navier–Stokes equations (RANS) with different level of complexity (linearized form or more complex degree of coupling between blade motion and unsteady pressure distribution around the airfoil) based on the vibrations of a structural mode shape.

Usually the dynamics of the bladed disk is considered linear and the fluid-structure interaction is directly linked to the natural frequencies and normal mode shapes of the system. However, structural designers of aircraft engines have introduced nonlinearities in the bladed disk structure in terms of joints that act also as damping systems to reduce peak stress values during the vibratory phenomenon caused by the external excitation forces. These damping systems are usually joints geometrically optimized to produce friction forces to dissipate energy increasing the strength and life of the blade against High Cycle Fatigue failure. The major sources of friction damping (Figure 1.3) in the bladed disk turbine are attributable to the contact between adjacent blades connected by interference at the tip (shrouds - Figure 1.3a), mid-span airfoil (snubber - Figure 1.3b), underplatform dampers (Figure 1.3c) and the bladed disk interfaces (blade root joint - Figure 1.3d). The last joint is practically always included in the bladed disk design while the other types of joint may not be present.

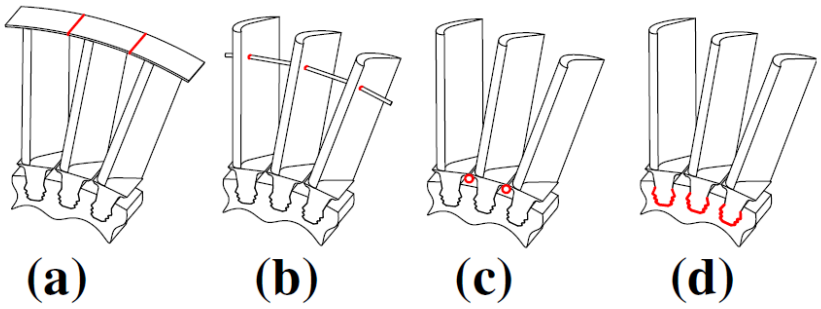


Figure 1.3: Common types of friction joints: (a) shrouds, (b) snubber, (c) underplatform damper and (d) root joints

As these friction contacts limit the vibrations due to the excitation forces, they can be used to suppress the unstable flutter vibrations to produce a periodic motion called Limit Cycle Oscillations (LCO). In this condition, the amplitude and the frequency of the LCO is determined by the equilibrium between the energy introduced in the system by the flow and the energy dissipated by the friction contacts (Figure 1.4).

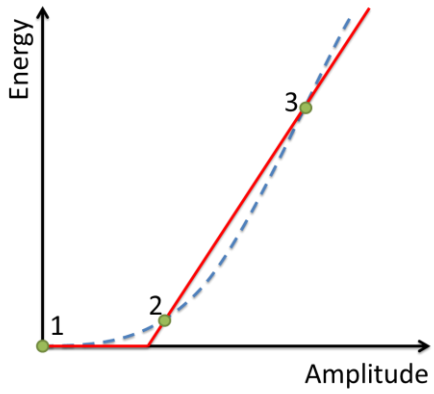


Figure 1.4 – Possible energy balance between the energy introduced by aerodynamics (blue dashed curve) and dissipative energy by friction (red solid curve)

The balance between the aerodynamic and dissipated energies provides in general three solutions: the solution 1 is the trivial solution where there is no exchange of energy because there is no vibration; besides, this is an unstable solution because any small perturbation of the system moves the system away from 1 and towards

solution 2. The solution 2 is the stable solution of the system and it will be called the LCO solution; in fact, any perturbation from 2 limited between the solution 1 and the solution 3 does not change the final equilibrium '2'. The solution 3 is an unstable solution and represents the stable limit of the system because any perturbations bigger than this limit produces ineffective damped and uncontrolled self-excited vibrations.

## 1.3 Thesis objectives and outline

The work presented in this thesis has been developed in an industrial context that is represented by GE Avio Aero. In particular, GE Avio Aero aimed at developing a method for the calculation of the non-linear aero-elastic behavior of a bladed disk in the presence of friction contacts at a blade root-joint. Consequently, the method has been developed to be implemented in the industrial process and so changing the current design process. In fact, the current design process does not accept a blade array with a level of instability bigger than a fixed limit determined by the intrinsic material damping and this has a great impact on the performance, but also on the time and cost of design because an unstable blade should be modified or redesigned. This methodology was thought to change this practice and apply a design for percentage endurance limit. This is possible because the method allows to quantify the amplitude and the frequency of vibration of an unstable bladed disk for a given nodal diameter.

The main aim of the method shown in Figure 1.5 is the reduction of the time for the aero-elastic calculation in the presence of non-linearities such as the friction joints. This method is a structural uncoupled method where the equations of motion are solved together to the equation of energy balance in the frequency domain, while the aero-elastic coefficients are pre-computed using a linearized solver of the RANS equations (the aero-dynamic solver is a tool of GE Avio Aero) and so they became the input parameters for the bladed disk equations of motion in the aero-elastic code.

The reduction of the computational cost is obtained using two approaches widely used in the forced response calculation of components with friction contact:

- Reduced Order Model (ROM);
- Harmonic Balance Method (HBM).

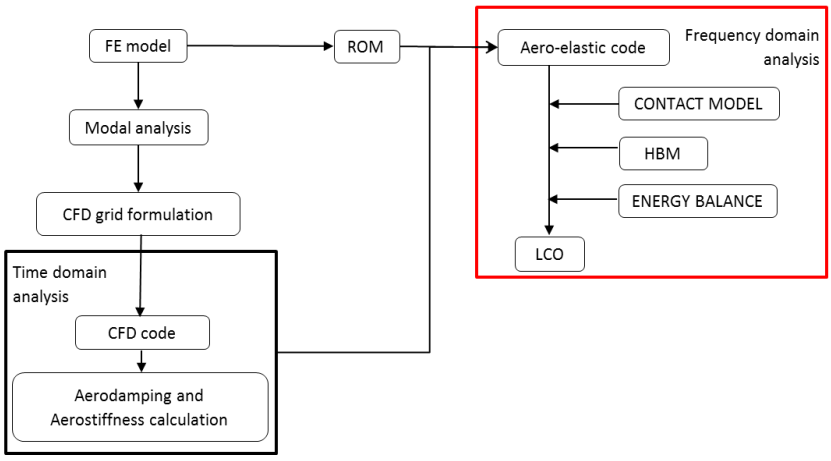


Figure 1.5: block diagram of the developed method

The present dissertation is structured as follows:

- *Chapter 2* introduces the vibrations on the turbo-machinery in terms of synchronous and asynchronous vibrations. The aero-elastic phenomena of forced response and flutter response are described and a description of the methods developed to study these dynamic behaviors is given.
- *Chapter 3* introduces the numerical methods that will be used to develop a methodology for the flutter calculation. These methods, that have been deeply studied by different authors, try to reduce and simplify the system saving the computation time. Since these numerical methods have been widely used in the scientific literature and have been applied in this study, a brief description of them and the mathematical modelling is presented for completeness of information.
- *Chapter 4* introduces the structural aero-elastic method and its application on lumped parameter models. In the first part of the chapter the study of the flutter phenomenon proposed by Griffin and Sinha in 1983 is first analyzed and replicated because this study is considered as the reference point for the flutter study on blades; then, a proper methodology to study the flutter phenomena on different systems is presented and a Parameter variation is performed to understand the main parameters acting on the flutter phenomenon.
- *Chapter 5* extends the developed methodology for a lumped parameter models to study the flutter behavior of a bladed disk. Two approaches are presented: a physical approach that uses the reduced mass and stiffness

matrices, and a modal approach that uses a modal base extracted by software FEM (Ansys). Different parameter variations are performed using the two approaches to study the flutter response on a bladed disk. Some modifications of the developed methodology are introduced to solve problem arising especially for the modal approach.

- *Chapter 6* presents a comparison between the numerical results and the experimental data obtained on the bladed disk of the project *Great-2020* funded by *Regione Piemonte*. The test article and the cold flow test rig and test campaign are presented, then the comparison is performed using appropriate distributions of normal forces on the contact surfaces. Two distributions are calculated through a non-linear static analysis at FEM where two different load conditions are applied. Finally, the effect of the geometric tolerances on the contact surfaces are considered and a new numerical-experimental comparison is performed.
- *Chapter 7* summarizes overall conclusions and fulfilled tasks. Possible future developments of this research are also presented.

# Chapter 2

# Vibrations of turbo-machinery

The trend of reducing fuel consumption and pollution produced by air traffic has led to the need to improve the turbo-machineries up to their structural mechanical limits. This means a reduction of the weight and an increase of the efficient of the aircraft engines that means high mechanical dynamic stress during operations (low natural frequency and high amplitude of vibration).

The most dangerous types of vibrations which occur inside a turbo-machinery assembly (see Figure 2.1) are resonant oscillations, characterized by frequencies that are multiples of the shaft's rotation speed (synchronous vibrations), and flutter vibrations, generally occurring at a non-integral order of frequency (non-synchronous vibrations). Flutter concerns aero-elastic instability problems that, if not considered during the design phase, can induce unexpected and very high stresses both on blades and on the entire assembly until serious high cycle fatigue (HCF) failure occurs.

For these two types of vibrations, there are two main fields of dynamic investigations in the turbo-machinery:

- forced response (synchronous vibrations);
- flutter analysis (non-synchronous vibrations).

In the first analysis, flow disturbances generated by upstream and downstream stages during the rotation motion are considered. Their frequencies are related to the number of revolutions per minute of the engine. In the second analysis, flutter

instabilities occur as self-excited oscillations due to an exchange of energy between the fluid and the structure. Usually in the flutter analysis the external forces are not considered since it is assumed that the vibrations due to flutter are much higher than the excitation produced by the aeromechanical excitation.

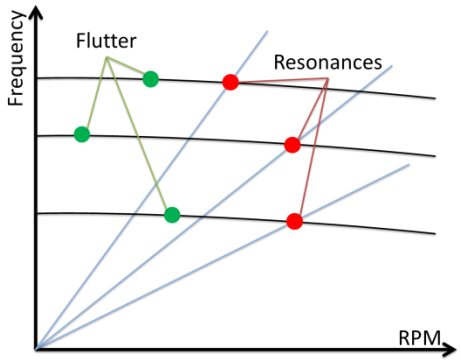


Figure 2.1: qualitative representation of dangerous vibration on the Campbell diagram of a LP turbine

It is possible to perform different types of analysis depending if the non-linearity of the structure and/or of the flow is considered. That is:

1. forced response:
    (a) linear
    (b) non-linear
2. flutter:
    (a) linear
    (b) non-linear

In the forced response calculation the linear analysis starts with the modal analysis of the structure (eigenvalues and eigenvectors calculation) and calculation is made in the simplest way using the modal superposition method, while in the non-linear analysis structural and mechanical non-linearities are included, such as the presence of friction dampers (under-platform dampers, snubbers tip or part-span shrouds, snubbers, blade root joints, ring dampers). In this case, iterative procedures are necessary to achieve the convergence of the solution of a dynamic equilibrium. Different Reduced Order techniques are used to accelerate the calculation with an acceptable approximation of the results. Instead, in a flutter investigation the non-linearities can reside both in the structure (friction dampers in this case) and in the flow (turbulence, transonic field, shock waves, etc.).

Besides, the fluid-structure interaction (FSI) can be treated with different points of view:

1. one-way coupled methods:
    a. in the aerodynamic field;
    b. in the structural field;
2. two-way coupled methods.

These two types of coupling methods indicate how the FSI is made. The one-way coupled methods focus their attention in one of the two fields (the aerodynamic or the structural fields), where they perform the FSI calculation. Instead, the results of the other field are only used as input to allow calculation. For example, the aero-elastic calculation in the aerodynamic field is made through the solution of the RANS equations on the base of the vibration of a structural mode shape that is separately calculated with a modal analysis at FEM. However, there is not a feedback between the aerodynamic field and the structural field, i.e. the structural results are not influenced by the results of CFD (see Figure 2.2a). A similar thing happens for the one-way coupled methods in the structural field: the flutter analysis is performed in the structural filed, while the aerodynamic results are only an input for the calculation of the flutter response of the blade (see Figure 2.2b). Instead, the two-way coupled methods present a mutual interaction between the two fields (see Figure 2.2c) and give more accurate results, but they are computational slow. On the contrary, the one-way coupled methods are faster, but they give a higher approximation of the solution of the problem to be discussed.

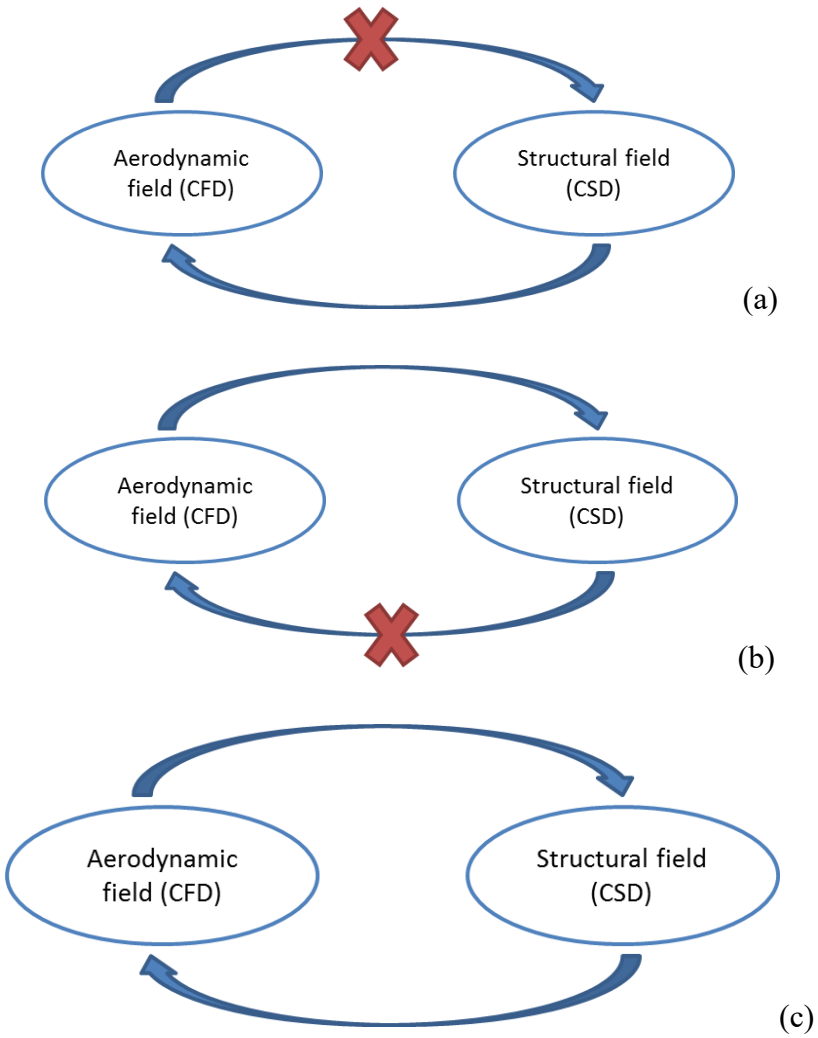


Figure 2.2: (a) one-way coupled methods in the aerodynamic field, (b) one-way coupled methods in the structural field and (c) two-way coupled methods

Finally, the calculation of the forced response and the calculation at flutter can follow two main approaches:

- frequency domain approach;
- time domain approach.

The frequency domain approach is computational fast because the equation of motion is algebraic and not differential, but it gives a higher approximation of the solution of the problem. It assumes a steady, periodical, harmonic motion of the blades with a constant phase shift, called Inter-Blade Phase Angle (IBPA) by

applying the Fourier transformation to time depending variables (displacements and forces). The time domain approach is slow because there is a direct time integration of the equations of motion and consequently the blades can have a non-harmonic motion. In general, it gives a detailed evolution and solution of the problem.

## 2.1 Aero-elasticity

Aero-elasticity is the study of the interaction between mechanical and aerodynamic forces acting on a body. These phenomena could be static or dynamic, and in this case the inertial forces should be included. The aero-elastic problems principally born in the aeronautic field, but they are present also in the mechanical and civil fields (a very popular example is the disaster of the *Takoma* bridge).

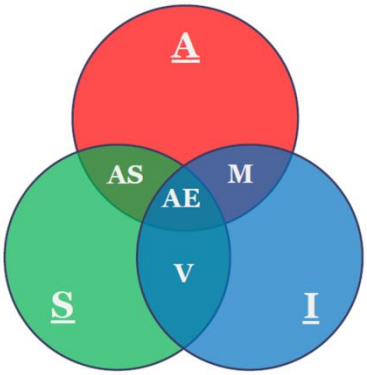


Figure 2.3: Collar diagram of aero-elasticity

Collar defined a triangle of forces [1], shown in Figure 2.3, in which inertia (I), elastic (S), and aerodynamic (A) forces form a triangle whose vertices represent the respective disciplines. From the intersection of these disciplines four new fields of study were born:

- vibration mechanics (V): intersection of elastic and inertial fields;
- flight mechanics (M): intersection of aero-dynamic and inertial fields;
- static aero-elasticity (AS): intersection of elastic and aero-dynamic fields;
- dynamic aero-elasticity (AE): intersection of elastic, inertial and aero-dynamic fields.

In turbo-machinery, the aero-elastic problems are very important since blade arrays are continuously subjected to significant aero-dynamic and centrifugal loads, while the gravitational forces contribute to the equilibrium of blade-rows, but these are generally negligible. As said, the main aero-elastic phenomena of interest in turbo-machinery are the forced response and the flutter response that will be presented in more detail below.

### 2.1.1 Forced response

Forced response is a very common vibration problem that is considered during the development phase of a new gas turbine to prevent blade failures due to HCF. Although the sources of the dynamic excitation producing vibrations of the whole structure are many, the time-varying forces loading gas turbines of aeronautic engines are caused by the considerable non-uniformity of the flow of the hot gases that pass through the turbine blades [2]. In a regular operating condition, the aerodynamic excitation pattern loading the blade array can be represented as a combination of multiple excitations having a harmonic pattern in space along the circumferential direction that travel with respect to the bladed disk. This cyclic pattern of excitation is produced by the flow that passes through stator and rotor stages alternating along the axial direction (Figure 2.4). Thus, the circumference can be divided into an integer number of wavelengths for each travelling harmonic force that is called Engine Order (EO) [3]. The bladed disk is therefore subjected to a wide excitation spectrum and multiple excitations at resonance condition may occur for a given rotating speed of the rotor. The same issue occurs for stator vane segments as well where travelling forces are generated by the wakes of front and aft-rotating disks.

The EO is defined as the ratio between the frequency of the excitation force and the rotating frequency of the disk. The excitation force on a bladed disk can be static or rotating depending on the reference system that is used, fixed in the first case or rotating with the disk in the second case. In case of static force, the bladed disk is potentially excited at resonance when the frequency of the forcing is equal to the natural frequency of a mode of the system. Instead, in case of rotating excitation force, a bladed disk is excited by two different rotating forces corresponding to two different EO: one agrees with the rotation speed of the disk (forward travelling excitation), the other opposite to the rotation of the disk (backward travelling force). The two travelling forces rotate with different angular velocities: lower for the backward excitation and higher for the forward excitation.

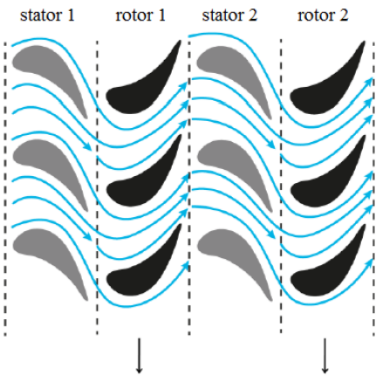


Figure 2.4: Stator and rotor bladed disks of an axial turbo-machine.

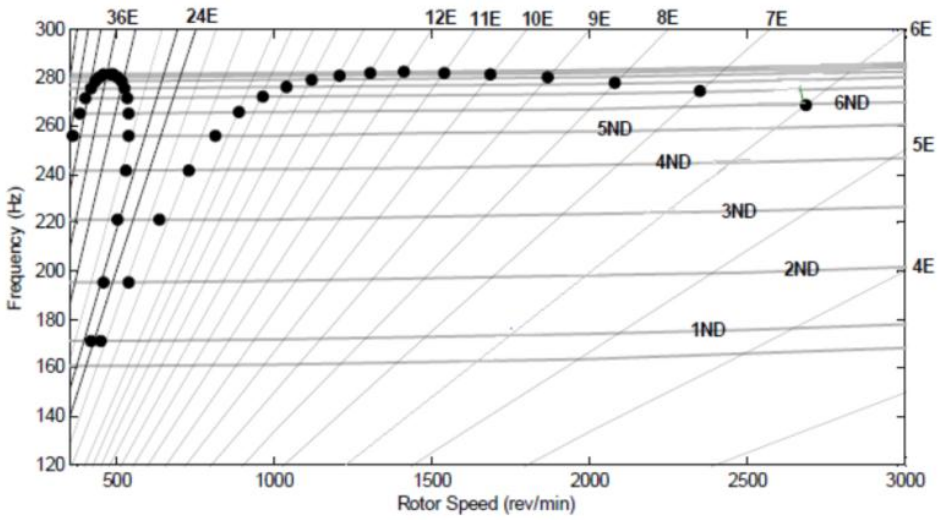


Figure 2.5: Campbell diagram of a bladed disk with 24 fundamental sectors

The first work on the forced response of bladed disks that left an important tool to study and identify the critical resonance conditions of the turbo-machinery was done by Wilfred Campbell [4, 5]. The Campbell diagram (Figure 2.1 and 2.5) is a plot where the trends of the natural frequencies of the bladed disk (horizontal lines) and the trends of the frequencies of the excitation force (inclined lines) for different EO are reported (the higher the EO, the steeper the line in a proportional way), both depending on the angular velocity of the disk. In Figure 2.5, some intersection points between the trends of the natural frequencies and the trends of

the excitation frequencies are marked with a black dot. These points represent an effective critical resonant condition, i.e. a travelling force with defined EO can excite the rotor at resonant condition for particular mode shapes and a particular rotating speed. In general, the resonance condition on Campbell diagram can be identified by the following expression:

$$EO = mN \pm ND \quad with \ \forall m \in \mathbb{N} \tag{2.1}$$

where *ND* is the nodal diameter and *N* is the number of blades. The nodal diameter is an index that indicates the number of lines crossing the center of the disk that have modal displacements equal to zero. If *m=0*, the EO excites the correspondent ND due to the non-orthogonality between EO and ND, while for *m* bigger than 0 the resonance conditions is due to spatial aliasing. In fact, the blade row is a discrete system that samples the shape of the excitation force in a finite number of equally spaced points corresponding to the blades location.

Two types of forced response problems can be distinguished thanks to the frequency of the exciting forces:

- high engine order forced response (HEO);
- low engine order forced response (LEO).

The first type is the classical forced response associated to the interactions given by the stator and more in general by the blade arrays close to the bladed disk that is studied and it is due to the excitation forces generated by the rotation of the bladed disk through a non-uniform pressure field. The strength of the excitation varies periodically with the angular position of the blades. The unsteady disturbances in the flow field due to the relative motion of stator and rotor stages can be divided in two categories:

- Potential stator-rotor interaction: the flow disturbance is caused by an unsteady forcing due to the non-uniform distribution of pressure acting in the stator and rotor blade rows [6];
- Wake-rotor interaction: the wakes shedded by the stator blades are in general steady in the stator reference frame, but become unsteady in the rotor reference frame and this produces that the periodicity of forcing depends on the number of stator blades [7].

The second type of forced response is the low engine order excitation [8, 9] that occurs at high speed and temperature and it is probably due to some loss of symmetry in the flow features. It is related to the pressure distribution in the region between stator and rotor stages where the unsteady aerodynamic force can be generated and it is composed by low-order harmonics that excite modes at low-order nodal diameter.

### 2.1.2 Flutter analysis

Flutter oscillations are today a phenomenon among those of major concern for turbo-machinery designers. Flutter is an instability problem in which vibrations are self-excited by the motion itself of the blades through the interaction among the flow, the elastic response and the inertial forces. Aerodynamic forces continuously introduce energy in the structure and stresses grow after each vibration cycle reducing the fatigue life and the reliability of the structure. As said in the introduction of this chapter, the flutter phenomenon belongs to the family of asynchronous problems, i.e. it is not directly caused by the interaction between upstream and downstream blade-rows whose frequency is an integer number of times the rotating frequency of the disk.

The first signals of presence of self-excited oscillations inside turbo-machinery appeared towards the mid and the end of 1940s and they are reported by Fransson in [10]. However, it is difficult to find information about aero-elastic failures in turbo-machinery, since they are considered as negative advertising and are not widely discussed, due to a strong competition among different companies producing engines. Besides, due to the complexity of aerodynamic forces and structural vibrations, it is difficult to distinguish interactions between blade rows and wakes (i.e. forced response) and self-excited vibrations (i.e. flutter). Same cases of flutter failures have been found in 1991 in the fourth stage turbine blades of the Pratt & Whitney F-100 engine produced for the McDonnell Douglas F-15 aircraft; in the third compressor stage of the Volvo engine developed for the Swedish SAAB JAS aircraft and in the first stage fan blades of the General Electric F-101 installed on the B-1B bomber.

In general, four types of flutter can be found in the turbo-machinery depending on the operating region and flow conditions. These four flutter regions are reported onto a compressor map (Figure 2.6) in which the engine characteristic lines are plotted in a pressure ratio against flow mass rate.

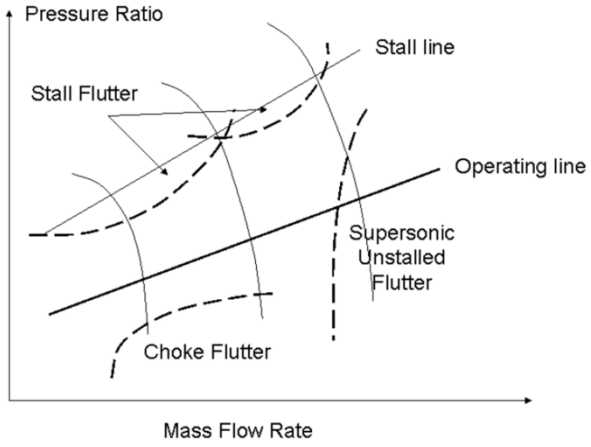


Figure 2.6: Compressor map showing the four flutter regions

This four types of flutter are:

- Classical flutter: this flutter can occur when the flow is attached to the blade with no separation and a phase lag between the aero-dynamic forces and the amplitudes of vibration exists. Three possible situations can be presented: (1) the flow introduces energy in a not damped structure producing uncontrolled oscillations (unstable condition); (2) the flow absorbs energy from the structure and this produces an always stable operative condition; (3) the energy introduced by the flow is balance by the dissipative energy of the structure producing Limit Cycle Oscillations (LCO).
- Stall flutter: the operative conditions are close to the stall line on the compressor map. This flutter is typical of the first stage fan blades and it is due to an increase of incidence of the blade that can produce the flow separation, which seems to play an essential part of the blade flutter mechanism [11].
- Supersonic unstalled flutter: this flutter occurs when the flow acting on the blades is supersonic, but it is not stalled and there is not separation. The induced vibrations usually involve the torsional mode of the bladed disk. This flutter is typical of the shrouded blades of the fans.
- Choke flutter: the operative conditions are close to the choke line on the compressor map. This flutter is typical of the last compressor stages and it is due to a decrease of incidence of the blade that can produce a flow

separation through a shock wave that may excite the vibrational modes of a blade [12].

The aero-elastic interactions occurring inside a turbo-machinery environment are a complex phenomenon that should be prevented. To build a reliable flutter prognostic tool is necessary to keep under control a lot of flow and structural parameters. An essential list of the parameters that influence the aero-elastic aspects of blade vibration is given by Srinivasan in [13]. The most important parameters are reported below:

- Reduced frequency (*k*): this parameter can be interpreted as the ratio between the time taken for a fluid particle to flow past the length of a semi-chord and the time taken for the airfoil to execute one cycle of vibration (from [13]). The reduced frequency can be defined as:

  $$k = \frac{b\omega}{V} \tag{2.2}$$

  where $b$ is the semi-chord, $\omega$ is the pulsation of vibration and $V$ is the velocity of air relative to the blade. Another interpretation of reduced frequency was given by Platzer and Carta in [14] as the ratio of a circumference of a circle of radius $b$ and the wavelength of the wake $\lambda$ (equation (2.3) and Figure 2.7). From equation (2.3) it is possible to see that the bigger the wavelength $\lambda$, the smaller the reduced frequency $k$. For small values of the reduced frequency, the flow is characterized by quasi-steady conditions, while, on the contrary, the ratio of frequency changes for higher values of $k$.

  $$k = \frac{2b\pi}{\lambda} \tag{2.3}$$

- Inter-blade phase angle (*IBPA*): this parameter can be interpreted as the phase relationship that represents the motion difference of a blade with respect to the adjacent blades. The *IBPA* is a characteristic parameter of structures that present a cyclic symmetry assembly such as the turbo-machinery where every blade of a stage is subjected to the same amplitude of vibration, but at different time instants. The *IBPA* can be defined as:

  $$IBPA = 2\pi ND/N \tag{2.4}$$

  where *ND* is the nodal diameter and *N* is the number of sectors.

- Mistuning: the mistuning can be natural/intrinsic (due to small differences between the blades with respect to the nominal geometry, material properties inhomogeneity, contact interfaces of joints, wear in service) or purposely induced (alternating mistuning where a blade cascade is made of two sets of blades assembled in a 01010… pattern for example). It breaks the cyclic symmetry that nominally characterizes the turbo-machinery and prevents the flutter onset. This is possible because a significant perturbation of the blade response in terms of amplitude uniformity in the blade cascade and phase shift between a blade and its neighbors can produce a change of the gas flow effect on the blade and, as a consequence, on the value of the aerodynamic damping [15-17].


Figure 2.7: reduced frequency interpretation given by Platzer and Carta in [14]

#### *2.1.2.1 Modeling aero-elastic phenomena*

The problem of the self-excited vibrations is one of the most important problems that has been studied by aircraft structural engineers in the last decades as soon as the weight reduction and flight performance increase. Aero-elasticity is a topic addressed by different authors, see for example [18-20]. The most effort to predict the occurrence of this problem was given in the fluid-dynamic field by means of CFD calculations ([21-24]) through the solution of the Reynolds-Averaged Navier–Stokes equations (RANS) with different level of complexity. The developed methods can be divided by the coupling with the structure in:

- Semi-uncoupled (or one-way coupled) methods: they take into account the influence of blade vibration on the flow, but not vice-versa;
- Fully coupled (or two-way coupled) methods: they take into account the interaction between fluid and structure and vice-versa;

and by the level of approximation:

- Linearized methods: the RANS equation are linearized and splitted into a steady part and a perturbation part;
- Non-linear methods: simulate unsteady flows around vibrating blades, in this case the equations to solve are the unsteady RANS equations (URANS).

All these approaches allow to calculate the values of the aerodynamic factors of damping and stiffness associated to a chosen mode shape of a blade at the variation of IBPA.

The first effort to model and predict was developed at the beginning of the 1970s. These methods were based on a linear approach where every equation was linearized [25-26]. Since the 1990s new linearized methods have been developed that include a non-linear steady solution of the flow. These new methods have been solved both in time domain ([27-31]) and in frequency domain ([32-34]).

The linearized methods are usually associated with a semi-coupled approach; this means that the blade vibrations derived from modal analysis whose results become the input data for the aero-elastic calculations. The oscillations, to be used in linearized method, should have determined characteristics:

- Infinitesimal and periodic amplitude of vibrations (hypothesis of small perturbation);
- Only one frequency (mono-harmonic perturbation);
- Constant phase delay between neighbor blades (i.e. only one IBPA for each simulation).

With these characteristics it is possible to define a harmonic perturbation of mesh of the fluid domain:

$$x' = x + \mathcal{R}e(\bar{x}_\delta e^{j\omega t})$$

$$y' = y + \mathcal{R}e(\bar{y}_\delta e^{j\omega t}) \tag{2.5}$$

$$z' = z + \mathcal{R}e(\bar{z}_\delta e^{j\omega t})$$

where $\omega$ is the natural frequency of the blade vibration. The governing equation for the fluid motion is:

$$\frac{\partial U\prime}{\partial t\prime} + \frac{\partial F\prime_x}{\partial x\prime} + \frac{\partial F\prime_y}{\partial y\prime} + \frac{\partial F\prime_z}{\partial z\prime} = Q' \tag{2.6}$$

where *U'* is the vector of the conservative variables (mass, momentum, energy and turbulence quantities when presented), *Q'* is the vector of the source terms and *F'* is the matrix of the flux functions in the three directions.

In accordance with equations (2.5), the vector of conservative variables *U'* is written as a sum of their mean values and their small perturbations:

$$U' = U + \mathcal{R}e(\overline{U}_\delta e^{j\omega t}) \tag{2.7}$$

Equations (2.5) and (2.7) are substituted into equation (2.6) that can be so splitted in two governing equations: one for the mean conservative variables (the steady solution of the flow), and one for the perturbation variables (the perturbation solution of the flow). The solutions of the two governing equations are then combined together to obtain the instantaneous solution.

The linearized methods are not able to include non-linear effects into aero-elastic analysis (if not in the steady solution); for this reason, more recently with the increase of the computational power, non-linear methods have been developed. These methods can be semi-uncoupled or fully-coupled. For the non-linear semi-uncoupled methods [35-40] the blade vibration, pre-computed from a modal analysis, is only an input for the aero-elastic calculations. However, they can also include non-linear phenomena such as shock waves, boundary layer separations or shock/boundary layer interactions. Since the approach is semi-uncoupled, all the blades in the row should have the same dynamic behavior, i.e. each blade is subject at the same amplitude of vibration but with a constant phase delay respect its adjacent (only one IBPA). However, multiple frequencies are possible to take into account all time-dependent phenomena that should arise at different frequencies due to non-linear interactions. As the linearized methods, the blade vibration is also used to define a perturbation of the CFD mesh through the equations (2.5). However, the mesh perturbation actually deforms the grid at each time step, rather than to derive the linearized governing equation, i.e. the non-linear unsteady flow equations (URANS) are integrated on the deforming mesh.

The non-linear phenomena can be also included in the full-coupled methods [41-42]. The full-coupled (or two-way coupled) methods consider the influence of vibrations on the flow and vice-versa and they are not linked to a fixed frequency

or IBPA. The two fields are characterized by the RANS equations (URANS if non-linearity are considered) for the aerodynamic and by the structural modal dynamic equations for the structure. These two fields can be integrated with different level of coupling:

- Loose coupling: take advantage of well-established solution algorithms both for aero and structure dynamics through a minimization of unnecessary interaction;
- Tight coupling: the equation of the two field are solved together with a monolithic scheme;

In the loose coupling the interconnection between the two fields is done in the least extent practicable, i.e. the coupling only occurs in determinate points where the solution produces a relevant change. This scheme is usually used to limit the risk that a change made in a point produces unanticipated changes in other parts; however in the aero-elastic calculation the effects of the fluid-structure interaction could be lost. The second scheme is not a common practice because space and time discretization techniques strongly differ between the two domains. Besides, the time step for CFD computations is, generally, different orders of magnitude smaller than the time step of CSD solvers. Between these two extremes exist intermediate techniques that allow the aero-elastic calculations through an exchange of aerodynamic and structural information during the integration. Because the two solvers have different space and time discretization, the instantaneous solutions of the two fields should be synchronized at each step-time of integration. Different algorithms have been proposed; two of them are (Figure 2.8):

- Conventional serial staggered: it is illustrated on the left of Figure 2.8 and presents a time step equal for fluid and structure. At each time step the CFD solver computes the next pressure values which are given as inputs to the structural solver that provides a solution for displacements and dynamic variables with an accuracy of first order. However, large time steps can cause significant energy errors.
- Improved serial staggered: it is illustrated on the right of Figure 2.8 and presents a time shift of $\Delta t/2$ between the structural displacements and the fluid state vector. The sequence of solution is the same of the preview scheme, but the time shift reduces the possibility of errors.

In general, these coupled methods are computationally heavy and require long calculation times to obtain the solution.

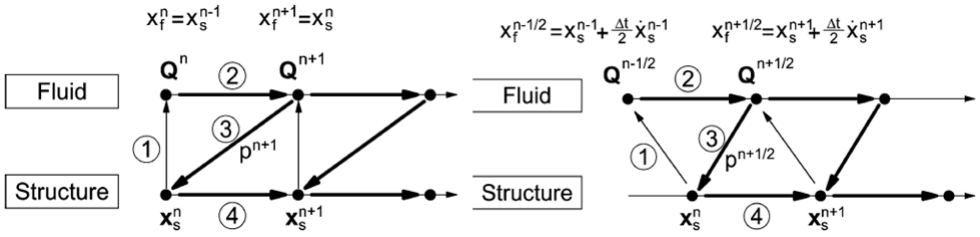


Figure 2.8: Conventional (left) and improved (right) time-staggered algorithm (ref. [41])

The methods presented before give information about the aerodynamic behavior of the blades in terms of state variables, but they do not give information about the aero-elastic effects (this counts for the semi-uncoupled methods and not for the coupled because the structure is solve together with the aerodynamic). To quantify the level of aero-elastic stability it is necessary to apply an energy method, i.e. the unsteady pressure of the blade is integrated over the entire blade for one cycle of oscillation to determine the aerodynamic work.

The aero-elastic stability is evaluated by checking the sign of the aerodynamic work:

- Positive: energy is transferred from fluid to blade, i.e. self-excited oscillation is presented (unstable condition);
- Negative: energy is transferred from blade to fluid, i.e. the oscillation is damped (stable condition).

Finally, the work of the fluid for one cycle of oscillation is compared with the mean kinetic energy of vibration to obtain the aero-damping (Figure 2.9a) and aero-stiffness coefficients (Figure 2.9b). The aero-damping is a coefficient that indicates the aero-elastic stability of the blade, while the aero-stiffness is a coefficient that indicates the variation of blade stiffness due to the presence of the flow.

The modal aero-damping coefficient of a blade array is usually characterized by negative/positive values for travelling mode shapes characterized by ND. As an example, in Figure 2.9a the negative values of aero-damping are associated to forward travelling wave (ND positive), while the positive values are associated to

backward travelling wave (ND negative). The meaning of the sign of the aero-damping coefficient is opposite to that of the aerodynamic work, i.e. a negative value means that the system is unstable (self-excited oscillations are presented), while a positive value means that the system is naturally stable (the oscillations are damped by the flow).

The aero-stiffness coefficient, instead, is always characterized by positive values both for positive and negative ND

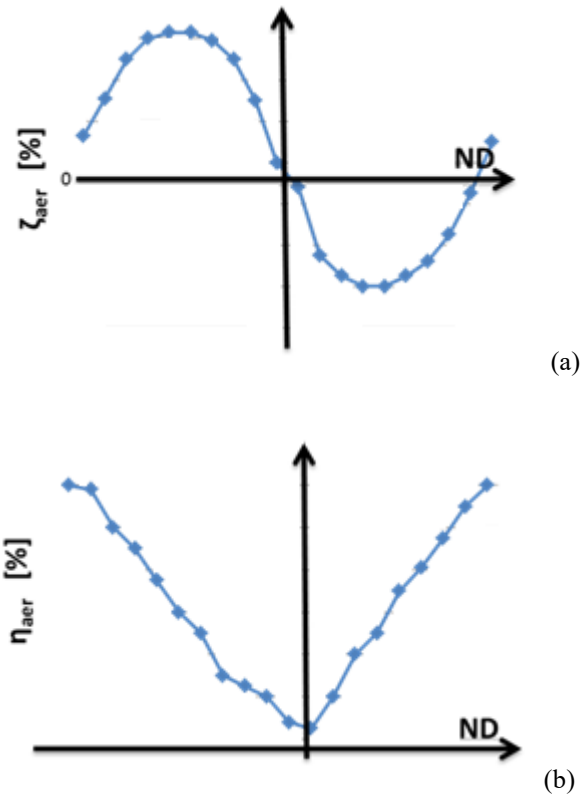


Figure 2.9: Typical trend of aero-damping (a) and aero-stiffness (b) coefficients at the variation of nodal diameters

The calculation of the aero-damping and aero-stiffness coefficients have been made in this thesis using a linearized method developed by the Department of Industrial Engineering of University of Florence [30] that is used by GE Avio Aero to design the blades.

#### *2.1.2.2 Suppression aero-elastic phenomena*

The effort to predict the occurrence of flutter phenomenon is only a part of the problem. Since the aerodynamic forces introduce energy in the structure, the stresses grow to each vibration cycle increasing the fatigue and reducing reliability of the structures. For this reason great attention should be placed on understanding how to avoid the insurgence of the flutter or to limit the flutter vibrations if this phenomenon acts on the blade. In the first case the better instrument is the mistuning, while in the second case the introduction of non-linear elements in the equation of motion due to the presence of friction contact surfaces in determinate region of the blades is the better choice.

##### 2.1.2.1.1 Mistuning

The rotating components of turbo-machinery are structures having nominally cyclic symmetry properties, i.e. every stage can be divided in a finite equal number of sectors. Usually these sectors are considered perfectly identical and with the same dynamic behavior; in this case the structure is said *tuned*. However, this hypothesis is not completely correct. In fact, in the reality, bladed disks completely tuned do not exist because imperfections of manufactory or tolerances produce some small difference among the components (Figure 2.10) and consequently also the dynamic behavior will not be the same. For these cases the term *mistuning* is used. Due to these irregularities, the rotor loses its symmetry and cannot be studied anymore through cyclic symmetry techniques. Although these imperfections are minimal, they can cause significant changes in the rotor behavior, producing bigger responses than those calculated in tuned conditions.

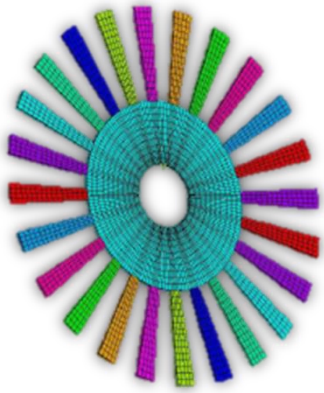

Figure 2.10: mistuned bladed disk

The first studies were launched by Whitehead and Ewins [43-44] in 1960s to understand the mistuning phenomenon and the effects of mistuning on the forced response and on the aero-elastic phenomena. The study of mistuning is mainly divided in two different approaches: the deterministic approach [45-46] and the statistical approach [47-48]. The deterministic approach searches to identify the level of mistuning inside a bladed disk to understand the effect of this phenomenon on the response of the blades. The studied mistuning can be natural (due to small differences between the blades with respect to the nominal geometry, material properties and contact interfaces of joints) or purposely induced (alternating mistuning where a blade cascade is made of determined pattern). The statistical approach searches the better model to represent the effects of the variation of geometry, mass or stiffness on the dynamic behavior of the blades. Usually these models are more complex and depend on the chosen type of patterns and on the imposed boundary conditions.

As said, thanks to the capability of mistuning to alter the dynamic response of the blades, many authors have studied this effect on the forced [43-46] and aero-elastic [49-52] responses. The authors have placed mainly their attention on the effect of induced mistuning because this can be controlled and chosen to maximize the reduction of amplitude of vibration [84]; besides, the induced mistuning is also able to mitigate the effect of natural mistuning.

The effect of mistuning in the aero-elasticity analysis is very important because it has a stabilizing effect on flutter stability. This happens because mistuning

(natural or induced) produces a non-constant IBPA among the blades that can be intended as a significant perturbation of the blade array response in terms of amplitude uniformity and phase shift between a blade and its neighbors. This is traduced in a change of the gas flow effect on the blade and, as a consequence, on the sign of the aerodynamic work.

#### 2.1.2.1.2 Friction contacts

The approaches to model and avoid the flutter described in the previous sections consider a linear dynamic of the bladed disk and the fluid-structure interaction is directly linked to the natural frequencies and normal mode shapes of the system. However, structural designers of aircraft engines have introduced nonlinearities in the bladed disk structure in terms of damping systems to reduce peak stress values during the vibratory phenomena caused by the external excitation forces. These damping systems are usually friction dampers or joints that use the friction forces to dissipate energy increasing the fatigue life of the blade. The major sources of friction damping in the bladed disk turbine are attributable to the blade-disk interfaces (blade root joint) [53, 54], the contact between adjacent blades connected by interference at the tip (shrouds) or mid-span airfoil (snubber) [55] and the presence of underplatform dampers [56, 57].

These friction contacts could be used to suppress the unstable flutter vibrations as it is usually made for the vibrations caused by excitation forces (forced response). The main friction dampers employed to limit the self-excited vibrations are the blade-disk interfaces or the underplatform dampers. These dampers are chosen because the blades in the tip-free condition (there is not interaction at tip between the blades) are more sensible at the flutter onset, while the blades with the shroud are often stable at flutter. The friction forces developing on damper surfaces produce dissipative energy that limits the self-excited vibrations and the Limit Cycle Oscillations is formed. In this condition, the amplitude and the frequency of the LCO is determined by the equilibrium between the energy introduced in the system by the flow and the energy dissipated by the friction contacts. However other two conditions may occur; in the first the aerodynamic energy is always bigger than the dissipative energy and as a consequence the system is always unstable. On the contrary, if the aerodynamic energy is always lower than the dissipative energy the system will be always stable. These equilibrium problems are qualitatively illustrated in Figure 2.11 where the aerodynamic energy is plotted with the blue dashed curve, while the dissipative energy is plotted with the red solid curve, both for one cycle of oscillation.

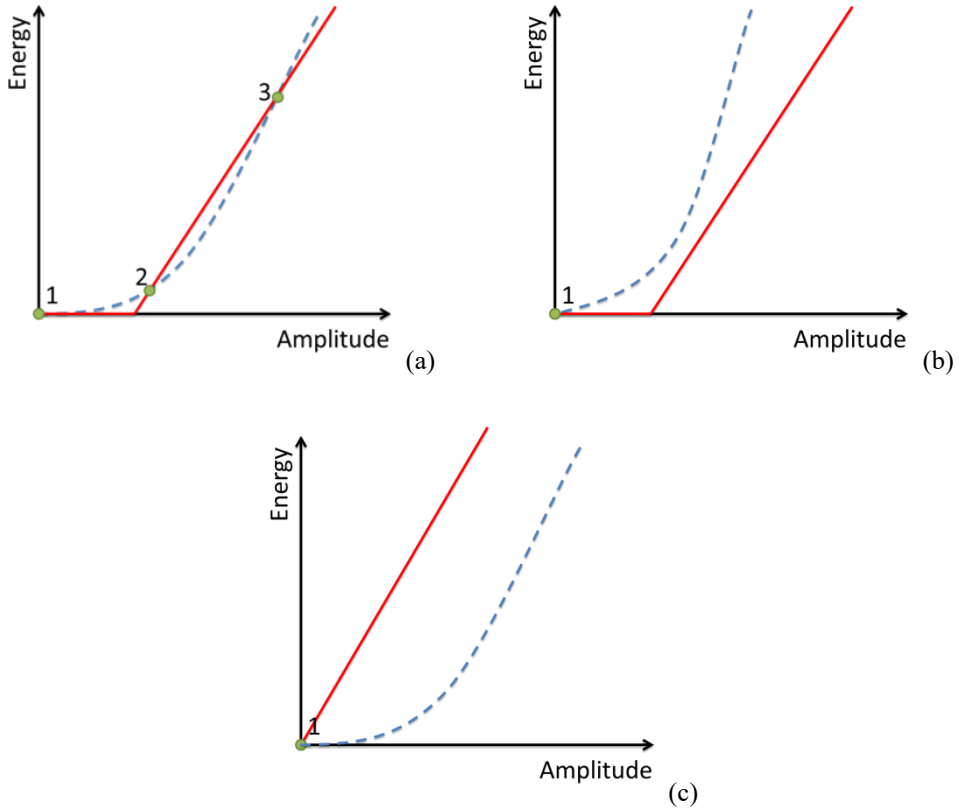


Figure 2.11: Possible energy balance between the energy introduced by aerodynamics (blue dashed curve) and dissipative energy by friction (red solid curve) – (a) LCO condition; (b) always unstable condition; (c) always stable condition

Only few authors have studied the LCO of the bladed disk structure in the presence of non-linearities as the friction contacts. Due to the complexity of the problem for the non-linear effects of the friction contacts, these studies have been usually realized considering a linearized aerodynamic and one-way coupled methods.

The first studies were conducted by Griffin. and Sinha in [58, 59]. In their works the authors have used a lumped parameters model based on one degree of freedom with a friction contact and a negative viscous damping that simulates the aerodynamic coupling (Figure 2.12). As many following studies, the contribution of the external synchronous force is assumed negligible and for this reason it is not considered in the equation of motion. This hypothesis has an effect on the dynamic study of the system; in fact the problem is not well-conditioned because the frequency of vibration becomes an unknown of the problem. Two different

approaches can be applied; in the first an additional equation is introduced (this equation is the energy balance) and this is the case used by Griffin and Sinha, while in the second case a mathematical operation is applied to reduce the number of unknown and this is the case used by Petrov in [60].

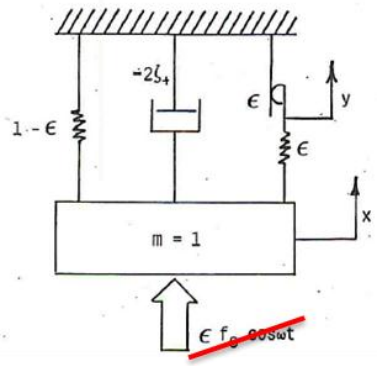


Figure 2.12: Lumped-parameter model used by Griffin J. and Sinha A. in [58]

The contribution of Griffin and Sinha was more important to understand the flutter response in terms of stable and unstable solutions and their variation if the aero-damping coefficient changes. In 2000s, very important are the studies of Corral, Gallardo and Martel. They have studied the LCO through the use of a lumped parameter model for the whole bladed disk sector with a blade root joint determining the amplitude of the blade from the equality of the energy dissipated at the blade root and the energy supplied from gas flow [61, 62]. Another important work is [63], where the authors have studied the combined effect of forced response and flutter phenomena identifying the fields where they act independently or together. Corral also proposed in [64, 65] a fully coupled method based on the direct time integration (DTI) of motion and RANS equations that solve a lumped parameter model of a bladed disk, while the non-linear equations characterizing the friction forces are solved using a Newton-Raphson method.

In the same years, Petrov in [60] has developed a general method, based on the mathematical properties of the Harmonic Balance Method (HBM) complex numbers, and the mathematical homogeneity of the linearized equation of motion in the presence of friction contacts and flutter-induced external forces that can be applied to model generated with FEM. In particular, from the HBM, it is possible to write the displacements *x(t)* as:

$$x(t) = X_0 + \sum_{h=1}^{H}(X_h^{(c)}\cos(h\omega t) + X_h^{(s)}\sin(h\omega t)) \quad (2.8)$$

where $X_h^{(c)}$ and $X_h^{(s)}$ are the harmonic coefficients, and $h$ is the specific number of harmonics. If $x(t)$ is a periodic solution of equation of motion, then also $x(t+t_0)$ is a solution of the same equation that can be written as:

$$x(t + t_0) = X_0 + \sum_{h=1}^{H}\left(X_h^{(c)}\cos\left(m_h\omega(t + t_0)\right) + X_h^{(s)}\sin\left(m_h\omega(t + t_0)\right)\right) \quad (2.9)$$

where the phase of the vibrations can be selected arbitrarily by adding any time shift (t0) to the time variable. Since t0 can be selected arbitrarily, it is possible to set an arbitrary value α for any selected harmonic coefficient that allows to reduce the number of unknown by one in order to have a well-conditioned problem.

More recently, Krack et al. in [66] used a lumped parameter dynamic system to calculate the LCO of a cyclic symmetric structure when multiple modes with different values of Nodal Diameters (ND) are considered. Great attention is paid for the calculation of the contact forces when more unstable mode shapes exist since the ND associated to the natural frequencies are not commensurable. For this reason, simple HBM method cannot be used to solve the equilibrium equations in the frequency domain. In fact, bi-dimensional FFT is used in [66] to consider the presence of two unstable mode shapes having two different nodal diameters. The consequence is an extension of the calculation time that may become prohibitive if such method is applied to a model of a real bladed disk with real distributed contacts and with 4, 5 or even more unstable mode shapes with different ND values. Krack also presented in [67] a recent review about the aero-elastic calculation (both forced response and flutter analysis) of bladed disk including the effects of friction contacts.

## 2.2 Conclusion

The flutter is an important aero-elastic phenomenon that produces, if not considered, a reduction of life and reliability of the blades. For this reason, the engineers have produced many efforts to predict, to avoid or to limit the occurrence of this problem developing different methods. These methods are based on the fluid-structure interaction between the blade rows and the hot gases that pass through the turbine. Two main type of coupling have been considered in these methods, the one-way coupled and the two-way coupled methods, with the

preference of the first due to the difficulty of modeling the flutter phenomenon when non-linearity are included. The one-way coupled methods are divided in the aero-dynamic methods that allow to model the phenomenon and identify the level of the flutter instability, and the structural methods that allow to limit and determinate the flutter amplitudes when these are presented. The first methods are well known and established in the design process, while the seconds have been studied by few author and do not yet used for the design. The potentiality of the structural methods in the design process are big. In fact, a blade, unstable at flutter, could be considered acceptable if the damping systems are able to limit or avoid the instability and as a consequence new design architectures that increase the performance and reduce the weight may be possible. It is in this fields, that this thesis will focus its attention.

# Chapter 3

# Reduction techniques, contact model and solution strategy

In this chapter, the more important and used instruments for the future analyses are briefly presented. In particular the attention will be placed on the reduced order model (ROM) that allows to reduce the degrees of freedom to analyze and in this way saving computation time, and on the contact model that allows to calculate the friction forces acting on the contact surfaces of the blade and introduces the non-linear effects in the equation of motion. At last, a general solution strategy for the non-linear equations is also presented.

The reduced order model and the contact model have an effect on the non-linear equation of motion that is here reported:

$$[M]\ddot{x} + [C]\dot{x} + [K]x = F_e + F_{nl} \tag{3.1}$$

where $[M]$, $[C]$ and $[K]$ are the mass, damping and stiffness matrices, $F_e$ is the vector of excitation forces and $F_{nl}$ is the vector of non-linear friction forces.

## 3.1 Reduced order model (ROM)

The solution of non-linear equation of motions (3.1) is realized through iterative numerical methods that generally lead to considerable computing times, especially if it is run on a normal pc. The bladed disk, object of the future analyses, has been

modeled on finite elements using a large number of nodes that the solution of equation of motions are generally not obtainable in acceptable times, even if non-linear computation is only performed for contact nodes. Therefore, it is necessary to reduce the degrees of freedom of the model without losing fundamental information for a truthful analysis of the system.

The ROM techniques used in this thesis are mainly four:

- The Craig-Bampton - Component Mode Synthesis (CB-CMS);
- Cyclic symmetry (CS);
- Tran reduction technique;
- Modal reduction.

Of these techniques, the cyclic symmetry is typical of the cyclic structures as the bladed disk, while the other three reduction techniques are more general and they can be applied in many cases.

In general the ROM techniques allow to white a rectangular reduction matrix [*T*] that reduced the size of the vectors of dofs/forces and the size of the matrices (see Fig. 3.1).

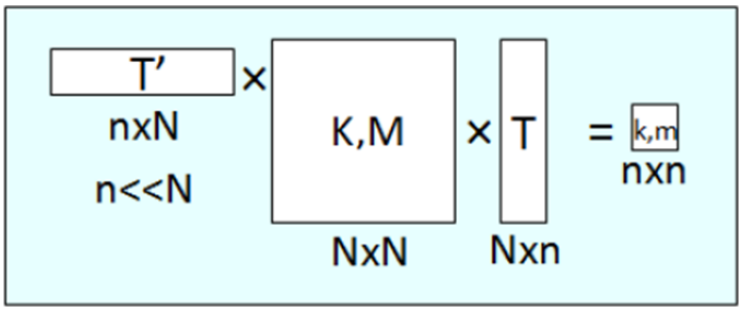


Figure 3.1: graphical representation of application of a generic reduction matrix [*T*] to reduce the size of the stiffness and mass matrices

The general equations, that allow the ROM, are the following:

$$
\begin{aligned}
&X = [T]x \\
&[m] = [T]^H[M][T] \\
&[c] = [T]^H[C][T] \\
&[k] = [T]^H[K][T] \\
&f_e = [T]^H F_e \\
&f_{nl} = [T]^H F_{nl}
\end{aligned}
\tag{3.2}
$$

where the capitol letters (X, M, C, K and F) represent the vectors or the matrices of the full system, while small letters represent the vectors or the matrices of the reduced system.

### 3.1.1 Craig-Bampton - Component Mode Synthesis (CB-CMS)

The CB-CMS reduction technique [68] is a common technique implemented in most FE softwares (Ansys, Nastran) and it is based on the definition of a set of master $x_m$ and slave $x_s$ degrees of freedom (dofs) of the physical model plus an additional set of slave modal dofs $\eta_s$. The first set is the set that remains explicit in the ROM while the remaining part of dofs is omitted as a function of the first set according to the Guyan static reduction technique formulation [69] where the static deflection shapes of the slave dofs are written by imposing a unitary displacement of each master dofs one by one. With this process the slave nodes are forced to move according to the deformation of the master nodes. Since the Guyan reduction technique is not sufficiently representative of the dynamics of the system, a number of slave modal shapes is added to the static deflection base obtained from a modal analysis where all the master dofs are constrained simultaneously.

The bladed disk is reduced according to the following transformation for each component (blade and disk):

$$
x = \begin{Bmatrix} x_m \\ x_s \end{Bmatrix} = \begin{bmatrix} I & 0 \\ G & \Phi_s \end{bmatrix} = \begin{Bmatrix} x_m \\ \eta_s \end{Bmatrix} = [T_{CMS}]x_{CMS} \tag{3.3}
$$

where $I$ is the identity matrix, $G$ is the Guyan matrix, $\Phi_s$ is a subset of the slave modal matrix, $\eta_s$ is the vector of the modal slave coordinates and $[T_{CMS}]$ is CB-CMS reduction matrix. $x_{CMS}$ is the vector of dofs remained after the reduction which number is much lower than the total number of dofs $x$. CB-CMS reduction matrix is applied to the equation of motion (3.1) to reduce the size of the system in according to the equations (3.2).

### 3.1.2 Cyclic symmetry (CS)

The bladed disk is a cyclic symmetric component that is excited by a periodic self-excited force, therefore each sector vibrates as the adjacent sectors but with a phase lag given by the IBPA (eq. (2.5)).

The bladed disk can be reduced to a single sector by applying cyclic symmetry constraints [68] to its left and right interfaces (see Figure 3.2). For example, it is possible to write the right interface dofs depending on the left interface dofs (or vice-versa) in according with the travelling force that can be clockwise or counterclockwise with respect to a defined cylindrical reference system:

$$x_l = x_r e^{iIBPA} \tag{3.4}$$

where $x_l$ are the dofs of the left interface while $x_r$ are the dofs of the right interface of the disk. Equation (3.4) performs a reduction of the dofs of the system, in fact

$$x = \begin{Bmatrix} x_l \\ x_r \\ x_o \end{Bmatrix} = \begin{bmatrix} e^{iIBPA} & 0 \\ I & 0 \\ 0 & I \end{bmatrix} \begin{Bmatrix} x_r \\ x_o \end{Bmatrix} = [T_{CS}] x_{CS} \tag{3.5}$$

where $x_o$ are the inner dofs not included in the interfaces, $[T_{CS}]$ is the cyclic symmetry reduction matrix and $x_{CS}$ is the vector of the reduced dofs after applying the cyclic symmetric constraint.

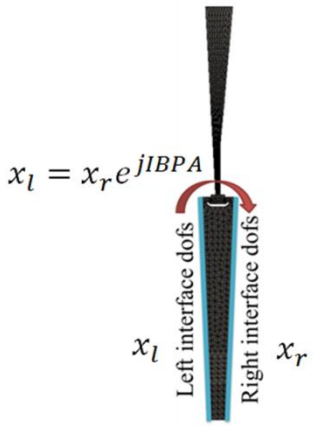


Figure 3.2: application of cyclic symmetric constraints at the interface on a single bladed disk sector

### 3.1.3 Tran reduction technique

The Tran reduction technique is a technique developed by Tran in [70]. This technique is used to further reduce the master dofs remained after the CB-CMS reduction if these are yet too big. In particular, this technique proposes a methodology to reduce the interface dofs replacing them with a linear combination of modal shapes.

The starting point to perform a Tran reduction is to apply the Guyan reduction at full component, where the considered master dofs are only the interface dofs. From the static reduced mass and stiffness matrices, a modal analysis is performed and only a small number of modes is taken into account (the modes obtained from the modal analysis of the reduced matrices represent the mode shapes of the interface dofs). In this way the modal coordinates of the considered mode shapes substitute the interface dofs.

The array of the explicit dofs of the master nodes becomes:

$$x = \begin{Bmatrix} x_l \\ x_r \\ x_o \\ \eta_s \end{Bmatrix} = \begin{bmatrix} \Phi_l & 0 & 0 \\ \Phi_r & 0 & 0 \\ 0 & I & 0 \\ 0 & 0 & I \end{bmatrix} \begin{Bmatrix} \eta_i \\ x_o \\ \eta_s \end{Bmatrix} = [T_{Tran}] x_{Tran} \tag{3.6}$$

where $I$ is the identity matrix, $\Phi_l$ and $\Phi_r$ are a subset of the interface modal matrix, $\eta_i$ is the vector of the interface modal coordinates, $[T_{Tran}]$ is the Tran reduction matrix and $x_{Tran}$ is the vector of the reduced dofs after applying the Tran reduction technique.

The Tran reduction technique can be applied after the cyclic symmetry reduction on the CMS dofs; in this case the equation (3.6) becomes:

$$x_{CS} = \begin{Bmatrix} x_r \\ x_o \\ \eta_s \end{Bmatrix} = \begin{bmatrix} \Phi_{r,CS} & 0 & 0 \\ 0 & I & 0 \\ 0 & 0 & I \end{bmatrix} \begin{Bmatrix} \eta_{i,CS} \\ x_o \\ \eta_s \end{Bmatrix} = [T_{Tran}] x_{Tran} \tag{3.7}$$

where $\Phi_{r,CS}$ and $\eta_{i,CS}$ are respectively a subset of the interface modal matrix reduced in cyclic symmetry and the vector of the interface modal coordinates.

If all three reduction techniques are applied, the whole transformation is:

$$x = [T_{CMS}][T_{CS}][T_{Tran}] \begin{Bmatrix} \eta_{i,CS} \\ x_o \\ \eta_s \end{Bmatrix} = [T_{TOT}] \begin{Bmatrix} \eta_{i,CS} \\ x_o \\ \eta_s \end{Bmatrix} \tag{3.8}$$

### 3.1.4 Modal reduction

The non-linear differential equation of motion (3.1) is written in the physical domain and can be rewritten in the modal domain because the physical displacements can be approximated with a linear combination of a limited number of normal modes:

$$x \simeq [\Psi]\, q \tag{3.9}$$

where $[\Psi]$ is the modal matrix obtained from a modal analysis that includes a set number of modes and $q$ is the vector of the modal coordinates. For the modal reduction, the modal matrix $[\Psi]$ is precisely the rectangular reduction matrix $[T]$, i.e.

$$[T] = [\Psi] \tag{3.10}$$

that can be used to derive the equations (3.2).

The set of the equations of motion can be turned into a set of uncoupled equations in the modal form by:

$$[m_{mod}]\ddot{q} + [c_{mod}]\dot{q} + [k_{mod}]q = f_{e,mod} + f_{nl,mod} \tag{3.11}$$

where the modal mass is the unity matrix and the damping and stiffness matrices are all diagonal.

$$[\mathrm{m}_{mod}] = [I]$$

$$[\mathrm{c}_{mod}] = \begin{bmatrix} 2\zeta_1\omega_1 & 0 & 0 \\ 0 & \ddots & 0 \\ 0 & 0 & 2\zeta_n\omega_n \end{bmatrix} \tag{3.12}$$

$$[k_{mod}] = \begin{bmatrix} \omega_1^2 & 0 & 0 \\ 0 & \ddots & 0 \\ 0 & 0 & \omega_n^2 \end{bmatrix}$$

In the equation (3.12) $\omega$ and $\zeta$ are respectively the natural frequency and modal damping of the system.

## 3.2 Contact model

In the equation of motion (3.1) the term $F_{nl}$ is a non-linear term that represents the friction forces produced on the contact surfaces of joints. The contact model is based on the Coulomb friction law where the maximum value of the generic friction force $f_t(t)$ occurs in case of slipping and is equal to the normal load $n(t)$ on the contact multiplied by the friction coefficient $\mu$:

$$f_t(t) = \mu n(t) \tag{3.13}$$

In this thesis, the Coulomb friction law is implemented in a contact model [71] with a normal $k_n$ and a tangential $k_t$ stiffnesses (Figure 3.3). $k_n$ allows for a variable normal load once a normal preload $n_0$ is defined:

$$n(t) = n_0 + k_n v(t) \tag{3.14}$$

where *v(t)* is the relative normal displacement on the contact. As a consequence the separation occurs when *v(t)* is lower than a limit value:

$$\text{if} \quad v(t) < -\frac{n_0}{k_n} \quad \rightarrow \quad n(t) = 0 \, . \tag{3.15}$$

$k_t$ takes into account a stick state of the contact allowing the two parts moving on each other without slipping:

$$f_t(t) = f_0 + k_t(u(t) - u_0) \tag{3.16}$$

where *u(t)* is the relative displacement between the two parts, $u_0$ and $f_0$ are respectively the relative tangential displacement and tangential contact force when the transition between the slip state (or separation state) and the stick state occurs. The value of the contact parameters, friction coefficient and tangential contact stiffness, are generally experimentally determinate by hysteresis loop measurement with test rig purposely developed [72, 73, 85] or numerically computed, for the contact stiffnesses, by means of specific contact models [74-76]

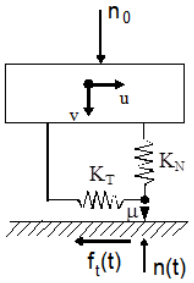


Figure 3.3: Contact model

The hysteresis loop can assume different shapes according to the relative phase lag of the relative tangential displacement with respect to the normal displacement (see reference [83]). In Figure 3.4 three types of hysteresis loops are shown assuming single harmonic oscillation for *u(t)* and *v(t)*: the first when *u(t)* and *v(t)* are in-phase, the second when lift off occurs within one cycle, the third when *u(t)* and *v(t)* do not vibrate in-phase. These hysteresis loop have been obtained using the model in Fig 3.3 and a solution method based on the prediction-correction method. This method is described in [80] and it is based on the prediction that the eq. (3.16) is initially always valid. The prediction of the stick system is valid until

the force (3.16) is smaller than the Coulomb limit; in the opposite, the friction force is corrected to the value of the Coulomb limit. In the following analyses the prediction-correction method will be used to calculate the non-linear forces.

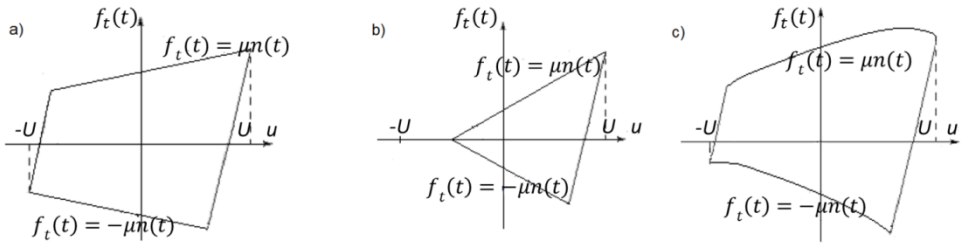


Figure 3.4: example of hysteresis loops at the contact

Depending on the application and the local kinematics of the contact, the contact area can be discretized in a layer of contact elements in order to simulate local phenomena of sticking, slipping or separation. A two dimensional motion on the contact surface can be modeled by placing two orthogonal contact elements sharing the same preload $n_0$ and normal contact stiffness $k_n$. The orbital tangential motion of the two parts in contact is decoupled into two independent oscillations on the orthogonal planes defined by the two contact elements (Figure 3.3).

## 3.3 General solution strategy for the non-linear equations

In order to reduce the calculation time of a non-linear numerical time integration, the Harmonic Balance Method (HBM) is used [77] to solve the equations of motion (3.1) [77-79]. This is possible if the external excitation is single-harmonic because in this way the external force produces the periodicity of the displacements $x$ and the nonlinear forces $F_{nl}$. The property of periodicity permits to express the time varying displacements ($x$) and forces ($F_e$ and $F_{nl}$) in a truncated Fourier series of $H$ orders, where $H$ is the maximum number of harmonics that are considered. Consequently, displacements and forces become:

$$x = x^{(0)} + \Re\left(\sum_{h=1}^{H} \bar{x}^{(h)} e^{ih\omega t}\right)$$

$$F_e = F_e^{(0)} + \Re\left(\sum_{h=1}^{H} F_e^{(h)} e^{ih\omega t}\right) \tag{3.17}$$

$$F_{nl} = F_{nl}^{(0)} + \Re\left(\sum_{h=1}^{H} \bar{F}_{nl}^{(h)} e^{ih\omega t}\right)$$

where ω is the excitation frequency, the *0* order represents the static components and the Fourier coefficients $\bar{x}^{(h)}$ e $\bar{F}_{nl}^{(h)}$ are complex quantities.

The Equations (3.19) are replaced into the equations of motion (3.1) obtaining a set of algebraic complex equations:

$$\left[D^{(h)}\right]x^{(h)} = F_e^{(h)} + F_{nl}^{(h)}, \quad h = 1,2,\dots H \tag{3.18}$$

where $\left[\mathrm{D}^{(\mathrm{h})}\right]$ is the $\mathrm{h}^{\mathrm{th}}$ dynamic stiffness matrix of the system that has the following form:

$$\left[D^{(h)}\right] = -(h\omega)^2[M] + ih\omega[C] + [K] \tag{3.19}$$

The equation (3.18) is non-linear because contact forces $F_{nl}^{(h)}$ depend on the displacements of the contact dofs that are a part of the total dofs $x^{(h)}$. Since the equations of motion are formulated in the frequency domain while the contact model operates in the time domain, an Alternating Frequency Time (AFT) [80, 81] also known as Hybrid Frequency Time (HFT) method [82] must be used in order to pass from the frequency domain to the time domain to calculate the hysteresis loop and then again to go back to the frequency domain by the Fourier series (Figure 3.5). In detail, the calculation procedure follows the following steps:

1. Periodical relative displacements *u(t)* and *v(t)* are computed from Fourier coefficients $u^{(h)}$ and $v^{(h)}$ by Inverse Fast Fourier Transform (IFFT);
2. Contact forces *n(t)* and $f_t(t)$ are computed by means of equations (3.14) and (3.16);
3. The Fourier coefficients $n^{(h)}$ and $f_t^{(h)}$ are computed from *n(t)* and $f_t(t)$ respectively by Fast Fourier Transform (FFT).

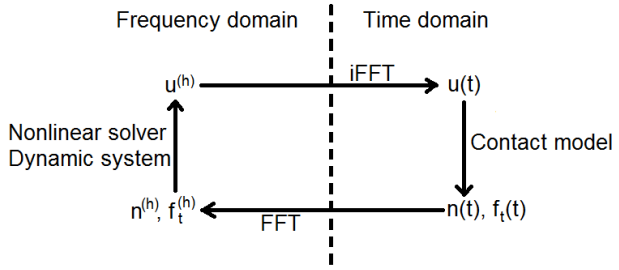


Figure 3.5: AFT/HFT method

With the Fourier coefficient of the contact forces it is possible to assemble the contact force vector $F_{nl}^{(h)}$. The equations of motion (3.18) are solved using finite differences to compute derivatives in the Newton-Raphson method.

# Chapter 4

# Flutter analysis for a lumped parameter model

In this chapter, the flutter analysis will be performed on simple systems such as the lumped parameter models to understand what are the properties of the flutter on the structures and what are the parameters that mostly influence the results. As first implementation, the method and the results obtained by Griffin. and Sinha in [58, 59] are first studied. These results, that are generically considering the base of the flutter analyses on the turbo-machinery, will be used to understand if the results obtained with a proposed method are correct in terms of typical trend. Three different structures will be analyzed with the method developed by the authors:

- One degree of freedom system;
- Lumped parameter model of a bladed disk;
- Lumped parameter model of a bladed disk reduced with cyclic symmetry hypothesis.

## 4.1 Griffin and Sinha results

Griffin and Sinha in [58, 59] were the first authors to study the suppression of the flutter phenomena in the turbo-machinery using friction contacts. In their two works the authors have simulated a blade with a damper sliding on the ground in

[58] and a row of blade with two dampers in [59], one sliding on the ground and the other acting between the blades; in both cases they used a lumped parameter dynamic system.

More attention will be placed on the results of [58] because in this work the authors placed the basis to understand the flutter phenomenon in the turbo-machinery in terms of stable and unstable solutions and their variation when the aero-damping coefficient changes. In [58] a lumped parameter model based on one degree of freedom with a friction contact and a negative viscous damping that simulates the aerodynamic coupling was used (Figure 4.1). The contribution of the external aerodynamic synchronous force was assumed, at the beginning, negligible and taken into account afterwards.

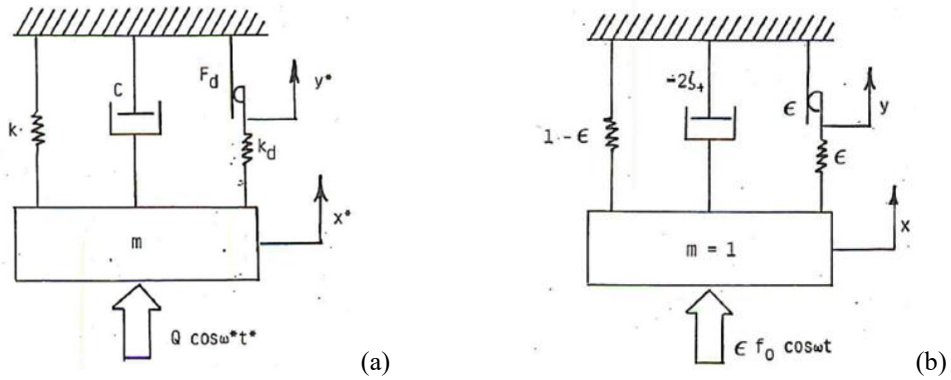


Figure 4.1: Lumped-parameter model used by Griffin and Sinha in [58] – (a) dimensional system, (b) dimensionless system

The equation of motion associated to the dimension system in Figure 4.1a is:

$$m\frac{d^2x^*}{dt^2} + c\frac{dx^*}{dt} + kx^* = k_d(x^* - y^*) + Q\cos(\omega^* t^*) \tag{4.1}$$

that can be turned into dimensionless notation using the following equation:

$$\varepsilon = \frac{k_d}{k_d + k}$$

$$x = \frac{x^*}{x_0} \; and \; y = \frac{y^*}{x_0} \tag{4.2}$$

$$x_0 = F_d/k_d$$

$$f_0 = \frac{Q}{F_d} = \frac{Q}{k_d x_0}$$

In the eq. (4.2) $F_d$ is the force required to cause the damper to slip and $x_0$ is the linear displacement when the system is stuck.

The resulting differential equation of motion is:

$$\frac{d^2x}{dt^2} - 2\zeta_+ \frac{dx}{dt} + x = \varepsilon y + \varepsilon f_0 \cos(\omega t) \tag{4.3}$$

where $x$ is the displacement of the mass, $y$ is the displacement of the damper, $\zeta_+$ is the viscous damping that simulates the interaction of the fluid on the structure, $\varepsilon$ is an equivalent stiffness of the contact, $f_0$ is the non-dimensional amplitude of the external force and $\omega$ is a non-dimensional angular frequency.

### 4.1.1 No external force ($f_0 = 0$)

When a synchronous excitation is not present, a small perturbation produces an uncontrolled increase of the amplitude of vibration due to the negative viscous damping until the contact produces dissipative energy that balances the energy introduced by the fluid in the structure and the system reaches the steady state. In the steady state the response can be considered harmonic and a Fourier transformation can be applied to the equation (4.3) passing from the time domain to the frequency domain. Under these assumptions, the non-linear term can be expanded in Fourier series obtaining:

$$\varepsilon y = a\cos(\omega t) + b\sin(\omega t) \tag{4.4}$$

where $a$ and $b$ are the coefficients of the Fourier series:

$$a = \varepsilon A[\pi - \vartheta_c + {}^1\!/_2 \sin(2\vartheta_c)]/\pi$$
$$b = 4\varepsilon(1 - {}^1\!/_A)/\pi \tag{4.5}$$

where $A$ is the amplitude of vibration and $\vartheta_c$ is the phase angle that occurs in the transition between the stick and slip condition.

$$\vartheta_c = \cos^{-1}(1 - {}^{2}/_{A}) \tag{4.6}$$

If the equation (4.4) is substituted into equation (4.3), the term $a$ adds a contribution to the stiffness while the term $b$ adds a contribution to the aero-damping. It is important to note that the pulsation $\omega$ of the system is not known a priori because a synchronous periodic external force is not considered (this is an important aspect that will often return in this thesis).

To solve this problem an additional equation is necessary. Since for the steady state response the balance of the forces acting on the system should be equal to zero, the balance of aerodynamic and frictional forces is:

$$2\zeta_+ = b/\omega A \tag{4.7}$$

The equations (4.3) and (4.7) can be manipulated to obtain the amplitude and the frequency of the flutter response:

$$A = \frac{4/\pi \pm [(4/\pi)^2 - (32\zeta_+\omega)/(\varepsilon\pi)]^{1/2}}{4(\zeta_+\omega/\varepsilon)} \tag{4.8}$$

$$\omega^2 = 1 - \varepsilon(\pi - \vartheta_c + {}^{1}/_{2}\sin(2\vartheta_c))/\pi \tag{4.9}$$

These two equations are solved together and iteratively for different values of $\varepsilon$ and $\zeta_+$ obtaining the results shown in Figure 4.2.

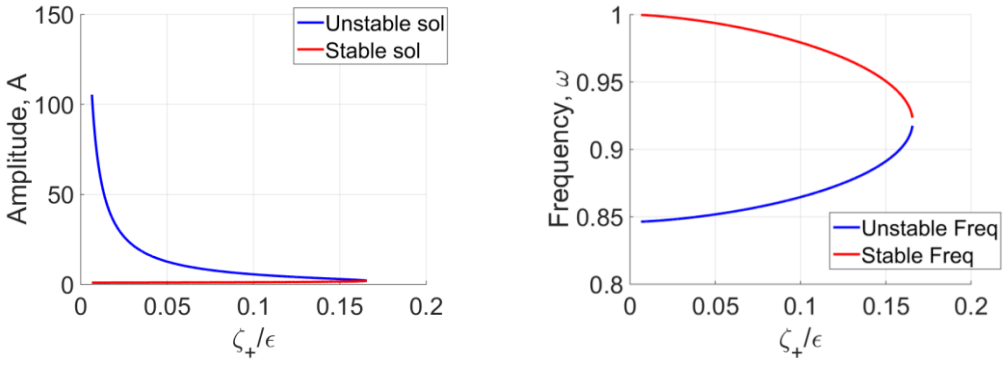


Figure 4.2: Flutter response by varying the ε and $\zeta_+$ in terms of amplitude (left) and frequency (right)

The results presented in Figure 4.2 are very important and show that for each ratio of $\zeta_+$ and $\varepsilon$ two solutions exist: one is stable and the other one is unstable. The stable solution will be called Limit Cycle Oscillation (LCO) and is characterized by small amplitude and high frequency, while the unstable solution will be called stability limit and is characterized by big amplitude and low frequency. The maximum value of amplitude can be controlled by the friction damper $\zeta_+$. The value of $\zeta_+$ corresponding to the maximum amplitude can be inferred from eq. (4.8) by setting the quantity under the radical equal to zero. The obtained equation is the following:

$$\zeta_+ = \frac{\varepsilon}{2\pi\omega} \tag{4.10}$$

When $\zeta_+$ assumes this value, the amplitude $A$ becomes a single value that represents an unstable solution. In fact, any perturbation from this point produces an ineffective damped and uncontrolled self-excited vibrations; while for value bigger than the maximum the system is always unstable because the damper is not able to limit the vibration. These considerations can be easily seen with a qualitative diagram of the energy balance illustrated in Figure 4.3a where three different ratios of $\zeta_+$ and $\varepsilon$ have been chosen. The ratio 1 produces two points of intersection between the dissipative energy (red line) and the aerodynamic energy (blue line); the ratio 2 presents only a point that represents the tangential point between the dissipative energy and the aerodynamic energy (blue dash line) and can be seen as the limit condition to control the flutter oscillations; finally, the ratio 3 does not show any intersection point, i.e. the system is always unstable.

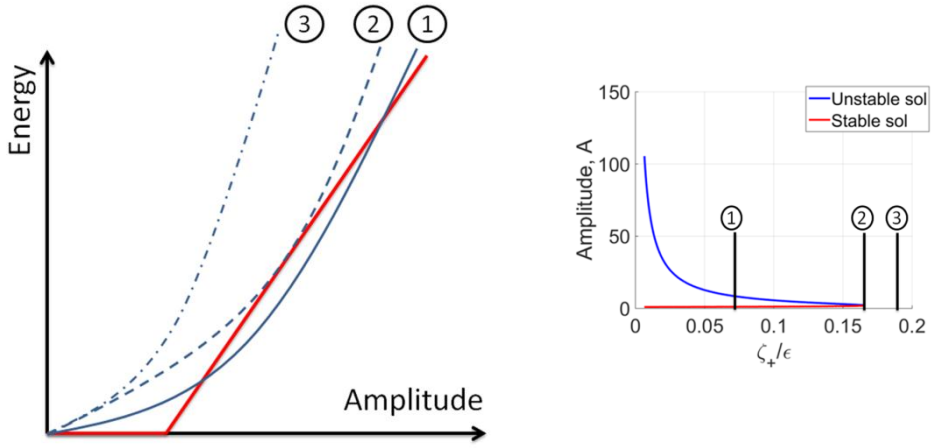


Figure 4.3: qualitative diagram of the energy balance for three different ratios of ε and $\zeta_+$

In Figure 4.2 the blue curve of the unstable solutions divides the plot in two regions: one stable and one unstable. These two regions have been called in this way because, fixed the ratio $\zeta_+$ on ε, an initial point under the blue line produces a controlled response at flutter (the attractor point is the stable solution), on the contrary, an initial point over the blue line produces uncontrolled self-excited vibrations. This result can be better seen through a solution of the equation (4.3) in the time domain. The points chosen are reported in Figure 4.4:

- A = 5 @ $\zeta_+/\varepsilon = 0.1$ in the stable region;
- A = 6 @ $\zeta_+/\varepsilon = 0.1$ in the unstable region;

while the time responses are shown in Figure 4.5. In detail, Figure 4.5a shows the stable response where the initial point is the point 1 of Figure 4.4; while Figure 4.5b shows the uncontrolled response from the point 2. The stable response was analyzed with a fast fourier transform (FFT) obtaining the same values of amplitude and frequency calculated in the frequency domain (Table 4.1).

| | Frequency domain | Time domain |
|---|---|---|
| Amplitude | 1.239 | 1.237 |
| Frequency | 0.9792 | 0.9790 |

Table 4.1: comparison of the results in frequency domain with that in time

domain

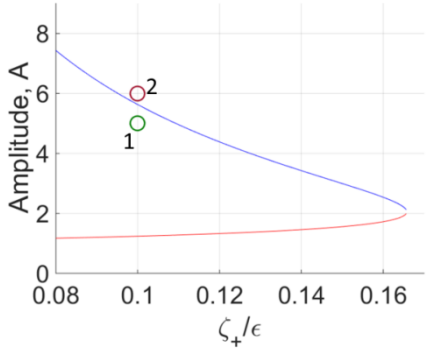


Figure 4.4: initial points for the direct time integration: 1 – stable point; 2 – unstable point

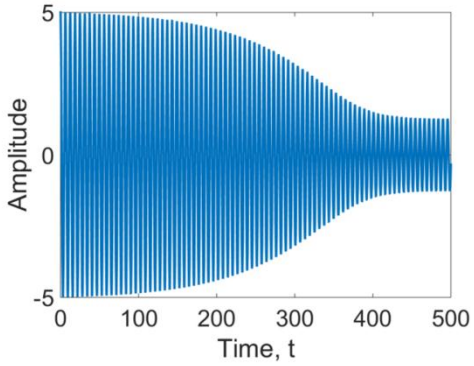


(a)

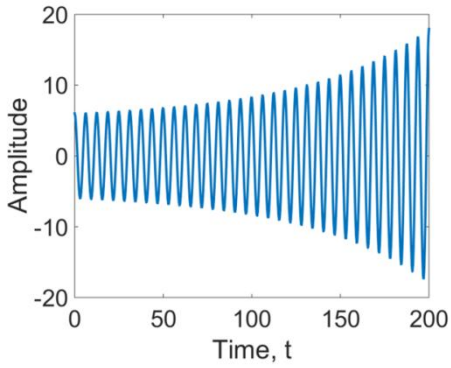


(b)

Figure 4.5: time response from point (1) of figure 4.4 – figure (a); from point (2) – figure (b)

### 4.1.2 External force ($f_0 \neq 0$)

In the second part of [58], Griffin and Sinha take into account the presence of a synchronous external force due to the pressure field caused by the presence of upstream static structures (stator vanes). In this case, the steady state is obtained when the dissipative energy balances the work of the aerodynamic and external forces. In this condition the response of the system is periodic, but not simply harmonic because two frequencies exist: one frequency for the flutter response and one frequency of the excitation force.

To avoid the presence of these two frequency values, the authors have considered an external excitation at the natural frequency because in this way the response becomes simply harmonic. Mathematically, the equation (4.8) becomes:

$$A = \frac{(4/\pi - f_0) \pm [(4/\pi - f_0)^2 - (32\zeta_+\omega)/(\varepsilon\pi)]^{1/2}}{4(\zeta_+\omega/\varepsilon)} \tag{4.11}$$

while the equation (4.9) does not change. As the previous case, the equations (4.11) and (4.9) are solved simultaneously and the results are reported in Figure 4.6.

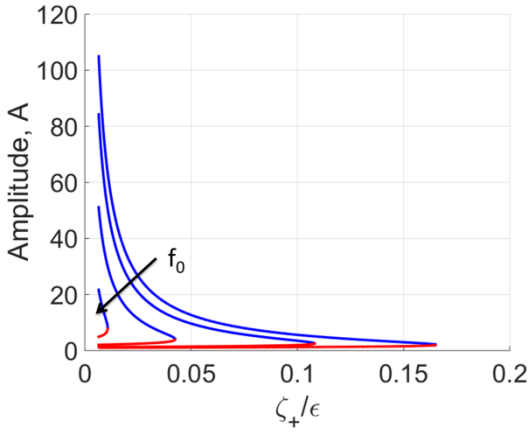


Figure 4.6: Flutter response at a variation of $f_0$

It is possible to see, that the increase of the external force produced a reduction of the stable region until a maximum value of $f_0$ that the authors have identified in:

$$f_0 \cong 4/\pi \tag{4.12}$$

When $f_0$ reaches its maximum value, the stable region disappears and the system is always unstable because the damper is not able anymore to dissipate the energy introduced by the fluid in the structure.

This section has been introduced to give a complete description of work [58] of Griffin and Sinha. In this thesis, the contribution of external forces will not be considered because the influence of the external force on flutter phenomenon can be usually neglected. This is possible because the flutter onset takes place away from the resonance conditions (see Fig. 2.1) where the influence of external forces is negligible.

## 4.2 One degree of freedom

The results presented in the previous section are based on the considerations and equations proposed by Griffin and Sinha in [58]. From this point, a proper formulation of the flutter analysis has been developed for a lumped parameter model with one degree of freedom (dof). The model used is shown in Figure 4.7 and it is similar to that used in [58], but for convenience of the author the names of the variables have changed.

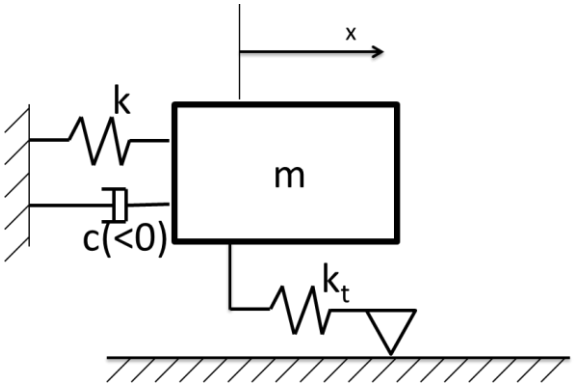


Figure 4.7: Lumped parameter model with one dof

In particular $m$, $c$ and $k$ are the mass, the damping and the stiffness of the system and $k_t$ is the tangential stiffness of the contact model. The damping $c$ is a viscous damping with negative sign to simulate a transfer of energy from the fluid to the structure.

The general equation of motion associated to this system is:

$$m\ddot{x} + c\dot{x} + kx = f_e + f_{nl}(x) \tag{4.13}$$

where $f_e$ is the external force and $f_{nl}(x)$ is the non-linear friction force that is a function of the displacement $x$.

On this system two hypotheses are made:

1. the external force is considered negligible, i.e. only the self-excited vibration is considered;
2. the motion of the system is harmonic.

These two hypotheses yield to:

$$m\ddot{x} + c\dot{x} + kx = f_{nl}(x) \tag{4.14}$$

with:

$$x = Acos(\omega t + \varphi) \tag{4.15}$$

the harmonic displacement. In order to apply the methodology developed for the lumped parameter model to a complex system such as a bladed disk, it is necessary to reduce the calculation time of a non-linear numerical time integration. For this reason, the Harmonic Balance Method (HBM) is used [77] to solve the equations of motion of the system [77-79]. This is possible due to a harmonic behavior of the aerodynamic forces that involves also a harmonic behavior of the displacement $x$ and the nonlinear forces $f_{nl}$. The harmonic behavior allows to write the time varying quantities in a truncated Fourier series of $H$ orders, where $H$ is the maximum number of harmonics that are considered (see eq. (3.17)). Consequently, the second order, differential equation of motions (4.14) in the time domain can be turned into a complex, algebraic equation in the frequency domain:

$$(-(h\omega)^2 m + ih\omega c + k)\bar{x}^{(h)} = \bar{f}_{nl}^{(h)}, \quad h = 1, \dots, H \tag{4.16}$$

The solution of the equation of motion is necessary but not sufficient to determine the flutter response of the system. This is due to the hypothesis of the absence of

the external force, whereby the frequency of the system is not imposed by the forcing, but by the equilibrium between the aerodynamic energy introduced in the structure by the fluid and the dissipative energy produced on the contact surfaces. Since the unknowns of the problem are two (one displacement value and one frequency value) and the equation of motion is only one, another equation is necessary. The additional equation is the energy balance:

$$E_{aer} = E_{diss} \tag{4.17}$$

where $E_{aer}$ is the aerodynamic energy and $E_{diss}$ is the dissipative energy.

An alternative to the proposed method is the method developed by Petrov in [60]. It is based on a phase normalization to seek for periodic solution. These two methods have been used together in the first part of research to evaluate the more suitable to use into industrial process. In general, they are very similar and have shown similar results and convergence problem. However, the method of the energy balance has been preferred because it is more coherent with the physical behavior of the flutter phenomenon, but also because it is easier to use. In fact, the method proposed by Petrov requires more attention in the definition of the parameters and this is a limit into industrial process where a tool should be as robust as possible. Consequently, these aspects have made the decision pending on the method of energy balance.

The dissipative energy can be calculated starting from the Fourier coefficients of the friction force $\bar{f}_{nl}^{(h)}$. Since the motion of the system has been supposed periodic, the approximation to the first order of the friction force is:

$$f_{nl}(t) = |F_{nl}|\cos(\omega t + \phi) \tag{4.18}$$

where $|F_{nl}|$ is the amplitude of the friction force, while $\phi$ is the phase lag between the amplitude of $x$ and the friction force. In a complex notation it is possible to write:

$$f_{nl}(t) = real(|F_{nl}|e^{i\phi}e^{i\omega t}) \tag{4.19}$$

This means a hysteresis loop that could be substituted by a harmonic force oscillating with the angular frequency of the exciting force (Fig. 4.8) that can be seen as a complex stiffness. The nonlinear force approximated by truncating the

Fourier series to the first order can be divided into two components (Fig 4.9): the first component is proportional to the displacement $x$ and describes an equivalent stiffness of the friction force; while, the second component has a phase delay of $\pi/2$ with respect to $x$ and describes an equivalent damping of the friction force. The whole dissipative effort of the contact is held in the second component of complex stiffness and consequently, the dissipative energy can be easily calculated as the area of the ellipse.

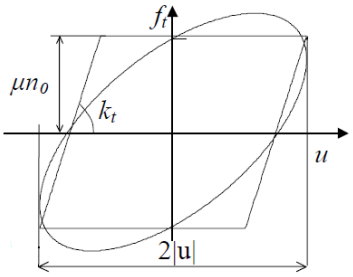


Figure 4.8: Approximation of the hysteresis loop by a harmonic force

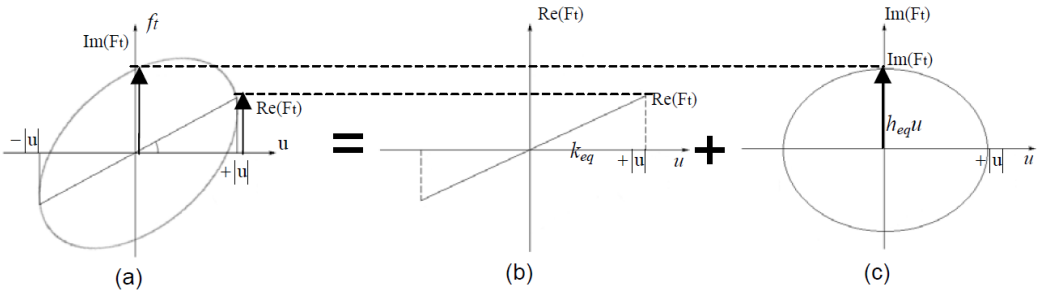


Figure 4.9: two components of the nonlinear force approximated by truncating the Fourier series – (a) equivalent stiffness of the friction force, (b) equivalent damping of the friction force

Mathematically, the steps to obtain the dissipative energy are:

1. First order of the friction force: $f_{nl}^{(1)}$;
2. Complex stiffness: $\bar{k} = f_{nl}^{(1)}/\bar{x}^{(1)}$;
3. Phased friction force: $\overline{F_{nl}} = \bar{k} * |\bar{x}^{(1)}|$;

Finally, the dissipative energy can be written as:

$$E_{diss} = \pi|\bar{x}^{(1)}|imag(\bar{f}_{nl}^{(1)}) \tag{4.20}$$

In the equation (4.20) the Fourier coefficients $\bar{x}^{(h)}$ and $\bar{f}_{nl}^{(h)}$ are expressed for the first harmonic ($h=1$) because the major contribution at the dissipative energy is given by this harmonic, while for the next harmonic the contribution is negligible. Since the damping parameter $c$ is considered as a negative viscous damping, also the aerodynamic energy can be written as the area of an ellipse, i.e.

$$E_{aer} = f_{aer}x = \pi|\bar{x}^{(1)}|imag(i\omega c\bar{x}^{(1)}) \tag{4.21}$$

As the dissipative energy, the major contribution at the aerodynamic energy is given by the first harmonic. In the equation (4.21) it is possible to replace the viscous damping $c$ with the critical viscous damping $\zeta$ that is the usual parameter that is obtained from the CFD flutter analyses:

$$c = 2\zeta\omega \tag{4.22}$$

that substituted in (4.21) gives:

$$E_{aer} = \pi|\bar{x}^{(1)}|imag(i2\zeta\omega^2\bar{x}^{(1)}) \tag{4.23}$$

The eq. (4.20) and (4.23) describe the dissipative and the aerodynamic energies and allow to give an explanation of the trends shown in figures 1.4, 2.11 and 4.3. In fact, from eq. (4.20) it is possible to see that the dissipative energy is proportional to the displacement $x$, while, from eq. (4.23) it is possible to see that the aerodynamic energy is proportional to the square of the displacement $x$ (this link will be better seen in the eq. 4.41).

From now, the aerodynamic critical damping $\zeta$ will be called aero-damping and its symbol will be $\zeta_{aer}$.

### 4.2.1 Result analysis

To permit an easy convergence of the calculation two proper tentative points are defined through the energy balance between the dissipative and the aerodynamic energies (see for example Figure 1.4) using respectively the equations (4.20) and (4.23). A range of displacement $x$ of the body is defined to obtain the two

intersection points, while the pulsation $\omega$ is that with the contact model in the stick condition. This choice of frequency has been made to be coherent with the flutter analysis of a bladed disk performed in the CFD domain; in fact the analyzed mode shape is obtained from a modal analysis of a model that has a rigid root joint, i.e. the nodes on the interfaces are merged with the disk slot.

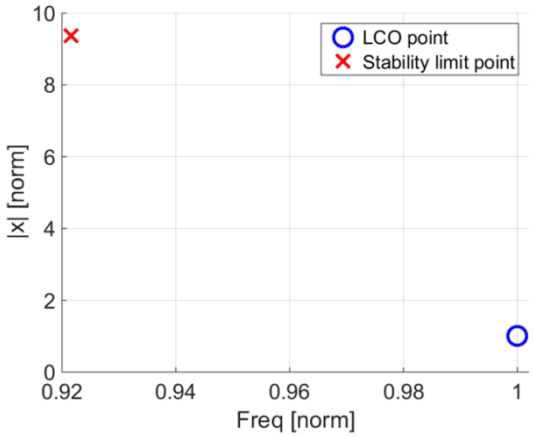


Figure 4.10: Flutter response of the system

These two tentative points are used to initialize the non-linear flutter calculation and the results obtained are reported in Figure 4.10 where the blue ‘o’ marker is the stable solution, while the red ‘x’ marker is the unstable solution. These two points are said stable or unstable through the knowledge obtained from the results of Griffin and Sinha; in fact, from the Figure 4.2 it is possible to see that a stable solution is characterized by small amplitude and high frequency, while the unstable solution is characterized by big amplitude and low frequency. However, to be sure of the stability of these two points, a stability analysis has been performed through the perturbation of two equilibrium points to obtain a range of displacement around the two solutions. For each point in the range of displacements the aerodynamic and dissipative energies have been calculated and the results are reported in Figure 4.11 and 4.12.

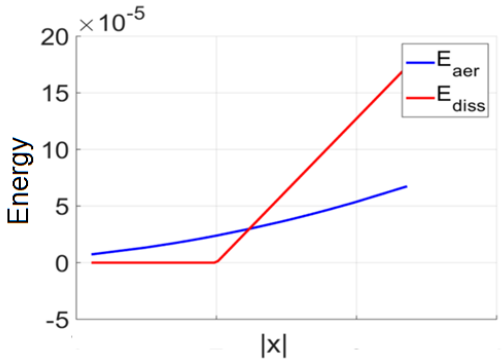


Figure 4.11: Stability analysis of the LCO point

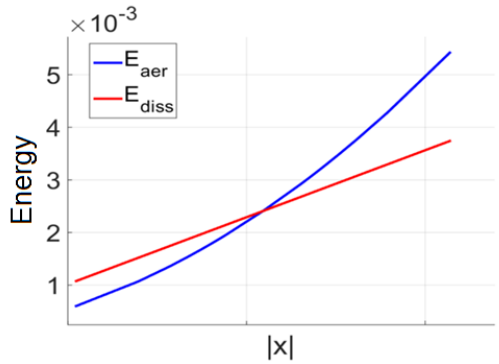


Figure 4.12: Stability analysis of stability limit point

It is possible to see in Figure 4.11 how a perturbation of the amplitude $x$ of the system from the LCO point produces a return at the equilibrium point due to the energy balance, while in the Figure 4.12 a perturbation of the amplitude $x$ of the system from the stability limit point may produce uncontrolled vibration because, for displacements bigger than the stability limit, the aerodynamic energy is always bigger than the dissipative one.

An important result, that can be obtained from Figure 4.10, is the comparison of the flutter frequency with the natural frequency of the system when the friction contact is in the two limit cases (free condition and stick condition). This comparison is made in the table 4.2 showing that the frequency of the stable solution (LCO) is near to the frequency of the system with the contact in stick

condition, while the frequency of the unstable solution (stability limit) is near to the frequency of the system with the contact in free condition.

| | Diff. in Frequency [%] |
|---|---|
| Stability limit vs. free condition | 0.47% |
| LCO vs. stick condition | 0.46% |

Table 4.2: Comparison of frequencies - Stability limit vs. free condition frequencies; LCO vs. stick condition frequencies

These results are important because they show how the contact works in the two equilibrium points. In the LCO point, the contact element is in adherence and a small displacement is sufficient to produce a slip condition (dissipative energy) that is able to balance the aerodynamic energy. This means that the contact has a rigid behavior and the flutter frequency is near to the natural frequency with contact in stick condition. However, the slip condition is predominant on the stick condition and the system is damped. On the contrary, if the system was too stuck, the red curve of dissipative energy in Fig. 4.3 would shift on the right without crossing the curve of the aerodynamic energy. This effect could produce a global unstable condition of the system. In the stability limit point, the contact is still in adherence because the contact model used in this system does not include the lift-off state, however a big $x$ displacement produces a big aerodynamic energy when the contact has a large slip condition to produce the necessary dissipative energy. A large slip condition means that the contact is very loose and as a consequence the flutter frequency is near to the natural frequency with the system in free condition (no contact).

The results obtained in the frequency domain through the HBM and the energy balance are now compared with the results calculated with the direct time integration (DTI) of the equation (4.14). Figure 4.13 shows the results for three different initial conditions: (a) time response with the initial point between 0 and the LCO amplitude, (b) time response with initial point between LCO and stability limit amplitude, and (c) time response with initial point bigger than the stability limit amplitude.

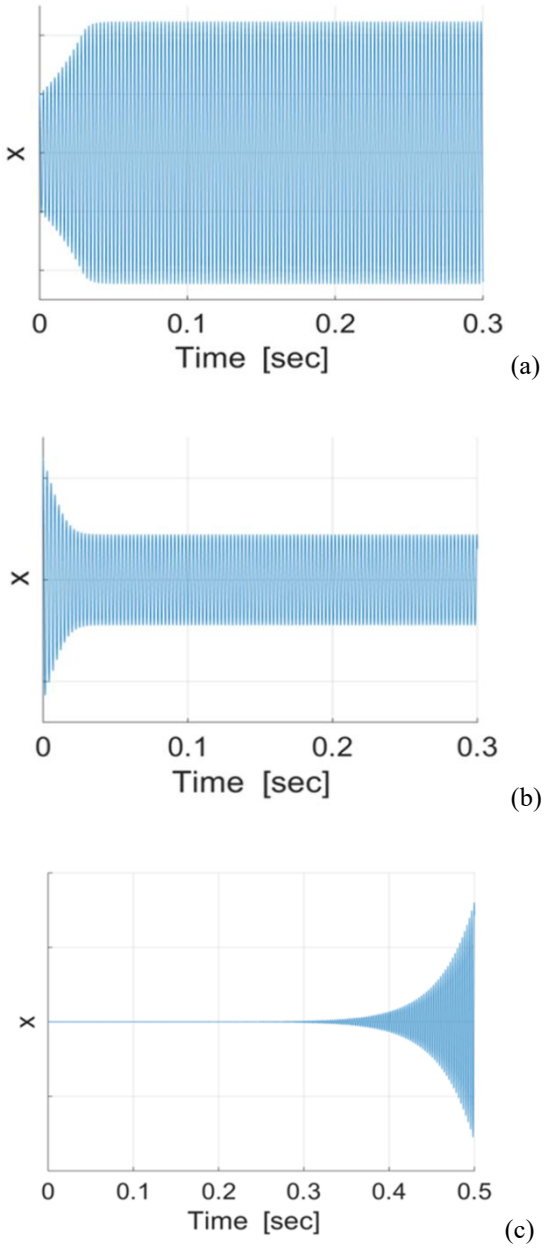


Figure 4.13: Time response of the system - (a) initial point between 0 and the LCO amplitude - (b) initial point between LCO and stability limit amplitude - (c) initial point bigger than stability limit amplitude

It is possible to see that the time responses (a) and (b) reach the limit cycle oscillation while the response (c) gives uncontrolled vibration according to the energy balance shown in Figure 1.4. For the two stable responses, the results obtained in the frequency domain is compared with those obtained in the time

domain in terms of error in amplitude and frequency (Table 4.3). It is possible to see that the both error in amplitude and frequency are very small proving that the approximated solution in the frequency domain is accurate. The small difference in frequency depends by the time discretization in the time domain simulation that has been analyzed with the FFT.

| | Error in Amplitude [%] | Error in Frequency [%] |
|---|---|---|
| Freq. domain vs time domain (a) | 0.04 | 0.07 |
| Freq. domain vs time domain (b) | 0.04 | 0.1 |

Table 4.3: comparison results: frequency vs time domain

### 4.2.4 Parameter variation

The results presented in the preview section are important to understand if the methodology developed works well and gives reliable results. Now, a Parameter variation is performed to understand how the different parameters that enter in the non-linear flutter analysis influence the flutter response of the system.

These parameters are:

- aero-damping ($\zeta_{aer}$);
- friction coefficient ($\mu$);
- normal pre-load ($n_0$);

The first parameter analyzed is the variation of aero-damping (Figure 4.14). The results obtained are similar to those obtained with the formulation of Griffin and Sinha and presented in Figure 4.2, i.e. for small values of aero-damping the system presents small amplitudes of vibration with frequencies close to the natural frequency in stick condition for LCO solution and a large margin of stability. On the contrary, for big values of aero-damping the system presents bigger amplitudes of LCO than the case with small values of aero-damping, but the margin of stability is small. The two curves do not converge at one point because the solutions have difficulties of convergence in proximity of the coalescence of the stable and unstable solutions. This problem of convergence is due to numerical effect on the solver used (function fsolve of MatLab). To provide a

solution of the problem, many interventions have been made such as the variation of the convergence tolerance, the reduction of the step of the aero-damping and the values of the initial solution. However, the problem remained because the system is near the coalescence of the stable and unstable solutions and it is sufficient a little perturbation in the solution to produce a fail on the search for a solution.

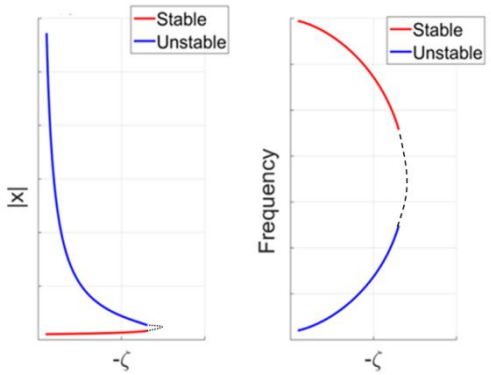


Figure 4.14: variation of aero-damping

In the Figure 4.15 the flutter response is presented by varying the friction and the aero-damping coefficients. For each parameter three values are considered:

- $\mu_1$, $\mu_2$ and $\mu_3$ for the friction coefficient;
- $\zeta_1$, $\zeta_2$ and $\zeta_3$ for the aero-damping;

for a total of 9 points. The used nomenclature for the friction coefficient means $\mu_1$ nominal value, $\mu_2 = 2.5\mu_1$ and $\mu_3 = 3.5\mu_1$, while for he aero-damping $\zeta_1$ is the nominal value, $\zeta_2$=2.5 $\zeta_1$ and $\zeta_3$=3.5 $\zeta_1$.

This type of diagram will be widely used in the future analyses of a real bladed disk to understand the goodness and consistency of the results. In Figure 4.15 it is possible to see that, for a given value of friction coefficient, the amplitude of the LCO increases when the absolute value of the negative aero-damping increases (see for example the three grouped markers). On the contrary, the LCO frequency decreases. These results are consistent with the results of Figure 4.14; in fact, the increase of the aerodynamic energy should be balanced by the increase of dissipative energy that is produced with bigger amplitudes of vibration. At the same time, the LCO frequency decreases since the contact is less rigid when the amount of slip increases. Instead, if the value of the friction coefficient increases

for a given value of the aero-damping coefficient (see for example the blue markers), the LCO amplitude increases while the LCO frequency remains constant. Also this behavior is due to the energy balance of the system; in fact a large value of the friction coefficient determines a more rigid behavior of the contact element and, as a consequence, the necessary amplitude of vibration to produce the dissipative energy increases when the friction coefficient increases. This means that the LCO equilibrium is achieved for bigger displacement amplitudes. This behavior is easily identifiable in Figure 4.16 where the energy balance with two different values of friction coefficient ($\mu_1$ and $\mu_3$) is shown and produce respectively two different LCO equilibrium points.

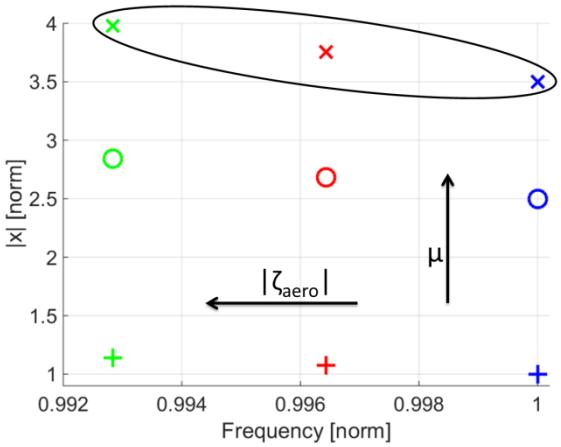


Figure 4.15: LCO response at variation of friction coefficient and aero-damping parameters

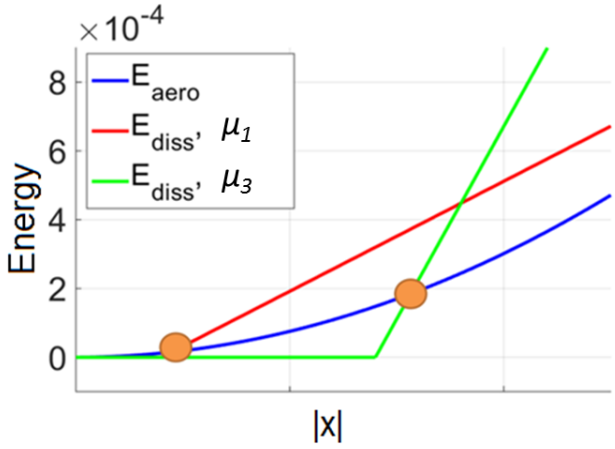


Figure 4.16: energy balance with two different values of friction coefficient

To complete the flutter analysis by varying the friction and the aero-damping coefficients, in Figure 4.17 the trend of the stability limit points is presented. The trend of the flutter response by varying the aero-damping coefficient with a given friction coefficient (same type of marker) is shown in Figure 4.14 (blue line), i.e. the amplitude decreases and the frequency increases if the absolute value of the aero-damping increases. This happens because the total quantity of the aerodynamic energy that the contact can dissipate is lower if the aero-damping coefficient is big in magnitude. As a consequence, a lower amplitude of vibration for the stability limit point is obtained. On the contrary, the increase of the friction coefficient produces an increase of the vibration amplitude of the stability limit point while the frequency is nearly constant (see for example the blue markers). The physical behavior that explains this effect is the same that rules the variation of the friction coefficient in Figure 4.15. The increase of the dissipative energy with the friction coefficient can be seen with the hysteresis loops of the contact model (Figure 4.18a and4.18b) which represents the dissipative energy. However, a big dissipative energy does not mean small amplitude of vibration because this is the result of the equation of motion and the energy balance.

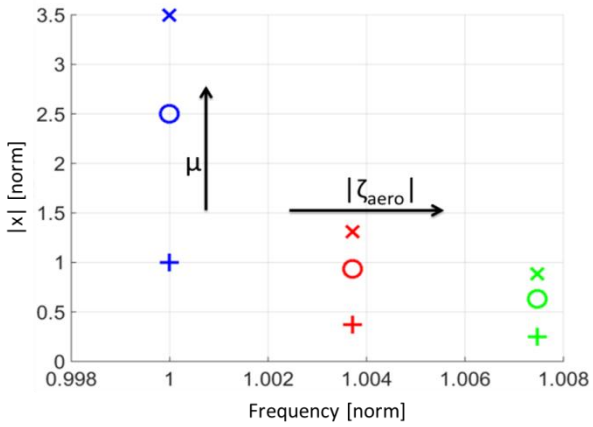


Figure 4.17: stability limit response at variation of friction coefficient and aero-damping parameters

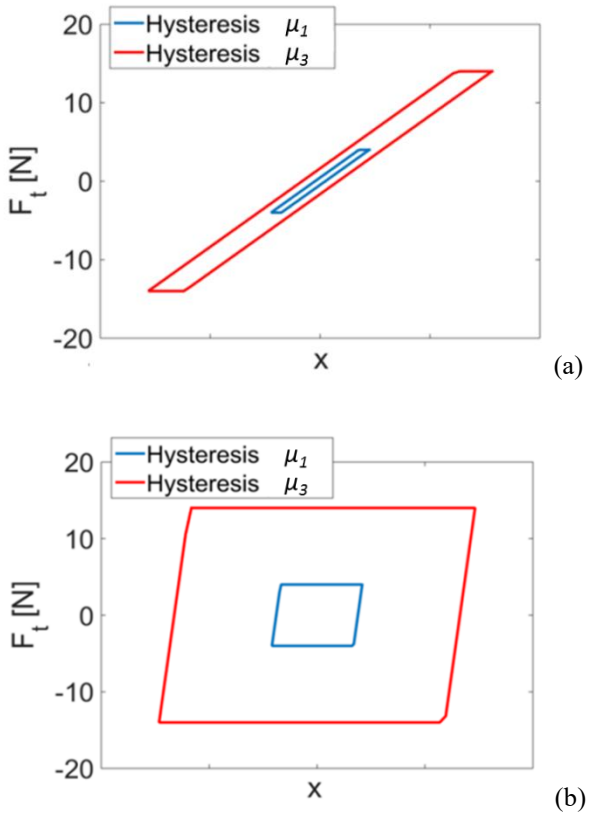


Figure 4.18: Hysteresis loops for two values of friction coefficient μ for the LCO response (a) and stability limit response (b)

Figure 4.19 shows the flutter response in terms of amplitude and frequency for the LCO and stability limit points by varying the normal pre-load $n_0$ on the contact element (see Figure 3.32). These responses have been obtained for given values of aero-damping and friction coefficients. It is possible to see that the increase of the normal pre-load produces an increase of the amplitudes of the flutter response while the frequencies remain near constant. The variation of the normal pre-load acts in the same way of the variation of the friction coefficient, i.e. a large normal pre-load determines a more rigid behavior of the contact element and, as a consequence, the contact element needs bigger displacement amplitude to produce dissipative energy because of the slip state of the contact (the hysteresis loops are similar of those in Figure 4.18).

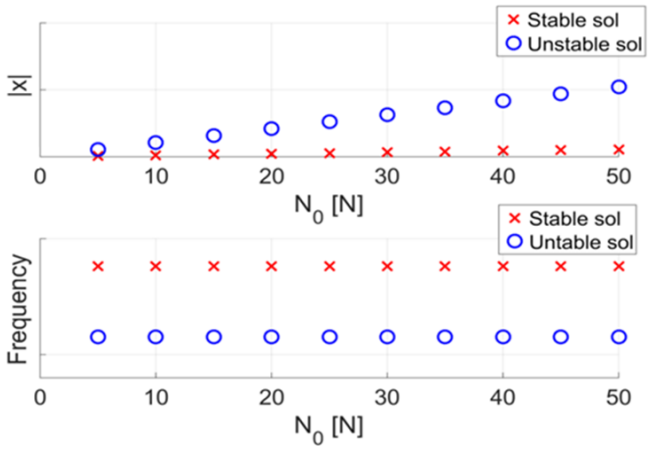


Figure 4.19: flutter response by varying the normal pre-load $N_0$

## 4.3 Bladed disk

The system analyzed in the previous section is a very simplified model that was useful to understand how the flutter response depends on the various parameters such as the aero-damping, the friction coefficient and the normal pre-load. However, this model is not able to represent the dynamic behavior of a bladed disk, therefore a more complex lumped parameter model, characterized by a cyclic symmetric structure, is necessary. These structures have been deeply studied in the 70s by different authors such as Thomas, Wildheim and Mead [86-89] that have analyzed their dynamic behavior.

Figure 4.20 shows a lumped parameter model of a bladed disk where the black points represent the mass of the components (disk and blade), the black lines represent the connection between the mass while the blue lines represent the sectors of the bladed disk. For each sector two mass are presented, one big and one small, that represent respectively the mass of the sector of the disk and the mass of the blade. In total, 12 identical sectors have been considered.

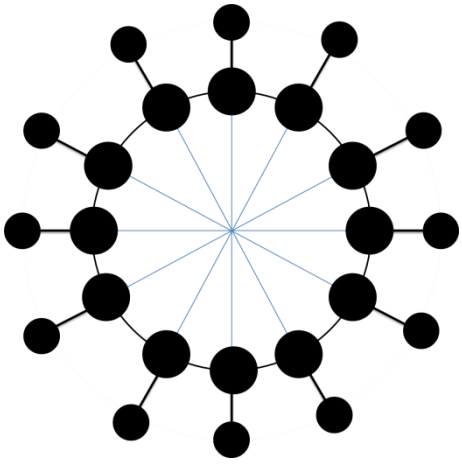

Figure 4.20: Lumped parameter model of a bladed disk

The sector of the bladed disk is illustrated in Figure 4.21:

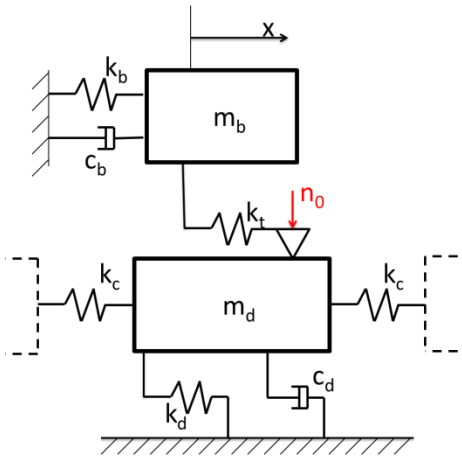


Figure 4.21: Sector of the bladed disk

where $m_d$ and $m_b$ are the mass of the disk and the mass of the blade, $k_d$ and $k_b$ are the respectively stiffness of the disk and of the blade, $k_c$ is the connection stiffness between the sectors and $c_d$ and $c_b$ are the mechanical damping always of the disk and of the blade. Disk and blade are modeled as two separated bodies that are linked together through the contact element to form the bladed disk assembly. The contact element is characterized by a tangential contact stiffness $k_t$ and a normal pre-load $n_0$ and simulates the root-joint interface.

The equation of motion (4.13) is now expressed in matrix form as:

$$[M]\ddot{x} + [C]\dot{x} + [K]x = F_e + F_{aer}(x) + F_{nl}(x) \tag{4.24}$$

where $[M]$, $[C]$ and $[K]$ are the mass, damping and stiffness matrices of the bladed disk, $x$ is the displacements array, $F_e$ is the array of the periodical aerodynamic forces due to the architecture of the engine (number of vanes and blades of the turbine stages), $F_{aer}$ is the non-linear periodical aerodynamic force array acting on the system depending on the blade motion and $F_{nl}$ is the array of the non-linear forces generated by friction contacts that also depends on the blade motion $x$.

The matrices $[M]$ and $[K]$ are the total mass and stiffness matrices of the whole system in Figure 4.20. They are composed by:

$$[M] = \begin{bmatrix} [M]_{S,1} & 0 & 0 \\ 0 & \ddots & 0 \\ 0 & 0 & [M]_{S,N} \end{bmatrix}$$

$$[K] = \begin{bmatrix} [K]_{S,1} & [K]_C & 0 & [K]_C \\ [K]_C & \ddots & \ddots & 0 \\ 0 & \ddots & \ddots & [K]_C \\ [K]_C & 0 & [K]_C & [K]_{S,N} \end{bmatrix} \tag{4.25}$$

where $[M]_{S,i}$ and $[K]_{S,1}$ are the mass and stiffness matrices of a generic sector, while $[K]_C$ is the connection stiffness matrix between the sectors. These matrices have the following structure:

$$[M]_{S,i} = \begin{bmatrix} m_d & 0 \\ 0 & m_b \end{bmatrix}$$

$$[K]_{S,i} = \begin{bmatrix} k_d + 2k_c & 0 \\ 0 & k_b \end{bmatrix} \tag{4.26}$$

$$[K]_C = \begin{bmatrix} -k_c & 0 \\ 0 & 0 \end{bmatrix}$$

The damping matrix $[C]$ is calculated starting from the modal damping ratio using the equation (4.27):

$$[C] = inv[\Psi^H] * (2 * \zeta_m * [\omega_n]) * inv[\Psi] \tag{4.27}$$

where $\zeta_m$ is the structural modal damping ratio, $[\omega_n]$ is the matrix of the natural pulsations of the system and $[\Psi]$ is the matrix of the eigenvectors of the whole system. The natural pulsations and the eigenvectors are obtained from a modal analysis of the system where the contact works in the stick condition, i.e. disk and blade are joined together through a spring of stiffness $k_t$. In this condition, the stiffness matrix of the sector is:

$$[K]_{s,i} = \begin{bmatrix} k_d + 2k_c + k_t & -k_t \\ -k_t & k_b + k_t \end{bmatrix} \tag{4.28}$$

The matrices $[\omega_n]$ and $[\Psi]$, so obtained, describe the dynamic behavior of bladed disk. Since each sector is identical to the other, the bladed disk is said tuned and it is characterized by the property of cyclic symmetry. Therefore, it is possible to define an *IBPA* that represents the phase delay between a sector and its adjacent (eq. 2.4). The *IBPA* is closely linked to the nodal diameter (ND) and in cyclic symmetry structure it is possible to have:

$$\begin{aligned} &0 \leq ND \leq \tfrac{N}{2}, \ if\ N\ is\ even \\ &0 \leq ND \leq \tfrac{N-1}{2}, \ if\ N\ is\ odd \end{aligned} \tag{4.29}$$

Each nodal diameter is characterized by two stationary modes with the same shape and the same natural frequency, but with a phase of 90 degree. The exceptions are the ND=0 and ND=N/2 (if exists) that are characterized only by one stationary mode and one natural frequency. The double modes can be combine together to obtain two rotational modes:

$$\varphi_{1,2} = \psi_1 \pm i\psi_2 \tag{4.30}$$

where $\varphi_{1,2}$ is the pair of rotational modes, $\psi_1$ and $\psi_2$ are the double stationary modes and $i$ is the imaginary unit.

For the considered lumped parameter model of bladed disk, the number of ND is equal to 6 and each ND has two different mode shapes; in the first mode the motion of disk and blade are concord while in the second mode the motion of disk

and blade are opposite. In the table 4.4 the natural frequencies of the system with the contact in stick condition are reported for the all nodal diameters.

| | Stick condition | |
|---|---|---|
| ND | Freq 1° mode [norm] | Freq 2° mode [norm] |
| 0 | 0,441 | 1,125 |
| 1 | 0,999 | 11,478 |
| 2 | 0,999 | 22,159 |
| 3 | 0,999 | 31,334 |
| 4 | 0,999 | 38,374 |
| 5 | 0,999 | 42,801 |
| 6 | 1 | 44,310 |

Table 4.4: Natural frequencies of the system in stick condition for the all nodal diameters

The natural frequencies by varying the nodal diameters are usually reported in a ZZENF diagram (Figure 4.22) where on the Cartesian axes there are the nodal diameters and the natural frequencies. This graphic is useful because groups together the different modal families.

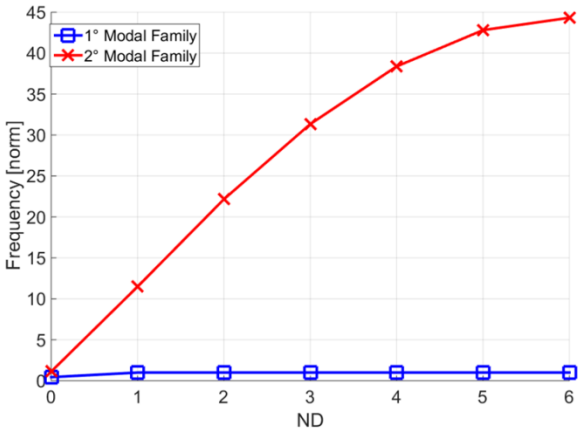


Figure 4.22: ZZENF diagram

The modal displacements of the first modal family for the nodal diameters 0, 1 and 6 are shown in Figure 4.23 (only the modal displacements of the blades are shown). It is possible to see that for ND=0 (Figure 4.23a) the blades have the

same modal displacements, while for ND=6 (Figure 4.23c) the blades have a pattern of displacements equal to ‘maximum, minimum, maximum,…’. Instead, for ND=1 (Figure 4.23b) it is possible to see the two double stationary modes with the phase of 90 degree.

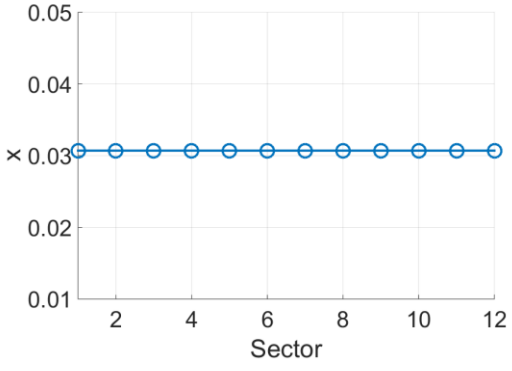


(a)

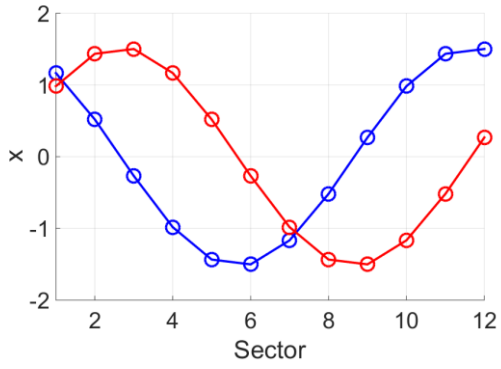


(b)

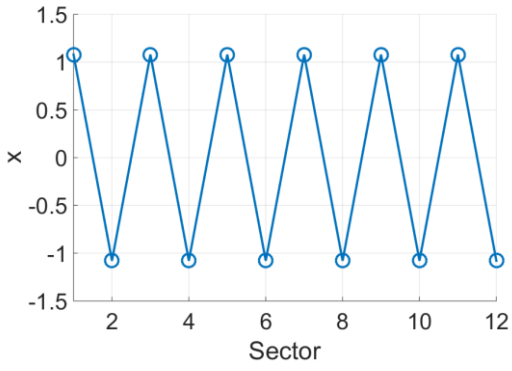


(c)

Figure 4.23: Modal displacement of the blades for (a) ND=0, (b) ND=1 and (c) ND=6

For each mode at every nodal diameter, the aero-elastic coefficient ($\zeta_{aer}$ and $\eta_{aer}$) can be calculated (see Figure 2.10) in CFD domain. Of these values, only the more unstable value will be taken into account to simplify the flutter analysis. This choice was made because a great attention should be taken on the calculation of the contact forces when more unstable ND exist. This is mainly due to the fact that, for a real bladed disk with many sectors (usually more than one hundred), unstable mode shapes are characterized by ND values close to each other and therefore they are not multiple of each other. For this reason, the motion of the blade is not more strictly periodic around one rotation of the disk and as a consequence a simple HBM method cannot be used. A n-dimensional FFT should be used to consider the presence of 'n' unstable nodal diameters with consequence extension of the calculation time that becomes critical when more than two ND are considered.

Since the calculation of the aerodynamic force $F_{aer}$ is made through the hypothesis of small perturbations, the RANS equations can be linearized and the vector $F_{aer}$ can be written as:

$$F_{aer} = [AM]x \tag{4.31}$$

where $[AM]$ is the aerodynamic matrix that includes the aero-damping ($\zeta_{aer}$) and aero-stiffness ($\eta_{aer}$) coefficients modeling the linearized coupling between fluid and structure. Besides, when self-excited vibrations occur, it is usually assumed that the contribution of the external excitation is negligible, for this reason $F_e$ can be set to zero and the equation (4.24) can be written as:

$$[M]\ddot{x} + [C]\dot{x} + [K]x + [AM]x = F_{nl}(x) \tag{4.32}$$

The aerodynamic matrix $[AM]$ can be defined as a hysteretic damping that has two components:

- the first holds the terms that define the aero-stiffness acting on the dofs of the blade;
- the second holds the terms that define the aero-damping acting on the dofs of the blade.

These two components are defined in the following way:

$$[K_{aer}] = -real([AM])$$
$$[C_{aer}] = -imag([AM])/\omega \tag{4.33}$$

i.e. the linearized aerodynamic matrix $[AM]$ can be written as:

$$[AM] = -[K_{aer}] - i\omega[C_{aer}] \tag{4.34}$$

Usually the aero-elastic coefficients ($\zeta_{aer}$ and $\eta_{aer}$) are given as modal ratios, therefore the aero-dynamic matrix $[AM]$ can be written in the modal domain by:

$$[am_{mod}] = [\Psi^H] * [AM] * [\Psi] \tag{4.35}$$

where $[am_{mod}]$ the modal aerodynamic matrix. $[am_{mod}]$ is in general a full matrix that includes two types of elements, the direct-coupling terms and the cross-coupling terms. The firsts are placed on the diagonal of the matrix and describe the aero-elastic coefficients calculated for each mode shape at proper aerodynamic field, while the seconds are placed out of the diagonal and describe the aero-elastic coefficients calculated between a mode shape and aerodynamic fields of the other modes. In this thesis only the elements on the diagonal will be considered because the used aerodynamic code is not able to calculate the cross-coupling terms.

For these reasons the modal matrix $[am_{mod}]$ has a diagonal form where only the elements of the diagonal have a value different from zero:

$$[am_{mod}] = \begin{bmatrix} -2m_1\omega_1^2(\eta_{aer,1} + i\zeta_{aer,1}) & 0 & 0 \\ 0 & \ddots & 0 \\ 0 & 0 & -2m_n\omega_n^2(\eta_{aer,n} + i\zeta_{aer,n}) \end{bmatrix} \tag{4.36}$$

In eq. (4.36) $m$ is modal mass and $\omega$ is the natural pulsation.

The passage from the modal form to the physical form is easy and it involves the inverse operation of the equation (4.35), i.e.:

$$[AM] = inv[\Psi^H] * [am_{mod}] * inv[\Psi] \tag{4.37}$$

It is possible to find a correspondence between the definition of the aerodynamic matrix in terms of hysteretic damping and the definition of aero-damping as viscous damper given in the previous section. In fact, from the equations (4.34) and (4.35) it is possible to write the modal aerodynamic matrix as:

$$[am_{mod}] = -\left[k_{aer,mod}\right] - i\omega\left[c_{aer,mod}\right] \tag{4.38}$$

that matched with (4.36) and applying the definition in (4.33) gives:

$$\begin{aligned}\left[k_{aer,mod}\right] &= \begin{bmatrix} 2m_1\omega_1^2\eta_{aer,1} & 0 & 0 \\ 0 & \ddots & 0 \\ 0 & 0 & 2m_n\omega_n^2\eta_{aer,n} \end{bmatrix} \\ \left[c_{aer,mod}\right] &= \begin{bmatrix} 2m_1\omega_1\zeta_{aer,1} & 0 & 0 \\ 0 & \ddots & 0 \\ 0 & 0 & 2m_n\omega_{n1}\zeta_{aer,n} \end{bmatrix}\end{aligned} \tag{4.39}$$

Usually the modal mass is equal to 1 and the terms in $\left[c_{aer,mod}\right]$ become equal to that in the equation (4.22) obtained from a definition of aero-damping as viscous damper.

As made for the one dof system, the HBM is applied and the second order, differential Equation of motions (4.32) in the time domain can be turned into a set of complex, algebraic equation in the frequency domain:

$$\begin{aligned}&(-(h\omega)^2[M] + ih\omega([C] + [C_{aer}]) + [K] + [K_{aer}])\bar{x}^{(h)} = \\ &F_{nl}^{(h)}, \qquad h = 1, \dots, H\end{aligned} \tag{4.40}$$

Since the external force is absent, the frequency of vibration of the system is not known at priori, therefore the energy balance equation (4.17) is alongside the equation of motion to have a well-conditioned problem. In this case the aerodynamic energy is written as:

$$E_{aer} = \pi * imag\left((\bar{x}^{(1)})^H * F_{aer}\right) = \pi * imag\left((\bar{x}^{(1)})^H * [AM] * \bar{x}^{(1)}\right) \tag{4.41}$$

while the dissipative energy is the sum of the structural dissipative energy associated with the material of the bladed disk and the energy dissipated by the contact elements of every sector.

$$E_{diss} = E_{diss,str} + E_{diss,cont} \tag{4.42}$$

The energy dissipated by the mechanical damping of the structure is written in the same way of aerodynamic energy, i.e.:

$$E_{diss,str} = \pi * imag\left((\bar{x}^{(1)})^H * i\omega[C] * \bar{x}^{(1)}\right) \tag{4.43}$$

while the energy dissipated by the contact elements is:

$$E_{diss,cont} = \sum_{i=1}^{N_c} \pi |\bar{u}_i{}^{(1)}| imag(\bar{F}_{nl,i}^{(1)}) \tag{4.44}$$

where $\bar{u}_i{}^{(1)}$ is the 1st order complex relative tangential displacement of the i-th contact element ($\bar{u}_i{}^{(1)} = \bar{x}_{b,i}{}^{(1)} - \bar{x}_{d,i}{}^{(1)}$) and $N_c$ is the total number of contact elements (in this case is equal to the number of sectors). As happened for the system at one dof, the complex coefficients of the Fourier transformation have get to first order in the energy balance because the most quantity of energy is linked to this order.

## 4.3.1 Result analysis

To permit an easy convergence of the calculation, two proper tentative points are defined through the energy balance between the dissipative (including friction forces and structural damping) and the aerodynamic energy (see for example Figure 1.4) using respectively the equations (4.41), (4.43) and (4.44). This calculation is performed varying the complex modal coordinate at first order $\bar{q}^{(1)}$ that multiplies the unstable mode $\psi_i$ of the bladed disk in according with:

$$\bar{x}^{(1)} = \bar{q}^{(1)} * \psi_i \tag{4.45}$$

The unstable mode considered is the first mode of a fixed nodal diameter. The other modes are not considered in this first energy balance because it is assumed that the main energetic contribution to flutter is only given by the unstable mode.

The results have been obtained for ND=2 and they are shown in Figure 4.24 for all the blades. The blue 'o' marker represents the stable solution, while the red 'x' marker represents the unstable solution. In the next figures, only the vibration amplitude of the blades will be plotted.

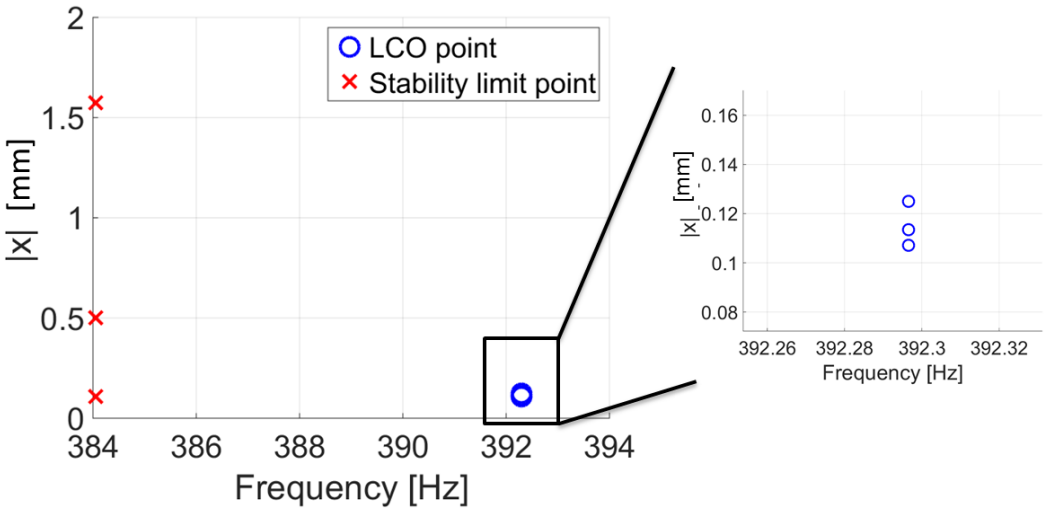


Figure 4.24: Flutter response of a bladed disk

It is possible to see in Figure 4.24 for both solutions, stable and unstable, that the amplitudes $|x|$ are not equal for all blades, but that they are grouped in three groups, while all the blades have two different frequencies in according with the type of solution (stable or ynstable). The calculated flutter response is not correct because, in a cyclic symmetry structure such as the bladed disk, each sector should be subject to the same value of amplitude of vibration at different time depending by IBPA. Besides, the smaller amplitudes of the stability limit response have about the same value of the LCO amplitude, but at different frequency and this does not represent a physical behavior of the bladed disk when the self-excited vibrations occur (if the amplitude are equal also the frequency will be equal).

The problem behind this result is the type of modal base taken into account to build the aerodynamic matrix $[AM]$, in fact stationary modes have been used. Since the flutter is a circular phenomenon that presents the traveling waves in one direction and in the other, the right modal base should be contained rotating modes to be coherent with the physical phenomena.

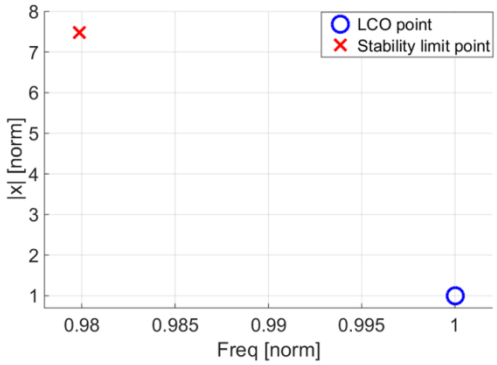


Figure 4.25: flutter response with rotating modes

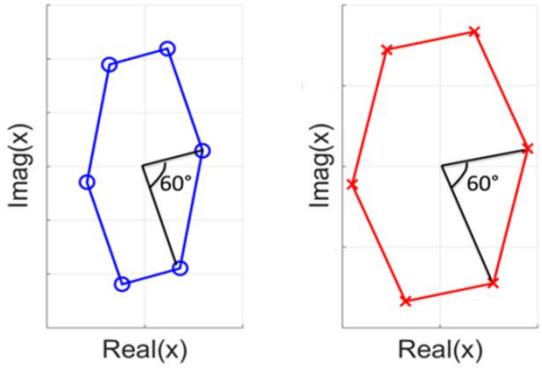


Figure 4.26: rotation of the displacement $x$ of the blades – right: LCO solution – left: stability limit solution

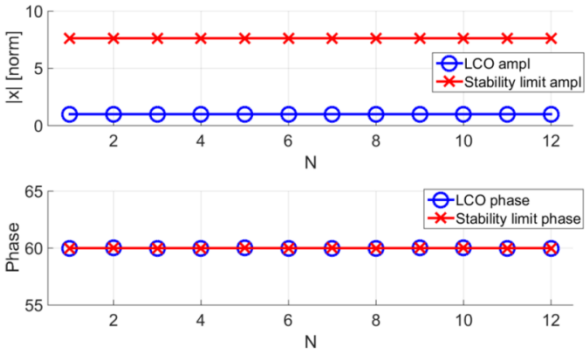


Figure 4.27: Amplitude and phase of each sector

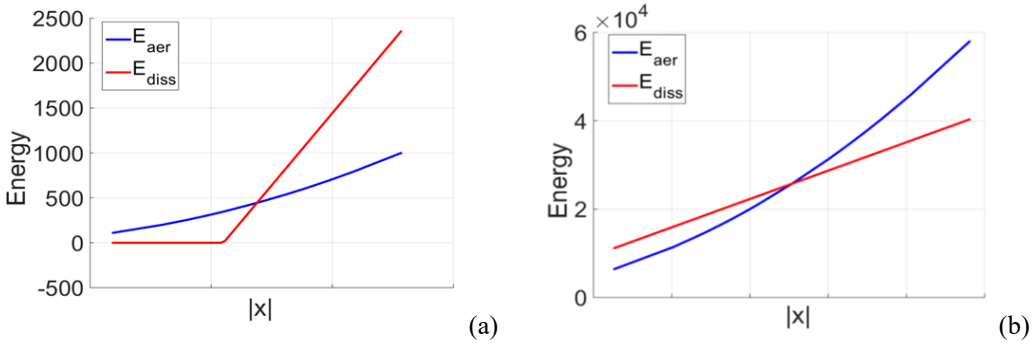


Figure 4.28: Stability analysis of LCO solution (a) and stability limit (b)

Figure 4.25 shows the flutter response in terms of frequency and amplitude with the utilization of the rotating modes in the modal base. Instead, Figure 4.26 shows the rotation of the displacements vector $x$ of the blades. Only 6 points are shown for the two solutions instead of 12 because ND=2 (for example, if the nodal diameter have been 1, the Figure 4.26 would have shown 12 points, for ND=3 the points would be 4 and etc.). This response is correct, in fact the blades are subject to the same value of amplitude of vibration at different time depending by IBPA (Figure 4.27). The stability of two solutions is then checked in Figure 4.28a for the LCO response and Figure 4.28b for the stability limit.

The results obtained in the frequency domain will be now compared with the results calculated with the DTI of the equation (4.32). Figure 4.29a shows the time response that reach the limit cycle oscillations. It is possible to see that after a transient period all the blades reach the LCO amplitude but at different time (Figure 4.29b), while the Figure 4.30 shows an uncontrolled vibration. In this case, the starting point is an amplitude bigger than the amplitude of the stability limit and consequently the response of the system can be only unstable. For completeness of the flutter analysis, the time response with the aerodynamic matrix [$AM$] built with stationary modes is shown in Figure 4.31. This figure shows that the blades reach three different values of LCO amplitude instead of one value as well as predicted by the calculation in the frequency domain.

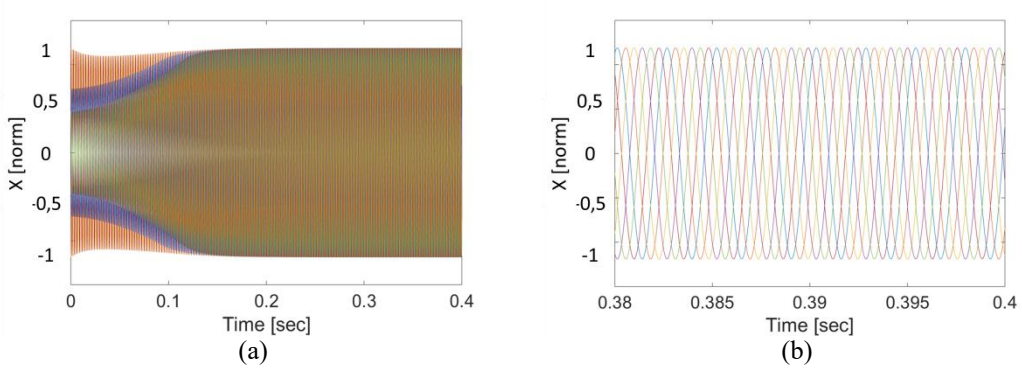


Figure 4.29: Stable time response of a bladed disk (a) and zoom (b)

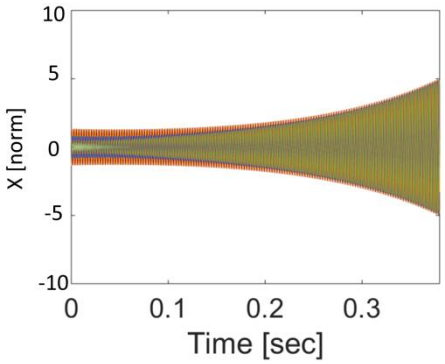


Figure 4.30: Unstable time response of a bladed disk

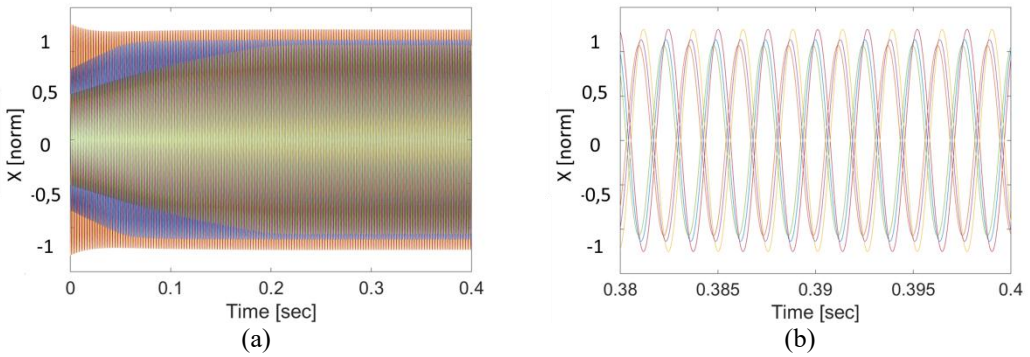


Figure 4.31: Stable time response of a bladed disk with stationary modes (a) and zoom (b)

Table 4.5 shows the comparison of LCO solution in frequency and time domains. The comparison is performed in terms of percentage error in amplitude and in frequency for every blade. It is possible to see that the error in frequency is equal for every blade, while the error in amplitude presents small difference due to small numerical errors occurring in the calculation. However, the error obtained are overall very small and this means that the approximation solution calculated in frequency domain is accurate.

| Blade | Error in Amplitude [%] | Error in Frequency [%] |
|---|---|---|
| 1 | 0,007 | 0,1 |
| 2 | 0,006 | 0,1 |
| 3 | 0,005 | 0,1 |
| 4 | 0,007 | 0,1 |
| 5 | 0,006 | 0,1 |
| 6 | 0,005 | 0,1 |
| 7 | 0,007 | 0,1 |
| 8 | 0,006 | 0,1 |
| 9 | 0,005 | 0,1 |
| 10 | 0,007 | 0,1 |
| 11 | 0,006 | 0,1 |
| 12 | 0,005 | 0,1 |

Table 4.5: comparison of results in frequency and time domains

### 4.3.2 Parameter variation

The results presented in the previous section show properties similar to those obtained for one dof system and this means that the flutter phenomenon for a bladed disk has been correctly interpreted. Now, a Parameter variation is performed to see if the different parameters that enter in the non-linear flutter analysis influence the flutter response of the system in the same way occurring in the one dof system.

These parameters are:

- aero-damping ($\zeta_{aero}$);

- friction coefficient (μ);
- normal pre-load ($n_0$);

Because in the lumped parameter model of bladed disk the mechanical damping ($\zeta_m$) has been included, the influence of this parameter on the flutter response will be also studied. Besides, the influence on the LCO response by varying the nodal diameter of the system will be also analyzed in this section.

Figure 4.32 shows how the flutter response changes at the variation of aero-damping coefficient. The figure shows the typical trend of flutter response at variation of aero-damping. In fact the stable and unstable lines tend to join in one point. Figure 4.33 focuses the attention on the stable line at low values of aero-damping; in this way it is possible to see that the amplitude of the response goes to zero by gradually reducing the aero-damping until it is equal to the structural damping: in this case the only solution possible is the trivial solution because the energy introduced by flutter is always balanced by the dissipative energy of the material, i.e. the system is always stable.

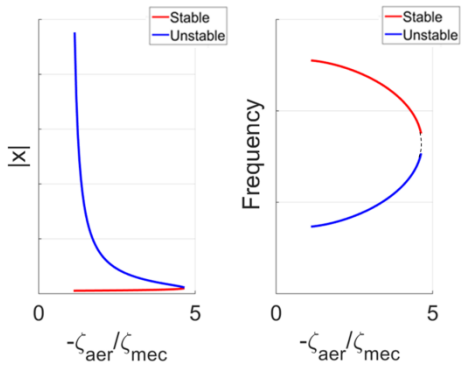


Figure 4.32: variation of aero-damping

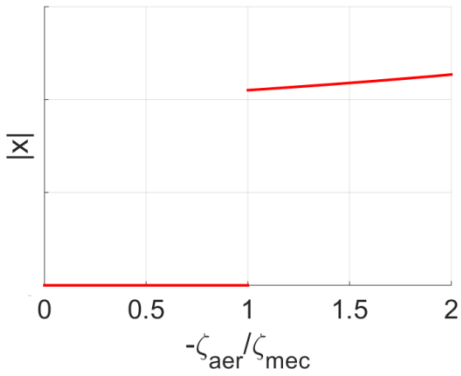


Figure 4.33: Stable solution at low values of aero-damping

As it happened before for the same analysis, the two solutions of Figure 4.32 do not converge at one point because the code developed has difficulties of convergence in proximity of the coalescence of the stable and unstable solutions.

Figure 4.34 shows the LCO flutter response at variation of friction and aero-damping coefficients. The value adopted for friction coefficient are those of the previous section, while for the aero-damping coefficient the value are $\zeta_1$ nominal value, $\zeta_2$=1.67 $\zeta_1$ and $\zeta_3$=2.34 $\zeta_1$. The shown trend is the same obtained in Figure

4.15 where one dof system was considered, i.e. the increase of friction coefficient produces an increase of vibration amplitude while the frequency remains constant. This trend depends from the behavior of the contact elements that can be more or less stiff in according with its friction coefficient. In fact, the amplitude of vibration increases due to the aerodynamic energy introduced in the system that is proportional to the square of the amplitude itself, until the contact changes its state from the stick state to the slip state and the dissipative energy is produced. This change of contact state depends from the friction coefficient and in particular this happens for smaller amplitude if the friction coefficient is small.

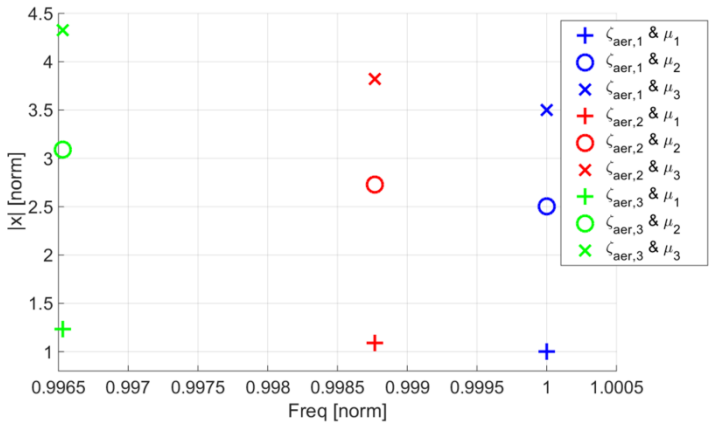


Figure 4.34: LCO response at variation of friction and aero-damping coefficients

In Figure 4.35 the flutter response in terms of amplitude and frequency of vibration for the LCO solution by varying the normal pre-load $n_0$ that acts on the contact element (see Figure 3.3 of Chapter 3) is shown. Fixed values of aero-damping and friction coefficient have been used. As it happened for the one dof system, the increase of the normal pre-load produces an increase of amplitudes of flutter response while the frequencies remain near constant. In fact, the normal pre-load acts on the contact element in the same way of the friction coefficient, i.e. it influences the behavior of the contact. An high value of normal pre-load means a more rigid behavior of the contact, on the contrary a low value of the normal pre-load means a less stiff behavior. This influences the production of dissipative energy in the same way described before for the friction coefficient.

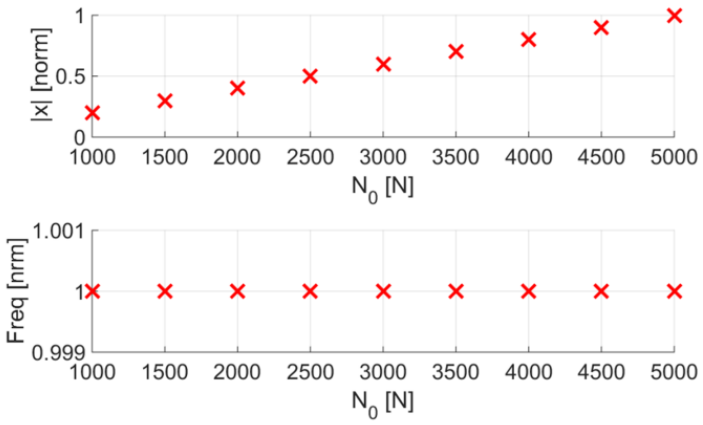


Figure 4.35: LCO flutter response by varying the normal pre-load $N_0$

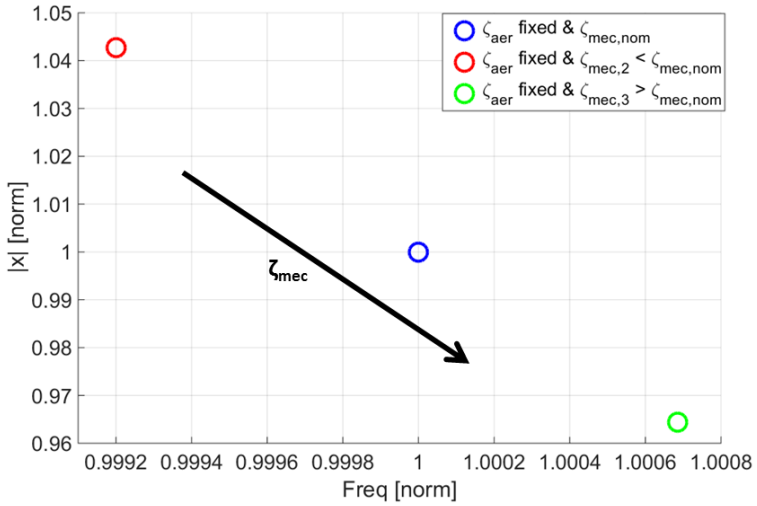


Figure 4.36: LCO response by varying $\zeta_{mec}$ ($\zeta_{mec,2}$=0.75$\zeta_{mec,nom}$ and $\zeta_{mec,3}$=1.25$\zeta_{mec,nom}$)

Figure 4.36 shows the influence of the mechanical damping $\zeta_{mec}$ on the flutter response of the stable solution where fixed values of aero-damping and friction coefficient have been used. It is possible to see that the increase of mechanical damping produces a variation of LCO solutions opposite to that of aero-damping. This happens because a part of aerodynamic energy is always balance by the

structural dissipative energy while the remaining energy is balance by the contact. In this condition, the bladed disk sees a total viscous damping equal to:

$$\zeta_{aer,purged} = \zeta_{aer} + \zeta_{mec} \tag{4.46}$$

that is balanced by the friction forces. Consequently, the variation of $\zeta_{aer}$ or the variation of $\zeta_{mec}$ represent the same thing. Figure 4.37 provides the comparison between the LCO result of the system in nominal condition ($\zeta_{aer,2}$ & $\zeta_{mec,nom}$) and the LCO result of an equivalent system where the mechanical damping is null and the aero-damping is given by equation (4.46). The figure shows that the two results are coincident because the energy balance is not change although the parameters are different.

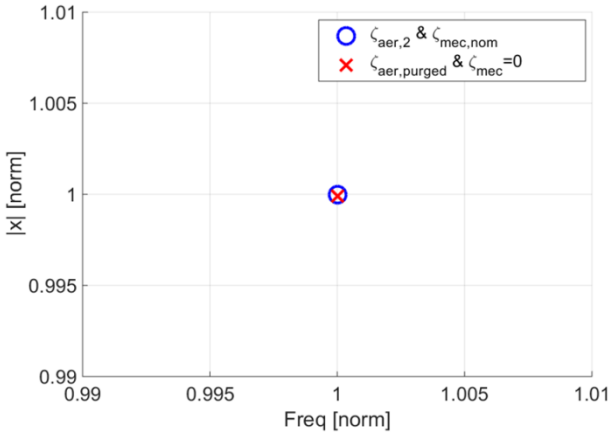


Figure 4.37: the comparison between result of the system in nominal condition and the result of an equivalent system

Fig 4.38 shows the variation of the LCO response by varying the nodal diameter of the model while the values of the friction and aero-damping coefficients have not changed in the different simulations. It is possible to see that, by varying the ND unstable at flutter from 1 to 6, the LCO response is characterized by a reduction of amplitude and an increase of frequency. This is due to the fact that a bigger ND produces a stiffening effect of the disk, while the blade sees the same level of instability (the aero-damping is not changed). Consequently, the relative displacement of the contact has a slight increase in accordance with the ND and this is traduced in smaller amplitudes and bigger frequencies to achieve the LCO.

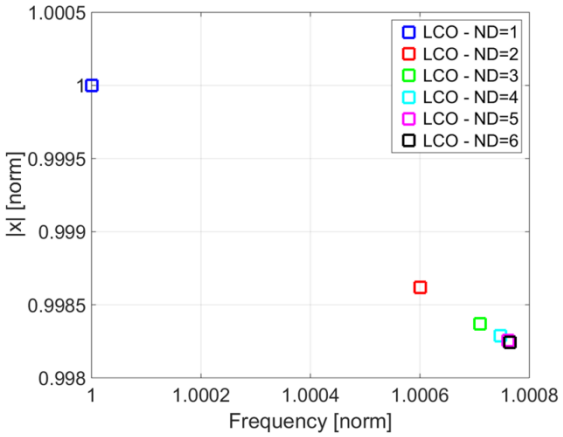


Fig 4.38: LCO response by varying the nodal diameter

## 4.4 Sector of a bladed disk in cyclic symmetry

A real bladed disk modeled at FEM has millions of degrees of freedom and this involves difficulties in managing the matrices and long calculation times. For this reason, a common practice is to study a fundamental sector of a bladed disk reduced in cyclic symmetry. In this section the lumped parameter model of a bladed disk shown in Figure 4.20 will be reduced in cyclic symmetry and then flutter analyses will be performed.

The cyclic symmetry reduction can be performed in different way. In general, the starting point is to consider a cyclic symmetry structure that is made from N sectors (Figure 4.20). If 'x' is the vector of the physical coordinates of each sector, it is possible to write, for each nodal diameter of the whole system, the discrete Fourier transformation (DFT) of the physical coordinates as:

$$\bar{x}^{(n)} = \frac{1}{N}\sum_{s=1}^{N} x_s e^{-i\,s\,IBPA} \tag{4.47}$$

where $n$ is the nodal diameter considered, $x_s$ is the physical displacement of a generic sector $s$ and $IBPA$ is the inter-blade phase angle. The physical coordinates can be obtained from the inverse discrete Fourier transformation (IDFT):

$$x_s = \sum_{n=1-N/2}^{N/2} \bar{x}^{(n)} e^{i\,s\,IBPA} \tag{4.48}$$

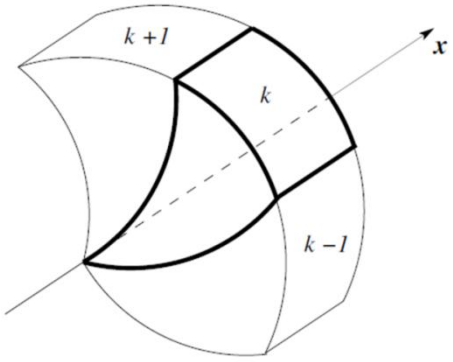


Figure 4.39: general cyclic symmetry structure

The studied bladed disk has 12 sectors that are made of 2 components which have one degree of freedom. Therefore, it is possible to write a reduction matrix $[T_{cs}]$ that links the global displacements of the bladed disk to the displacements of the sector as:

$$x = [T_{CS}] \begin{Bmatrix} x_{d,cs} \\ x_{b,cs} \end{Bmatrix} = [T_{CS}] x_{CS} \tag{4.49}$$

where $x_{CS}$ is the vector of dofs of the sector reduced in cyclic symmetry ($x_{d,cs}$ and $x_{b,cs}$ are respectively the dof of the disk and dof of the blade). The matrix $[T_{cs}]$ can be written in according to the equation (4.47) as:

$$[T_{CS}] = \begin{bmatrix} 1 & 0 \\ 0 & 1 \\ e^{-iIBPA} & 0 \\ 0 & e^{-iIBPA} \\ \vdots & \\ e^{-i(N-1)IBPA} & 0 \\ 0 & e^{-i(N-1)IBPA} \end{bmatrix} \tag{4.50}$$

The equation (4.49) is substituted in the equation of motion (4.32) to obtain the reduced matrices in according to the equations (3.2) of the Chapter 3. The equation of motion (4.32) becomes:

$$[m_{CS}]\ddot{x}_{CS} + [c_{CS}]\dot{x}_{CS} + [k_{CS}]x_{CS} + [am_{CS}]x_{CS} = f_{nl,CS}(x_{CS}) \tag{4.51}$$

where $[m_{CS}]$, $[c_{CS}]$ and $[k_{CS}]$ are the mass, damping and stiffness matrices, $[am_{CS}]$ is the aerodynamic matrix and $f_{nl,CS}(x)$ is the vector of non-linear forces. All these elements are reduced in cyclic symmetry, i.e. they depend on a determined *ND*, and have a dimension 2x2 for the matrices and 2x1 for the vectors.

The modal analysis of the cyclic symmetry sector allows to calculate the eigenvalues $[\omega_{n,CS}]$ and the eigenvectors $[\Psi_{CS}]$ of the system for a given nodal diameter. To be coherent with the flutter analysis made in the previous section, the chosen ND is equal to 2. The results of modal analysis are:

| | Freq. CS / Freq. BD |
|---|---|
| 1° mode | 1 |
| 2° mode | 1 |

Table 4.6: ratio of natural frequencies between the system in cyclic symmetry (CS) and the full bladed disk (BD)

| 1° mode eigenvector | 2° mode eigenvector |
|---|---|
| -7,48e-5 | -1.73 |
| -3.73 | 1.62e-4 |

Table 4.7: eigenvectors of the system reduced in cyclic symmetry

Table 4.6 shows the ratio of the natural frequencies between the system reduced in cyclic symmetry and the full bladed disk. It is possible to see that the ratio is equal to 1, i.e. the frequencies are the same. Table 4.7 shows, instead, the modes shape of the reduced system with the contact in stick condition. The mode shapes of two systems are equal, in fact the first mode has concord displacements for the blade and the disk, while in the second mode the displacements are opposite. However, to compare the eigenvectors of two systems, the reduced eigenvectors should be

expanded; in this way it is possible to see the trend in the space of the displacements on the whole system. The expansion is performed using the following equation:

$$[\Psi_{ex}] = [T_{CS}][\Psi_{CS}] \tag{4.52}$$

where $[\Psi_{ex}]$ is the matrix of the expanded eigenvectors. These eigenvectors are rotating because the IBPA has been imposed in the construction of the matrix $[T_{CS}]$; therefore, the comparison will be made with the rotating modes of the full system. If the ratio between the two modes (expanded and full) is calculated, it is possible to obtain for the first mode shape:

$$R = \frac{\|\psi_{1,ex}\|}{\|\psi_1\|} = 3.464 = \sqrt{N} \tag{4.53}$$

that represents the classical relationship between the two modes. The same value is found for the second mode shape. The value of $\sqrt{N}$ is obtained due to the mass-normalization of the modes. In fact, the modes of the full system and those of the reduced system are mass-normalized; however, the first are normalized considering the mass of the full system, while the second are normalized considering the mass of the sector. Consequently, the expanded modes consider N times the mass of the sector and $\sqrt{N}$ is the factor to mass-normalize these modes.

The reduced aerodynamic matrix $[am_{CS}]$ can be directly obtained in this form without any reduction; in fact, for the single sector it is possible to write:

$$\left[am_{mod,CS}\right] = \begin{bmatrix} -2m_1\omega_1^2(\eta_{aer,1} + i\zeta_{aer,1}) & 0 \\ 0 & -2m_2\omega_2^2(\eta_{aer,2} + i\zeta_{aer,2}) \end{bmatrix} \tag{4.54}$$

where $\left[am_{mod,CS}\right]$ is the reduced modal aerodynamic matrix. The equation (4.37) is still valid, but the modal base used is that obtained in cyclic symmetry, i.e.:

$$[am_{CS}] = inv[\Psi_{CS}^H] * [am_{mod}] * inv[\Psi_{CS}] \tag{4.55}$$

Since the flutter analysis is performed in this thesis in the frequency domain, the HBM is applied to the equation of motion (4.51) that becomes:

$$\left(-(h\omega)^2[m_{CS}] + ih\omega\left([c_{CS}] + \left[c_{aer,CS}\right]\right) + [k_{CS}] + \left[k_{aer,CS}\right]\right)\bar{x}_{CS}^{(h)} = f_{nl,CS}^{(h)}, \quad h = 1, \dots, H \tag{4.56}$$

The equation of energy balance (4.42) is still used together the equation (4.56) to get a well-conditioned problem. The energy equations are those of the full bladed disk, but they are expressed in the cyclic symmetry form, i.e.:

$$E_{aer} = \pi * imag\left((\bar{x}_{CS}^{(1)})^H * [am_{CS}] * \bar{x}_{CS}^{(1)}\right) \tag{4.57}$$

$$E_{diss,str} = \pi * imag\left((\bar{x}_{CS}^{(1)})^H * i\omega[C] * \bar{x}_{CS}^{(1)}\right) \tag{4.58}$$

$$E_{diss,cont} = \pi|\bar{u}^{(1)}|imag(f_{nl,CS}^{(1)}) \tag{5.59}$$

where $\bar{u}^{(1)}$ is the 1st order complex relative tangential displacement of the contact element ($\bar{u}^{(1)} = \bar{\mathrm{x}}_{\mathrm{b}}{}^{(1)} - \bar{\mathrm{x}}_{\mathrm{d}}{}^{(1)}$).

## 4.4.1 Result analysis

The initialization of the flutter analysis has made through the calculation of two initial tentative points that represent the equilibrium points of the energy balance. Since the first mode of the reduced system is considered unstable, the main energetic contribution at flutter will be given by this mode therefore the energy balance will be performed varying the first modal coordinate amplitude $\bar{q}_{CS}^{(1)}$ that multiplies the first unstable mode $\psi_{1,CS}$ in according with the equation (4.45).

To compare the results of the reduced system with those of the full system, the flutter analysis has been performed with the same parameters. Figure 4.40 shows the flutter analysis of the reduced system where the blue 'o' marker is the LCO solution, while the red 'x' marker is the stability limit solution. The solution obtained is coherent with the other types of analyses performed before, in fact the stable solution presents LCO a big frequency and a small amplitude of vibration; while, the unstable solution has a small frequency and a big vibration amplitude.

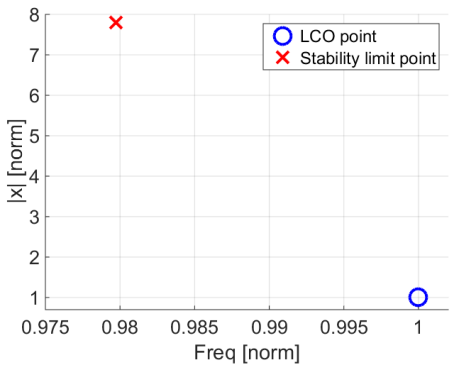


Figure 4.40: Flutter response of a bladed disk in cyclic symmetry

The stability of two solutions is check in Figure 4.41a for the LCO response and Figure 4.41b for the stability limit.

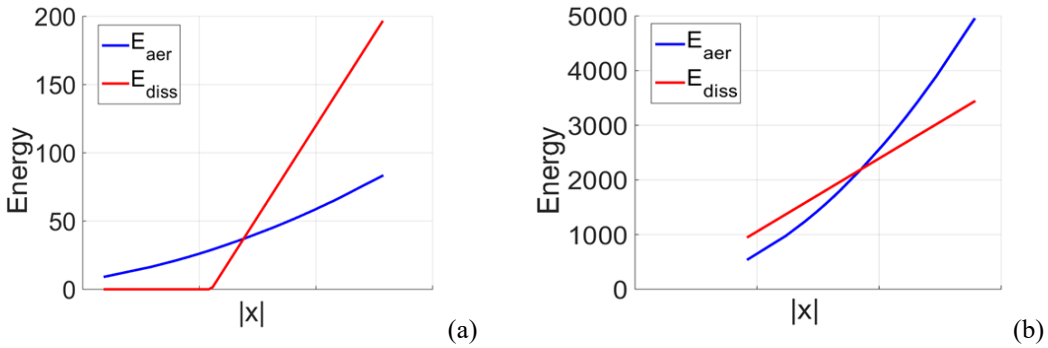


Figure 4.41: Stability analysis of LCO solution (a) and stability limit (b)

The obtained results in Figure 4.40 are now compared with the results calculated in Figure 4.25 in terms of frequency and amplitude of vibration. This comparison is made in Figure 4.42 where it is possible to see a good match between the flutter results of the reduced system (‘o’ marker) and those of the full system (‘x’ marker). The figure shows a small difference in the stability limit point due to the numerical errors occurring in the calculation. In this case the saved computation time is so small that no difference is highlighted because the system is very simple; however, it is sufficient to increase the number of sectors from 12 to real number of sectors of a bladed disk to see a great saving of computation time (table 4.8). In general, the velocity of the non-linear calculation depends on the number of non-linear degrees of freedom because the Newton-Raphson method needs

more iteration to find the displacements that give a residual equal to zero. This saving of time becomes important when only a sector of bladed disk is simulated because there is a great reduction of number of non-linear dofs to calculate (non-linear dofs of sector and not of the whole structure).

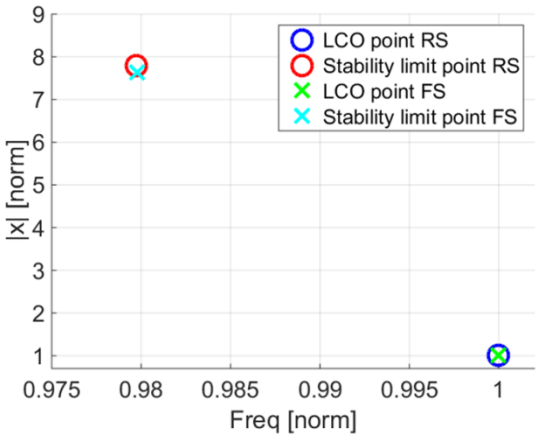


Figure 4.42: Comparison between the flutter results of the reduced system (RS) and those of the full system (FS)

| | Time [sec] |
|---|---|
| Full | 1 |
| Cyclic symmetry | 150 |

Table 4.8: Computation time of a bladed disk with 112 blades

The obtained results in the frequency domain with the reduced system will be compared with the results calculated with the DTI of the equation (4.51). Figure 4.43 and 4.44 respectively show the time response that reach the limit cycle oscillations and the uncontrolled response of the system. These responses have been obtained with two different boundary conditions, in according with the energy balance.

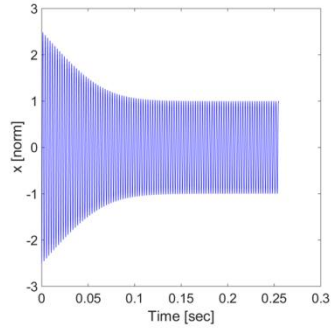


Figure 4.43: Stable time response of a bladed disk

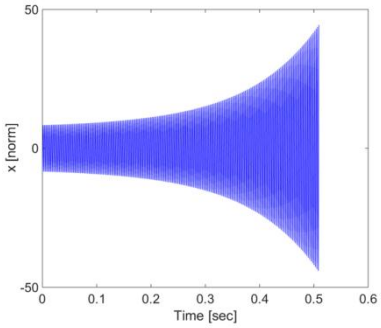


Figure 4.44: Unstable time response of a bladed disk

At last, the comparison of the LCO solution is made in the table 4.9 in terms of percentage error in amplitude and in frequency. It is possible to see that the both the errors are very small, i.e. the solution of equation of motion in frequency domain produces accurate results.

| | |
|---|---|
| Error in Amplitude [%] | 0.1 |
| Error in Frequency [%] | 0.001 |

Table 4.9: Percentage error between frequency domain and time domain

## 4.5 Conclusion

In this chapter the study of the flutter behavior for different lumped parameter models has been analyzed. From the discussion of the results obtained by Griffin and Sinha which have been replicated in the first section, the author has developed a methodology to study the flutter phenomena on different systems. For all systems taken into account the aero-damping parameter has been fixed a priori and interpreted as a viscous negative damping. Besides, the external force due to the engine order excitation have not been considered, i.e. only the self-excited vibration have been studied. This allowed to use a one-way method based on the resolution of the equation of motion in the frequency domain together with the energy balance to have a well-conditioned problem. The aerodynamic is therefore included in the equation of motion.

The three analyzed systems have the same dynamic behavior (the first mode, that is considered unstable, has the same mode shape) and the results show similar trend that are in accordance with those of Griffin and Sinha. In particular, the

flutter analysis presents two solutions, one stable at low amplitude and bigger frequency, and one unstable at big amplitude and lower frequency. The Parameter variation shows that the behavior of the contact has a great influence on the final result because of the quantity of dissipative energy that can balance the aerodynamic energy.

The method developed can be easily extended to a real model of a blade or a bladed disk because the definition of the aerodynamic matrix that contains the aero-damping and aero-stiffness coefficients depends on the dynamic behavior of the system in terms of modal analysis. This feature will be addressed in the next chapter.

# Chapter 5

# Flutter analysis of a bladed disk

In this chapter, the flutter analyses will be performed on a FE model of a bladed disk developed by GE Avio Aero inside the regional project Great-2020 phase 2 promoted by Piedmont region. The method proposed for lumped parameter models is extended to analyze a real sector of a bladed disk and the same parameters, used in the Chapter 4, have applied in the sensitivity analyses to see if their effects on a bladed disk are similar in terms of typical trends.

Two different approaches have been developed:

- a physical approach;
- a modal approach.

The first approach is based on the reduced matrices of mass and stiffness obtained by a CMS-CB reduction; while in the second approach a modal reduction is performed. For the physical approach, before to analyze the bladed disk, the blade-alone configuration will be studied to understand the effect of the flutter phenomenon on no cyclic symmetry structures.

## 5.1 Model and case study

The analyzed FE model of a bladed disk is that of the regional project Great-2020. The sector is illustrated in Figure 5.1 and it is composed of six components: the blade, the bar, the disk, the cone-shaft and two retainer rings. From this point to the end of the thesis, the assembly blade and bar will be generally called blade,

while the assembly disk, cone-shaft and retainer rings will be generally called disk. The studied bladed disk is characterized by a dove-tail attachment that will have an important role in the flutter analysis. In fact the system will be studied in tip free condition, i.e. the only source of damping, beyond the mechanical damping of the material, will be produced at root joint through the application of contact elements.

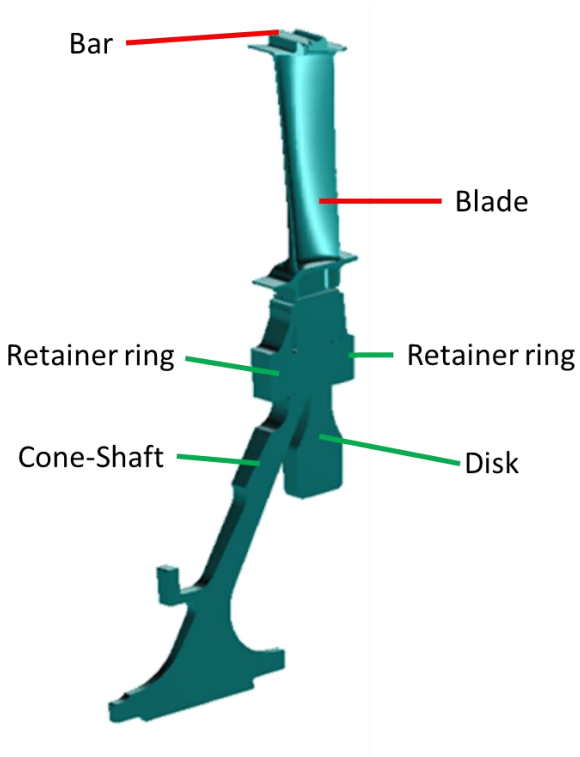


Figure 5.1: CAD model of Great-2020 bladed disk

The dynamic behavior of the bladed disk is reported in the ZZENF diagram (Zig-zag shaped excitations in nodal diameters versus frequency) in Figure 5.2 where the trends of the first three modal families by varying the nodal diameters are shown. It is possible to see that these three modes are well separated and reach a constant value of natural frequency for high values of ND. The mode shapes of these three modes are plotted in Figure 5.3a, 5.3b and 5.3c. They are respectively classified as the first flap mode, the first edge wise mode and the first torsional mode.

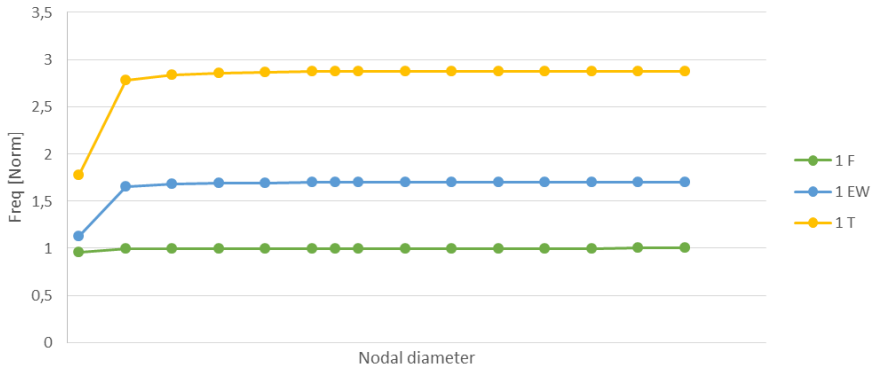


Figure 5.2: ZZENF diagram of the bladed disk

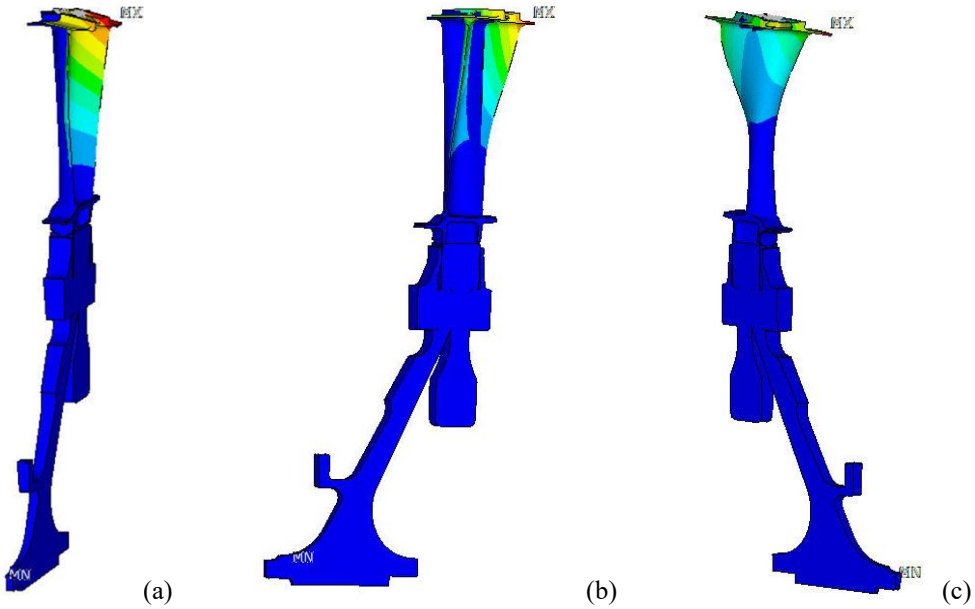


(a) (b) (c)

Figure 5.3: mode shapes of the first three modes – (a) flap mode; (b) edge wise mode and (c) torsional mode

These modes have been analyzed at flutter using the aerodynamic code LARS developed by the Department of Industrial Engineering of University of Florence [30] that is used by GE Avio Aero. The aerodynamic flutter analysis shows that only the first flap mode is unstable at flutter while the other modes are stable. The trends of the aero-damping ($\zeta_{aer}$) and aero-stiffness ($\eta_{aer}$) coefficients are reported

in Figure 5.4. The aero-damping shows a minimum negative value for positive values of ND. This value can be considered the worst condition because the aerodynamic energy introduced in the system is maximum, i.e. it represents the most unstable condition of the bladed disk. For this reason, the bladed disk will be analyzed at flutter taken into account the value of ND that gives the minimum value of aero-damping.

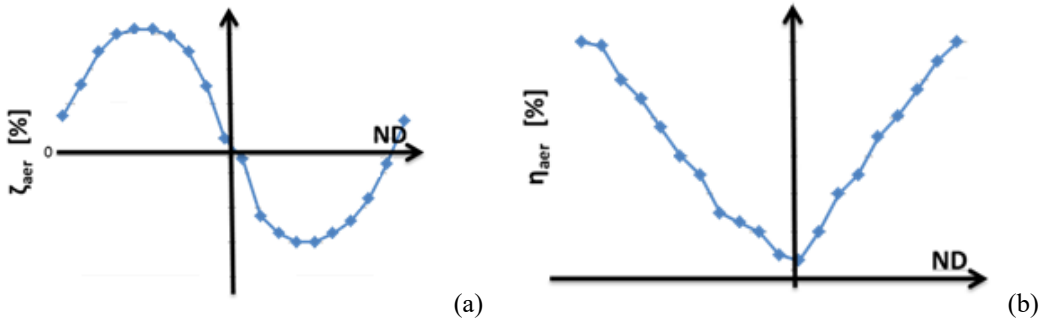


Figure 5.4: aero-damping (a) and aero-stiffness (b) parameters at variation of ND

Fig 5.5 shows the aero-damping density on the airfoil for the value of ND that gives the minimum value of aero-damping. It is possible to see that the blade has a distribution of aero-damping that is stable in the tip and in the middle of the suction side, while the pressure side is overall unstable with a pick in the root of the airfoil.

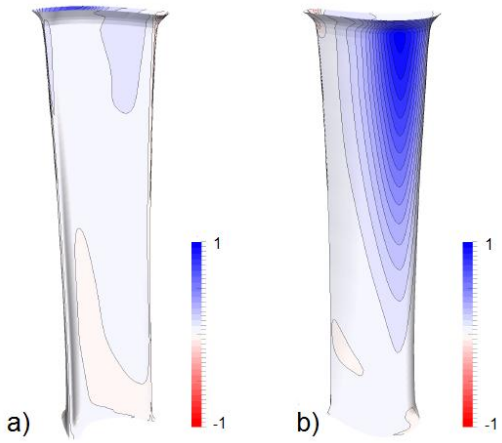


Fig 5.5: aero-damping density for the value of ND with the minimum value of aero-damping – a) pressure side, b) suction side (the scale is normalized)

## 5.2 Contact stiffnesses determination at the blade root joint

To perform the aero-elastic analysis, the bladed disk sector will be modeled as two distinct FE models with Ansys software where the blade is initially unconstrained. The connection between the blade and the disk is done in the root joint that is characterized by a dove tail attachment. In particular, the attachment will be made by node-to-node contact elements that are characterized by contact stiffnesses.

The values of the contact stiffnesses used in the contact model are calculated according to the utilization of contact wizard tool in Ansys software. In detail, a subpart of the blade root and disk slot was selected (Figure 5.6) and modeled at FEM (Figure 5.7). The elements CONTA174 and TARGE170 are applied on the contact surfaces and solved with a pure Lagrange method that allows to analyze the state of the contact without the utilization of the contact stiffnesses. To realize this calculation a fine mesh on the contact surfaces should be defined. Also proper constraints should be applied on the selected subpart of the root joint to guarantee a right behavior of the model and to keep in contact the two contact surface during the calculation. In particular on the left and right surfaces the tangential displacements are prevented to simulate the remaining part of the bladed disk, while in the bottom surface the three degrees of freedom are unable to simulated the rigid constraint of the shaft. Instead, on the top surface, a finite displacement $\delta$ is applied to allow a controlled displacement of the contact surfaces.

The utilization of the lagrangian method has been also chosen for the geometry of the contact. In fact, the common methods in literature (for example the [74]) calculate the contact stiffnesses through a separation of the normal and tangential problems. However, the geometry of the root joint does not allow to divide the influence of the normal displacement from the influence of the tangential displacement due to the slope angle of the contact (Fig. 5.8).

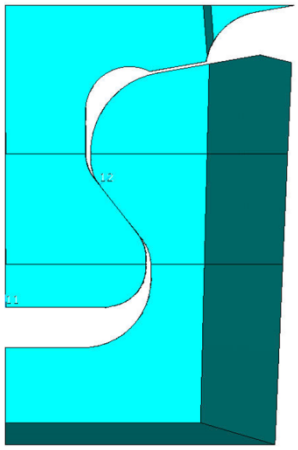

Figure 5.6: selection of the subpart of the root joint for the contact stiffnesses calculation

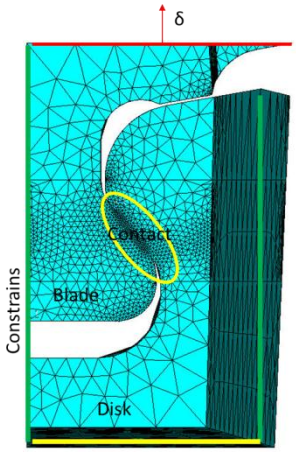


Figure 5.7: FE model of the subpart of the root joint for the contact stiffnesses calculation with definition of the constrains (green line tangential displacement unable; yellow line 3 dofs unable) and the finite displacement δ (red line) applied

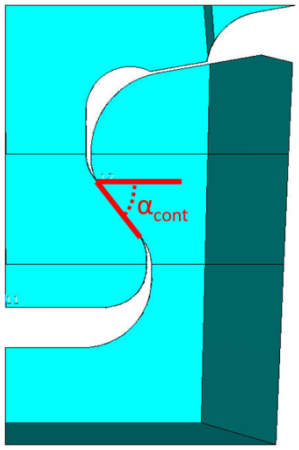


Figure 5.8: blade root geometry

A small value of δ displacement is applied and a non-linear static analysis is performed. The results obtained in terms of state of the contact and pressure distribution are presented respectively in Figure 5.9 and 5.10. It is possible to see that the contact is always in the slip state, while the pressure has a right distribution; in fact along the principal direct of slipping the pressure is concentrated at the borders of the contact surface. Since the contact is in the slip state, the tangential contact stiffness in this state has a value minor than the value that it would have in stick condition. For this reason, different calculations with a smaller value of displacement δ has been performed. However, the state of the contact is always slip. This happens due to the geometry of the contact that has an angle $\alpha_{cont}$ of inclination of the contact surface bigger than 45 degree (see Fig. 5.8 for definition of $\alpha_{cont}$). In fact, if a linear behavior is supposed, it is possible to write:

$$\frac{\delta_T}{\delta_N} = \frac{F_T}{F_N} = \tan \alpha_{cont} \tag{5.1}$$

where $\delta_T$ and $\delta_N$ are the decomposition of displacement δ in the tangential and normal directions, while $F_T$ and $F_N$ are the tangential and normal contact forces. Besides, the state of the contact is characterized by the slip condition that involves the following relationship:

$$\frac{F_T}{F_N} = \mu \tag{5.2}$$

If the results of the equations (5.1) and (5.2) are compared, the tangent of $\alpha_{cont}$ will be always bigger than friction coefficient μ and consequently the state of the contact can be only in the slip condition.

Figure 5.9: contact state

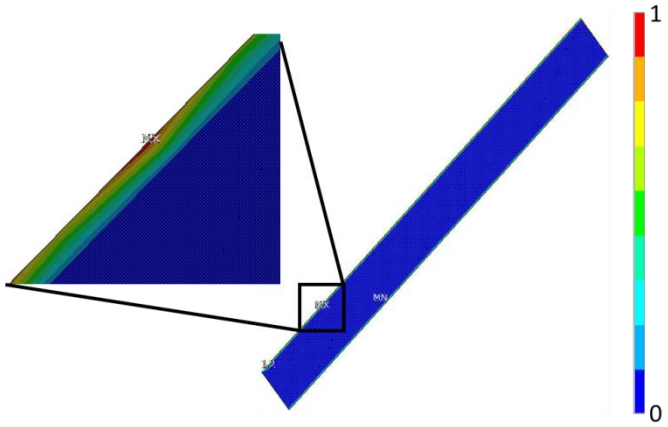


Figure 5.10: pressure distribution on the contact surface

To calculate the real value of tangential contact stiffness, two ways are possible: chose a non-physical value of friction coefficient $\mu$ bigger than $tan(\alpha_{cont})$ or start from the deformation solution with the contact in slip condition and suppose an unload of the contact. Both case has been analyzed and the stick condition has been reached. In the first case the ratio $F_T/F_N$ will be always minor than friction coefficient (however this is not representative of a physical behavior); while in the second case an unload of the contact from the slip condition can only produce a

stick behavior (see in Figure 5.11 the red circle on a hysteresis loop of contact model where the unload of the contact from slip state occurs).

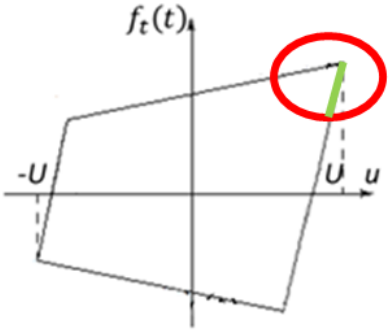


Figure 5.11: hysteresis loop of contact model

The second case has been chosen for the calculation of contact stiffnesses because it is physically correct. Figure 5.12 shows the contact is in stick condition, while the distribution of pressure is shown in Figure 5.13. More interesting is to see the color map of normal (Figure 5.14) and tangential (Figure 5.15) displacements around the contact surface. In fact, from these two figures, it is possible to see how the contact, beyond a normal displacement that is near constant, presents also a rotation. This behavior is highlighted in Figure 5.15 where it is shown a non-constant distribution of tangential displacements.

The contact stiffnesses can now be calculated as gradient of the unload curve (green line in Figure 5.9) by the following equations:

$$K_n = \frac{\Delta F_z}{\Delta z} = \frac{F_{z,slip} - F_{z,stick}}{z_{slip} - z_{stick}}$$
$$K_t = \frac{\Delta F_x}{\Delta x} = \frac{F_{x,slip} - F_{x,stick}}{x_{slip} - x_{stick}} \tag{5.3}$$

where the forces and the displacements are the differences between their values in slip state and their values in stick state. The values of $F_z$ and $F_x$ are identified as total reaction forces on the contact surfaces in the local reference system of the contact, while the displacements are obtained as difference of the mean value of displacements of the elements in the two yellow boxes shown in Figure 5.15:

$$
\begin{aligned}
z_{slip} &= z_{slip,1} - z_{slip,2} \\
z_{stick} &= z_{stick,1} - z_{stick,2} \\
x_{slip} &= x_{slip,1} - x_{slip,2} \\
x_{stick} &= x_{stick,1} - x_{stick,2}
\end{aligned}
\tag{5.4}
$$

These boxes have been chosen because they are placed in two areas away from the contact where the local deformations of this can be neglected. However, the selection of these areas have been made arbitrarily and consequently they are subject a certain level of uncertainty.

Figure 5.12: contact state

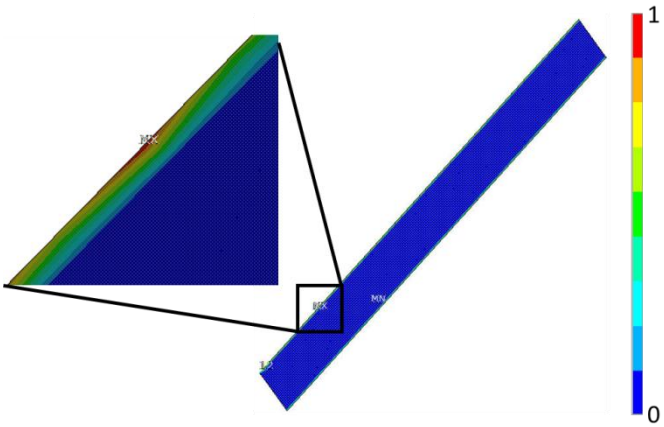


Figure 5.13: pressure distribution on the contact surface

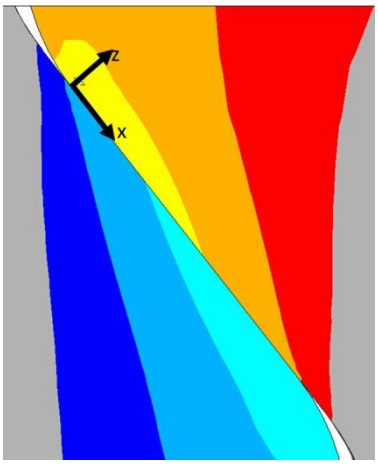


Figure 5.14: normal displacement near the contact surface

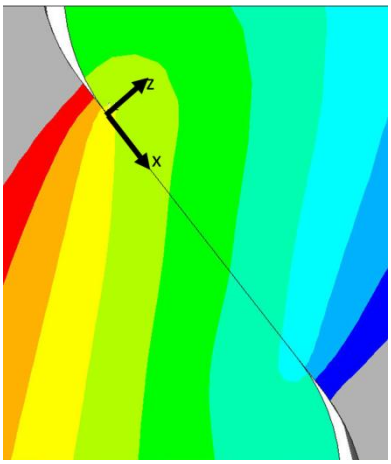


Figure 5.15: tangential displacement near the contact surface

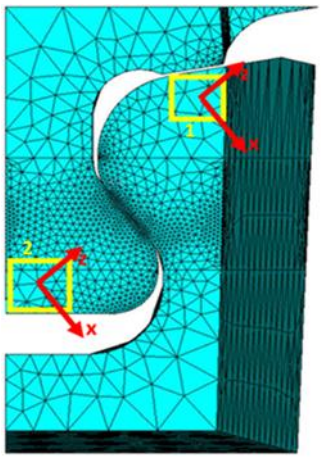


Figure 5.16: areas for the definition of displacements to use in the calculation of 'delta' displacements

## 5.3 Physical Approach

The physical approach for the calculation of the LCO response is based on the ROM of the mass and stiffness matrices of the bladed disk. This approach works with the physical coordinates of the system and the results are the frequency and the amplitude of flutter vibrations.

The physical approach is applied to two configurations:

- the blade-alone;
- the bladed disk.

In the first case of study, only the blade is analyzed and as a consequence the cyclic symmetry is not considered, while in the second case the blade-disk assembly is analyzed with the cyclic symmetry hypothesis.

### 5.3.1 Blade-alone

The first case analyzed is that of the blade-alone. In this configuration the disk is considered infinitely stiff, i.e. the cyclic symmetry is not considered. This hypothesis can be considered valid because the minimum (negative) value of aero-damping that represents the worst condition at flutter (instability) is associated to a high value of nodal diameter (see Figure 5.17) where the mode shape is blade dominated.

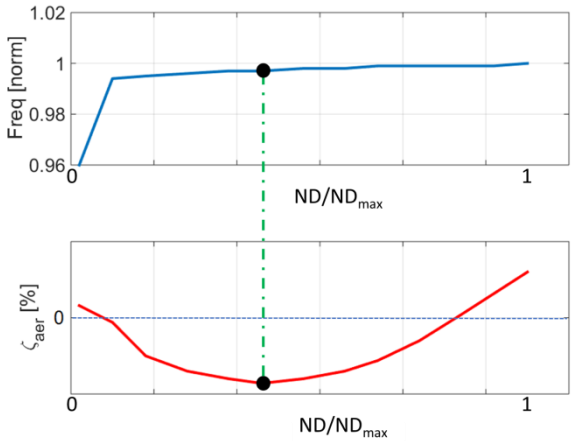


Figure 5.17: natural frequencies of the first modal family associated to the aero-damping by varying the ND.

To validate the hypothesis of an infinitely stiff disk, it is important to verify the difference of the natural frequencies and mode shapes between the blade-alone configuration and the bladed disk. This is made in the Figure 5.18 and 5.20, where the eigenvalues and the *MAC* between the two configurations are respectively shown. The MAC number is the Modal Assurance Criteria and it is defined as:

$$MAC = \frac{|\{\psi_{OB}\}^T * \{\psi_{BD}\}|^2}{(\{\psi_{OB}\}^T * \{\psi_{OB}\})(\{\psi_{BD}\}^T * \{\psi_{BD}\})} \tag{5.5}$$

where $\psi_{OB}$ and $\psi_{BD}$ are respectively the mode shapes of the blade-alone configuration and the bladed disk. The *MAC* is a parameter that indicates how much two modes are similar each other, i.e. the *MAC* number compares the shape and not the absolute value of the deformed shape. It can assume a value between 0 and 1, where 0 indicates that the two modes are completely different while 1 is the opposite, i.e. the two mode shapes are the same.

Figure 5.18 compares the natural frequencies of the blade-alone and bladed disk. It is possible to note that the frequencies of the blade-alone configuration are bigger than the natural frequencies of those of the bladed disk (the mass of the blade-alone is lower than the mass of the bladed disk because there is not the disk, and the structure is more rigid due to the lack of a flexible disk) with an error smaller than 5% for the most part of the modes. The exceptions are found for the modes eight, twelve and fifteen (see Figure 5.19). These errors are acceptable because the natural frequencies of these modes are away by the flutter conditions (only the first mode is unstable).

In Figure 5.20 the *MAC* number for the first 15 modes (direct comparison – 1$^{st}$ vs. 1$^{st}$, 2$^{nd}$ vs. 2$^{nd}$, etc.) is reported and shows that the most part of the modes have a MAC bigger than 0.9, i.e. they are very similar each other. However, it is possible to note that there exist modes with a MAC number smaller than 0.9; these modes are the eighth and the eleventh, they have a MAC number around 0.85, and the modes fourteen and fifteen have a value of MAC near to zero, i.e. these two modes in the two configurations are different. Since these modes are modes at high frequencies, they do not influence the dynamic behavior of the blade in the flutter condition because this phenomenon is dominated, in this case of study, by modes at low frequencies.

Figure 5.21a and 5.21b show the MAC of all combinations of the 15 modes and not only the direct comparison. From the figure 5.21a it is possible to note that the modes 14 and 15 of the blade-alone configuration are more similar respectively at modes 13 and 14 of the bladed disk instead of the equivalent modes, while it is not possible to say anything about the mode 15 of the bladed disk because the mode 16 of the blade alone was not calculated.

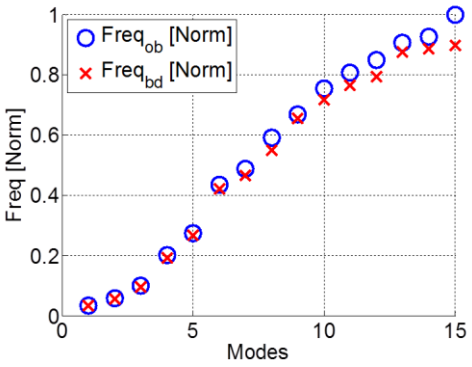


Figure 5.18: comparison of natural frequencies between blade-alone and bladed disk

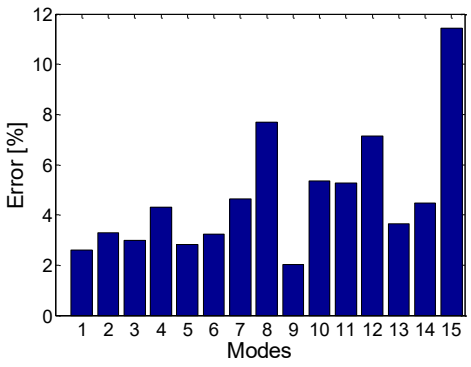


Figure 5.19: error of natural frequencies between blade-alone and bladed disk

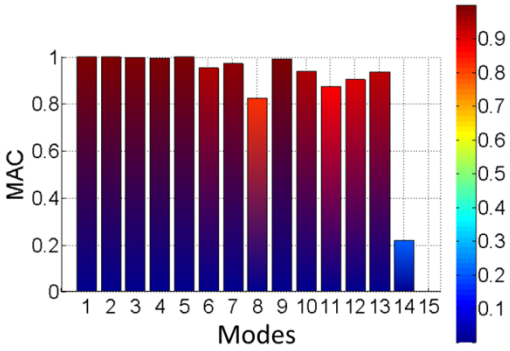


Figure 5.20: Direct MAC number between the modes of blade-alone and bladed disk

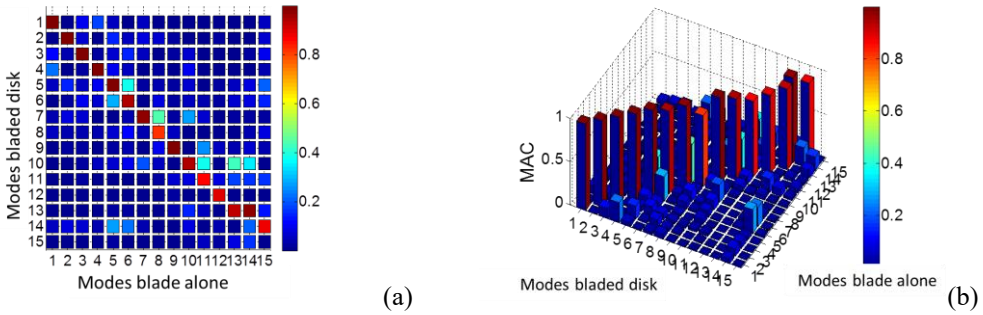


(a) (b)

Figure 5.21: MAC number of the all combination of modes between blade-alone and bladed disk

The calculation of the eigenvalues and eigenvectors was performed with the blade root joint fixed; for the blade-alone configuration this means that the nodes on the contact surfaces have been constrained in the three dofs while for the bladed disk the matching nodes on the contact surfaces of the blade and disk have been merged together. In this condition the blade root joint cannot produce dissipative energy because the relative displacements at the contact do not exist and as a consequence the LCO calculation is impossible. To allow the LCO calculation the blade root joint may be able to slip but also to simulate the stick condition. This can be modeled using the contact elements that link the blade with the ground in the case of the blade-alone configuration (see Figure 5.22). To model a 3D contact, two orthogonal 2D contact elements with the same value of normal contact stiffness, normal displacement and normal pre-load are used. In this case, the relative displacement of the slider of the contact is equal to the absolute displacement, i.e.

$$u = x_b - x_g = x_b \tag{5.6}$$

where $u$ is the relative displacement and $x_b$ is the displacement of the contact nodes of the blade.

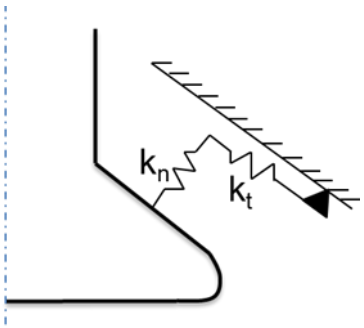


Figure 5.22: contact element for the blade-alone root joint

Since the value of the stiffnesses is limited and chosen equal to the values calculated in the section 5.2, the comparison of the dynamic behavior between a blade with fixed contact and the same blade with the contact elements should be similar but not equal. The differences in term of natural frequencies and mode shapes are reported in Figure 5.23 and 5.25. Figure 5.23 shows the trend of the natural frequencies of the system in the two conditions (fixed contact and contact elements). It is possible to see that the model with the contact elements has

smaller frequencies for every mode and this is correct because the contact is less stiff due to a finite value of the contact stiffnesses. In general, the error between the two configurations is smaller than 3.5% (Figure 5.22). Instead, Figure 5.25 shows the direct MAC number (1st vs. 1st, 2nd vs. 2nd, etc.) between the first 15 mode shapes of the blade in the two conditions and it is possible to note that for all the modes the value of the MAC is near to 1, i.e. the modes are very similar.

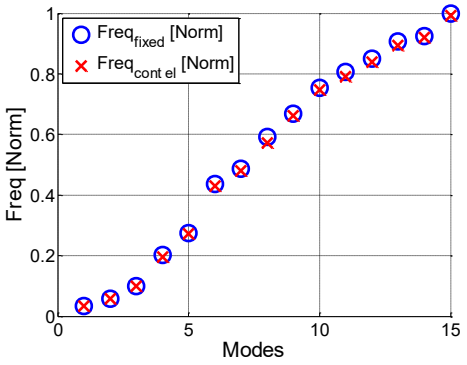


Figure 5.23: comparison of the natural frequencies for the blade-alone between fixed contact and contact elements

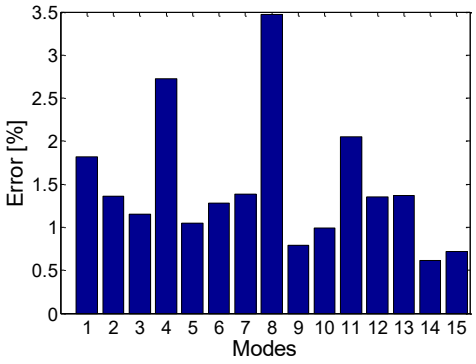


Figure 5.24: error of the natural frequencies of for the blade-alone between fixed contact and contact elements

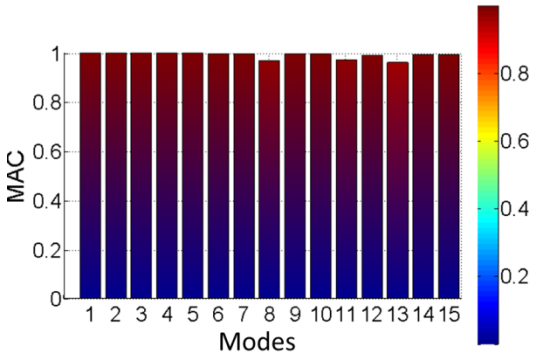


Figure 5.25: direct MAC number between the modes of the blade-alone case with fixed contact and contact elements

After checking the hypothesis of the disk infinitely stiff, the FE model of the Great-2020 blade has been reduced with the CMS-CB technique to have an acceptable number of dofs and usable from a normal personal computer. The master nodes considered for the reduction are:

- all the nodes in the contact surfaces of the blade root joint;
- 15 accessory nodes that describe the airfoil motion;

The slave modes taken into account are 30. The reduction was performed with the body in free condition, i.e. no constrains are included because the contact elements will be simulated in MatLab. However, the effect of the centrifugal force was taken into account to have a better approximation of the physical behavior of the system in the real working condition.

The reduced mass and stiffness matrices have been imported in MatLab where the contact elements have been added in stick condition to evaluate the approximation errors due to the reduction. Figures 5.26, 5.27 and 5.28 show respectively the comparison of the natural frequencies, the errors of the natural frequencies and the MAC between the modes of the whole system and those of the reduced system. It is possible to note from Figure 5.26 and 5.27 that the natural frequencies of the reduced system are equal to those of the full system (the errors are smaller than 1%), while from the Figure 5.28 the MAC shows that the modes are the same. The errors in Figure 5.27 are negative because the frequencies of reduced system are slightly larger than the frequencies of the full system and this is due to the fact that a reduction techniques generally produces a stiffer system.

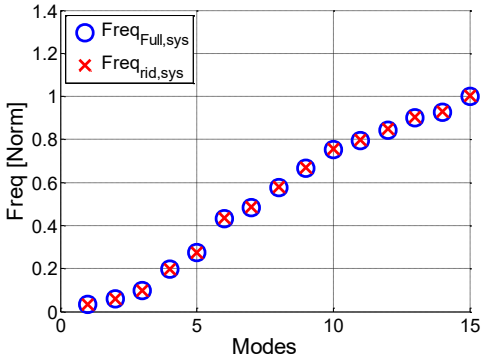


Figure 5.26: comparison of the natural frequencies of the blade-alone between full and reduced systems

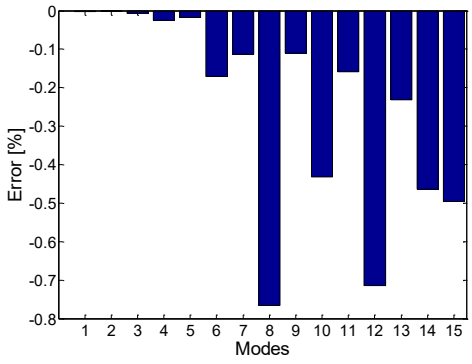


Figure 5.27: error of the natural frequencies of the blade-alone between full and reduced systems

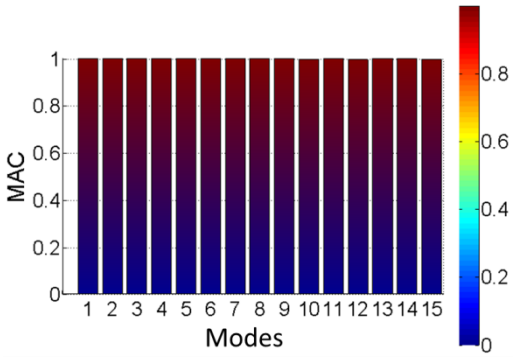


Figure 5.28: direct MAC number between the modes of blade-alone of the full and reduced systems

The reduced mass and stiffness matrices that are used to build the damping matrix $[C]$ and linearized aerodynamic matrix $[AM]$ on the base of the equations (4.27) and (4.37) of the previous chapter, where modal ratios $\zeta_m$, $\zeta_{aer}$ and $\eta_{aer}$ have been used to assembly the modal matrices. The used eigenvectors $[\Psi]$ are those of the system with the contact in the stick condition because these are very close to the dynamic behavior of the blade under the flutter condition. From the linearized aerodynamic matrix $[AM]$ it is possible to derive the aero-damping and aero-stiffness matrices ($[C_{aer}]$ and $[K_{aer}]$) from equations (4.33). The equations of motion in the frequency domain to solve is:

$$(-(h\omega)^2[M] + ih\omega([C] + [C_{aer}]) + [K] + [K_{aer}])\bar{x}^{(h)} = F_{nl}^{(h)}, \quad h = 1, \dots, H \tag{5.7}$$

As for the lumped parameter models, the frequency of the flutter vibration of the system is unknown, therefore the energy balance equation (4.17) must be taken into account together with the equations of motion to have a well-conditioned problem. Equations (4.41), (4.43) and (4.44) are used for the energy balance, where the parameter $N_c$ in the equation (4.44) is the total number of contact elements that is equal to twice the contact nodes (every contact node is characterized by two 2D contact elements).

Since the reduced matrices $[M]$ and $[K]$ describe a free system (no constraints applied during the reduction), to facilitate the convergence of the calculation a proper tentative solution is defined through the energy balance between the dissipative and the aerodynamic energy. This calculation is based on the mode

shape of the unstable mode, that in this case of study is the first flap mode, by varying a complex modal coordinate (see equation (4.45)). The intersection of the two energies give the tentative solution that will be near to the solution.

#### *5.3.1.1 Parameter variation*

The ROM of the blade is used to compute the LCO points together with the linearized aerodynamic matrix, similarly to what has been done for the lumped parameter models. A Parameter variation is performed to see if the different parameters in the non-linear flutter analysis influence the flutter response of the system similarly to the lumped parameter models.

These parameters are:

- aero-damping ($\zeta_{aero}$);
- aero-stiffness ($\eta_{aero}$);
- friction coefficient ($\mu$);
- normal pre-load ($n_0$);

where the aero-stiffness coefficient is now considered.

Since the root joint has a slope angle, the distribution of the normal pre-load on the contact surfaces is not uniform, but depends on the boundary conditions. However, to simplify the Parameter variation in this case and the future case of study with the bladed disk, a uniform distribution of normal pre-load was initially considered. To obtain this distribution, the blade is considered rigid and an equilibrium equation along the radial and circumferential directions is analytically solved in order to find the global left and right normal pre-loads that act on the contact nodes according to eq. (5.8):

$$n_0 = \frac{F_C}{2(\cos(\alpha_{cont})+\mu sin(\alpha_{cont}))N_{cont}} \tag{5.8}$$

where $\alpha_{cont}$ is the slope of the contact surface, $N_{cont}$ is the number of contact element and $F_c$ is the centrifugal force. In Figure 5.29 the simplified distribution is shown where z is the axial direction parallel to the length of one contact and y is the direction parallel to the width of the contact for one root side (see Figure 5.30). In this calculation the tangential global contact loads $T$ acting on the two sides are assumed to be proportional to the normal load by means of the Coulomb's limit $T=\mu N$.

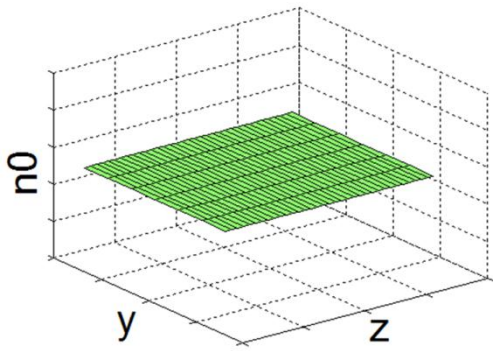


Figure 5.29: uniform distribution of the normal pre-load $n_0$

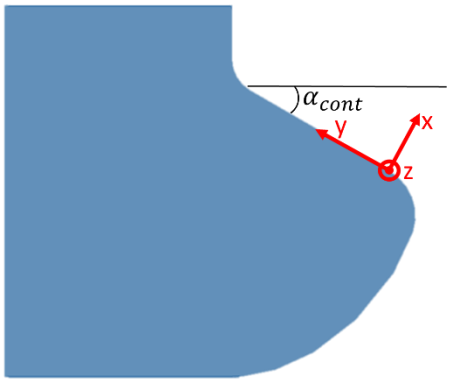


Figure 5.30: blade root geometry

The LCO is calculated by varying the value of the negative aero-damping coefficient and the friction coefficient. In the next figures the friction coefficients are indicated with the nomenclature $\mu_1$ (nominal value), $\mu_2 = 2.5\mu_1$ and $\mu_3 = 3.5\mu_1$, while the aero-damping coefficient is indicated with $\zeta_1$, $\zeta_2$ and $\zeta_3$ ($\zeta_1$ will be considered the nominal value, $\zeta_2$=1.36 $\zeta_1$ and $\zeta_3$=1.6 $\zeta_1$). It must be noted that the normal pre-load depends on the friction coefficient according to the equation (5.8). As a consequence, the normal preload decreases if the friction coefficient increases. The general tendency of a contact to slip or stick can be represented by the Coulomb's limit that defines the transition between the stick and the slip state. Since the Coulomb's limit $C_{lim}$ is equal to the normal pre-load multiplied by the friction coefficient, it can be noted that the Coulomb's limit increases as the friction coefficient increases; in fact, by manipulating equation (5.8), it can be obtained:

$$C_{lim} = \frac{\mu F_c}{2\cos(\alpha_{cont})} \tag{5.9}$$

LCO results are shown in Figure 5.31. It is possible to see that, for a given value of the friction coefficient, the amplitude of the LCO calculated at the tip of the blade increases when the absolute value of the negative aero-damping increases (see for example the three grouped markers). On the contrary, the LCO frequency decreases. These results are consistent with expectations since the more the energy introduced by flutter on the blade, the higher the vibration amplitude to dissipate an equivalent amount of energy by friction to achieve the LCO equilibrium. At the same time, the LCO frequency decreases since the blade root

joint is less rigid when the amount of slip increases. If the value of the friction coefficient increases for a given value of the aero-damping coefficient (see for example the blue markers), the LCO amplitude increases while the LCO frequency remains near constant. Even in this case results are consistent with expectations since the higher the friction coefficient, the higher the amplitude to let the contact slip in order to dissipate the same amount of energy required for the LCO.

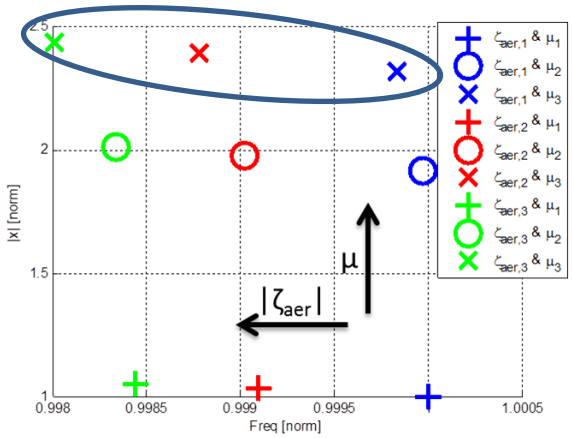


Figure 5.31: LCO amplitude by varying the aero-damping coefficient and the friction coefficient

The results plotted in Figure 5.31 show the response of the system in terms of frequency and amplitude, but they do not give information about the deformation of the blade. This information can be obtained comparing the real deformation of the blade in flutter condition with the modes of the system using the MAC number. For all the points of Figure 5.31 the MAC number between the real deformation and modes of the blade are equal to zero with exception of the first value that is equal to 0.99, i.e. the predominant mode is only the unstable mode. This equality can be better seen in Figure 5.32 where the the first mode shape (left) and the flutter deformed shape (right) are reported.


Figure 5.32: deformation of the blade: a) mode shape, b) flutter deformation

A better detailed trend of the LCO is shown in Figure 5.33 where both amplitude (above) and frequency (below) are plotted with respect to the aero-damping coefficient. In particular, the amplitude of the response goes to zero by gradually reducing the aero-damping until it is equal to the structural damping: in this case the only solution possible is the trivial solution because the energy introduced by flutter is always balanced by the dissipative energy of the material, i.e. the system is always stable. On the contrary, the LCO can be found for a maximum value of the aero-damping coefficient after which the blade response is always unstable. This result agrees with the results obtained by Griffin in [58] for one dof dynamic system and in general with the results obtained in Chapter 4.

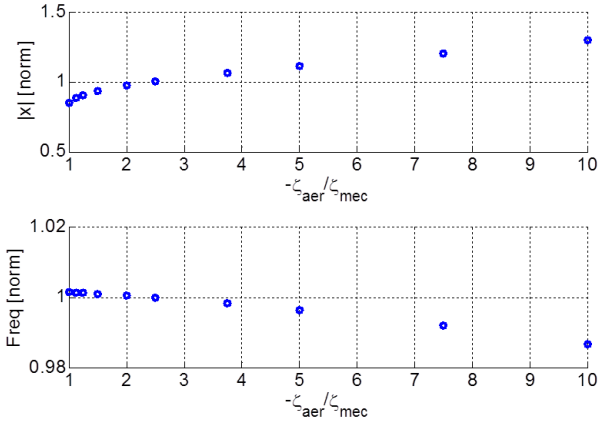


Figure 5.33: LCO amplitude and frequency by varying the aero-damping parameter

The value of the normal pre-load depends on the centrifugal force. It is possible to see a linear relationship between the LCO amplitude (upper figure) and the normal preload, while the corresponding frequencies (lower figure) remain constant by varying $n_0$ (Figure 5.34). This result is in accordance with the results presented by Petrov in [60] and with the results obtained in the previous chapter. Finally, Figure 5.35 shows the LCO amplitude when the value of the aero-stiffness is varied of the same amount as the aero-damping coefficient. It is possible to see that the effect of the aero-stiffness acts only on the frequency of the response and not on the amplitude; in particular, the LCO frequency increases as expected if the aero-stiffness value increases. This happens because the aero-stiffness is a parameter that quantifies the additional stiffness due to the aerodynamic flow. This effect can be seen mathematically observing the modal aero-stiffness matrix of equation (4.39); in fact, the general component of the matrix is:

$$\left[k_{aer,mod\ (i,i)}\right] = 2m_i\omega_i^2\eta_{aer,i} \quad with\ i = 1, \dots, N \tag{5.10}$$

where $m_i$ is the modal mass, $\omega_i^2$ is the square of the natural angular frequency and $N$ is the total number of dofs. Since the modal mass is usually equal to 1 and $\eta_{aer,i}$ is a critical modal ratio always positive, it is easy to see that the system has an increase of the natural frequencies equal to the equation (5.10). In fact, by considering only the modal stiffness matrices of equation of motion it is possible to see that:

$$\left[k_{mod\ (i,i)}\right] + \left[k_{aer,mod\ (i,i)}\right] = \omega_i^2(1 + 2\eta_{aer,i}) \quad with\ i = 1, \dots, N \tag{5.11}$$

However, observing the values in Figure 5.35, the frequency variation is less than 1% and it can be still considered negligible; for this reason, the aero-stiffness parameter is generally not considered as important as the aero-damping coefficient for the determination of the LCO.

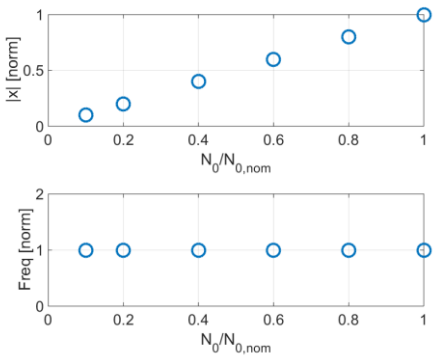


Figure 5.34: linear relationship between the Limit Cycle amplitude and frequency, and the normal pre-load

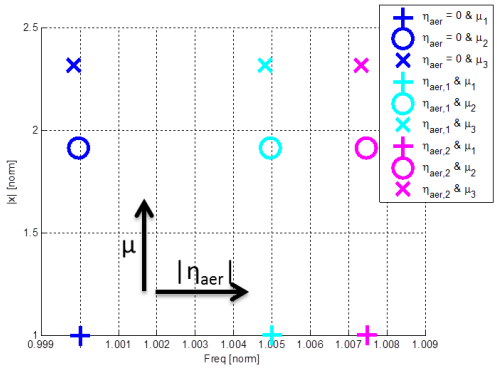


Figure 5.35: LCO response by varying the aero-stiffness parameter for three different friction coefficients.

### *5.3.1.2 Comparison with DTI*

The direct time integration (DTI) is the best effective method to solve the non-linear equation of motion because it gives the right solution of the problem, but it involves a very long calculation time. For this reason, the presented frequency method has been developed. However, to understand if the frequency method is effective to calculate the right LCO of the system, it has been compared with DTI.

The model used in this section slightly differs from the one used for the Parameter variation. In particular, a simplified model of the blade was considered to reduce the computation time and improve the stability of the time integration. This model has eight contact points, four on the left and four on the right contact surfaces instead of using all the nodes on the two surfaces.

Since the model is changed, a calculation in the frequency domain is first performed to see if the flutter behavior of the blade has a different trend. It is possible to see from Figure 5.36 that the trend of the flutter response of the simplified system is similar to the trend shown in Figure 5.31 where the "full" reduced system has been analyzed. From the different combinations of aero-damping and friction coefficient, the parameters of the central point (red 'o' marker) has been chosen and a time integration of the equation of motion was performed.

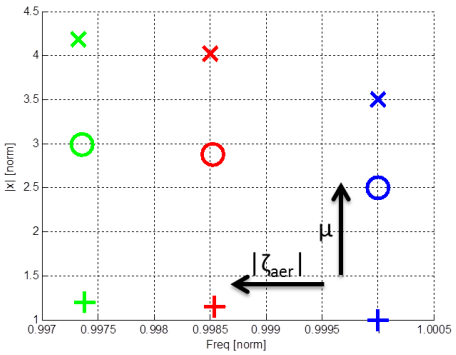


Figure 5.36: LCO flutter response of the simplified system in the frequency domain

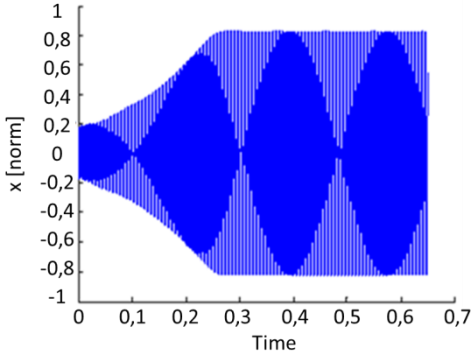


Figure 5.37: flutter response of the simplified system in the time domain

Figure 5.37 shows the result of the DTI of the equation of motion in the presence of contact elements and negative aero-damping. It is possible to see that, after a transient period, the response of the system becomes periodic with a constant amplitude. This state describes the LCO. These responses in the time domain have been used to compare the results obtained in the frequency domain and so to evaluate the effectiveness of the frequency based method. Table 5.1 shows the percentage errors in amplitude and in frequency between time and frequency responses for a given set of aero-damping and friction coefficients. The frequency response was obtained considering only the first harmonic of the Fourier series and it is possible to note a good match between the frequency values of the two responses, but a significant error in amplitude (10%). It is important to note the difference between the comparison 'frequency vs. time' methods made for the lumped parameter models and for the blade-alone case, in fact in the first case the error can be considered equal to zero, while now it cannot be considered negligible as well. This effect is mainly due to the complexity of the blade-alone model compared to the lumped parameter models, and in particular the complexity of the contact region.

| | |
|---|---|
| Error in amplitude | 10.2% |
| Error in frequency | 0.8% |

Table 5.1: Comparison time vs. frequency (1st harmonic)

The comparison between the frequency and the time responses shown above has been made by considering only the first term of the Fourier series (1st harmonic) and not the higher terms. If these terms are considered in the solution of the flutter equations (equation of motions plus energy balance) in the frequency domain, the flutter response will change. The results are reported in Figure 5.38, where it is possible to note that the increase of the number of the harmonics (the hth term of truncation of the Fourier series) produces a reduction of the LCO amplitude, while the frequency remains near constant. The reduction of the LCO amplitude produces a reduction of the error in amplitude until a value of error of 4% (see table 5.2) that can be considered acceptable. Instead the error in frequency remains constant. The introduction of n-harmonic produces a reduction of LCO amplitude because the aerodynamic forces are always introduced to the first order while the friction forces have the Fourier coefficients different from zero as many as the considered harmonics. Consequently there is not a balance of forces between the harmonic indices of the friction forces and the harmonic of the aerodynamic forces and this produces a reduction of amplitude (the system is more damped).

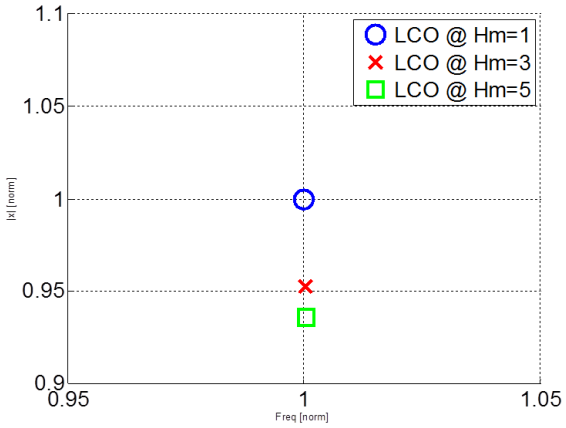


Figure 5.38: LCO flutter response of the simplified system in frequency domain considering 1, 3 and 5 harmonic

| | |
|---|---|
| Error in amplitude @ Hm=1 | 10.2% |
| Error in frequency @ Hm=1 | 0.8% |
| Error in amplitude @ Hm=3 | 5.8% |
| Error in frequency @ Hm=3 | 0.9% |
| Error in amplitude @ Hm=5 | 4.1% |
| Error in frequency @ Hm=5 | 0.9% |

Table 5.2: 'time vs. frequency' methods comparison by varying the number of harmonics retained in the MHBM calculations

The two approaches, in frequency and in time, have naturally a great difference in the calculation time. Table 5.3 shows the values of the calculation times where it is significant to see that the increase of the number of the harmonics used in the solution of the equation in the frequency domain produces an increase of the computation time, but this value remains smaller than the time requested by the DTI.

| Domain | Time |
|---|---|
| Frequency @ Hm=1 | ≈ 5 min |
| Frequency @ Hm=3 | ≈ 40 min |
| Frequency @ Hm=5 | ≈ 2 h |
| DTI | ≈ 120 h |

Table 5.3: Computation time in the frequency and time domain

### 5.3.2 Bladed disk

The analyses on the blade-alone configuration are the first step to analyze a real model of a bladed disk. However, this configuration is useful to understand the flutter behavior of systems not in cyclic symmetry or the blades in a cascade (for example to make comparison with experimental results of a cascade rig).

To simulate the real dynamic behavior at flutter of a rotor sector, a bladed disk is analyzed. Only a sector of the bladed disk is taken into account and analyzed in cyclic symmetry because the system is considered tuned, i.e. all sectors are equal to each other. A strong coupling between the sectors is assumed since geometric non-linearities that may break the cyclic symmetry behavior are not considered. This assumption is coherent with the calculation of the aero-dynamic coefficients that is based on a periodic self-excited force depending on cyclic symmetry conditions.

As made for the blade-alone configuration, the analyzed bladed disk has to have a blade root joint able to slip and not fixed. In this case, a root joint fixed means that a node on the contact surface of the blade must move in the same way and of the same quantity of the correspondent node on the contact surface of the disk, while the slip condition is allowed by the contact elements. The contact element used (see Figure 5.39) is the same of the blade-alone configuration, but now the contact displacements are relative and equal to:

$$u = x_b - x_d \tag{5.12}$$

where $x_b$ and $x_d$ are respectively the displacements of the contact nodes of the blade and disk.

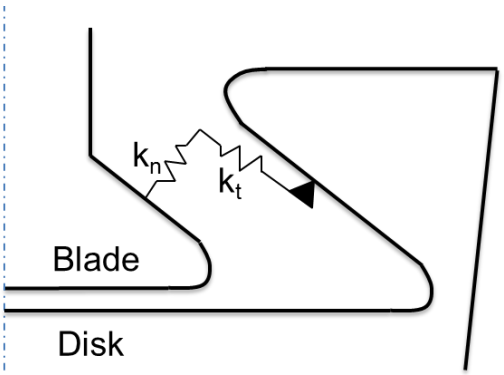

Figure 5.39: contact element between the blade and the disk

Since the contact element is characterized by contact stiffnesses with a finite value, the dynamic behavior of the system in the two configurations, merged contact and contact elements, will be similar but not equal. For this reason, how made for the blade-alone, a comparison of the dynamic behavior of the bladed disk in the two configurations of joint is performed form Figure 5.40 to Figure 5.42.

Figure 5.40 shows the trend of the natural frequencies of the system in the two conditions (fixed contact and contact elements); it is possible to see that the match of the frequency is good with a maximum error of 4.2%. However, at difference of the blade-alone where all the natural frequencies of the system with the contact elements were smaller than the frequencies with the root joint fixed, here only the modes at low frequency with the contact elements have lower frequencies, while for the modes at high frequency it is contrary (see Figure 5.41). This result is also highlighted in Figure 5.42 where the comparison of the mode shapes is presented with the MAC number. It is possible to see that the first nine modes are the same, while there is some difference from the tenth mode (the MAC number is around 0.8). Since these modes are modes at high frequency, their influence on the dynamic behavior in the flutter condition will be small because the studied flutter phenomenon is dominated by modes at low frequency.

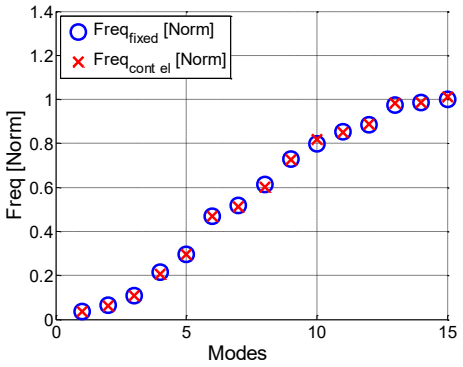


Figure 5.40: comparison of natural frequencies of bladed disk with fixed contact and contact elements

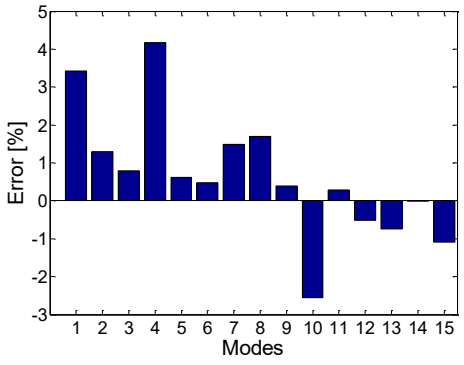


Figure 5.41: error of natural frequencies of bladed disk with fixed contact and contact elements

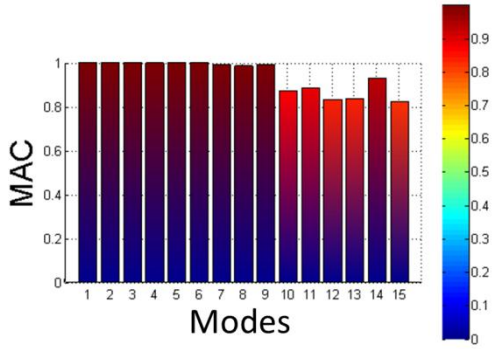


Figure 5.42: direct MAC number between the modes of bladed disk with fixed contact and contact elements

Since the dynamic behavior of the bladed disk in the two conditions of joint is similar and can be considered acceptable for the study of the flutter response, the ROM techniques have been applied to the FE model of the bladed disk. The bladed disk has been reduced dividing the blade from the disk.

The blade has been reduced with the CMS-CB technique in the same way made for the blade-alone configuration, while the disk has been reduced with the CMS-CB technique using the software Ansys and then the cyclic symmetry and Tran reduction have been applied to further reduced mass and stiffness matrices.

The master nodes considered for the reduction of the disk are:

- all nodes on the contact surfaces of the blade root joint;
- all nodes on the interface surfaces;

while the mode slave taken into account are 30. The reduction was performed considering the effect of the centrifugal force to have a better approximation of the physical behavior of the system. After the CMS-CB reduction, the dofs of the interface have been further reduced with the application the cyclic symmetry and Tran reduction, where the modes of interface taken into account are 40.

The reduced mass and stiffness matrices of the blade and disk have read in MatLab where the contact elements have been added in stick condition to evaluate the approximation errors due to the reduction. Figures from 5.43 to 5.45 show respectively the comparison of natural frequencies, the error of the natural frequencies and the MAC between the modes of the whole system and those of

the reduced system. It is possible to note from Figure 5.43 and 5.44 that the natural frequencies of the reduced system are slightly bigger than those of the full system (the errors are negative and minor of 1%). The negative error is due to the stiffening effect of the reduction. Figure 5.45 shows the MAC of the mode shapes. The values reported in the figure are equal to 1, i.e. the reduced modes describe well the dynamic behavior of the full system.

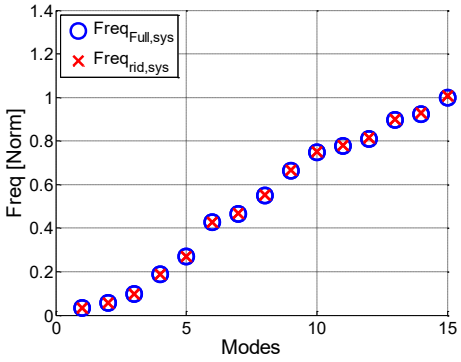


Figure 5.43: comparison of the natural frequencies of bladed disk of full and reduced systems

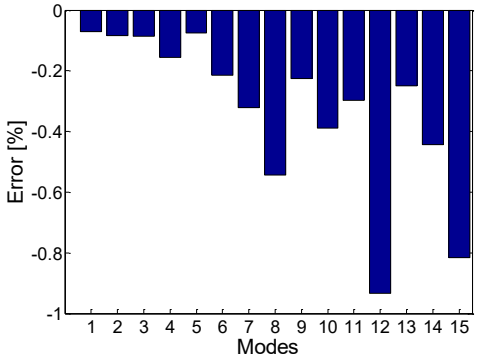


Figure 5.44: error of the natural frequencies of bladed disk of full and reduced systems

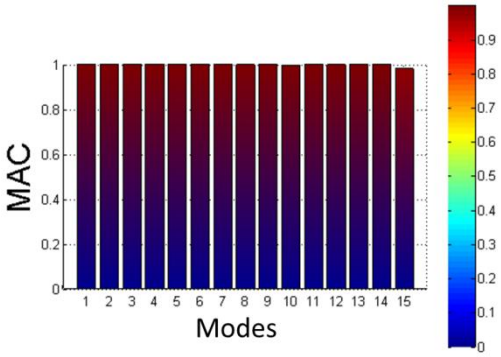


Figure 5.45: direct MAC number between the modes of full and reduced system

Blade and disk have been reduced separately for reasons of convenience. In fact in this way, the stiffness matrices of the two bodies remain fixed, but it is possible to build different stiffness matrices of bladed disk changing the values of contact stiffnesses. The other possibility was to reduce the full system with the root joint

modeled through springs which values of stiffness are equal to the contact stiffnesses. However, in this way two problems arise, the first is that if the contact stiffnesses change, a new reduction will be needed; the second is that the root joint is in stick condition and the method developed for flutter calculation can have problem to convergence. A variation of the method proposed to solve this last problem will be shown in the modal approach.

The reduced mass and stiffness matrices have used to build the damping matrix $[C]$ and the linearized aerodynamic matrix $[AM]$ on the base respectively of the equations (4.27) and (4.37) of the previous chapter. The used eigenvectors $[\Psi]$ are those of the system with the contact in the stick condition because these represent the dynamic behavior of the blade in flutter condition, but the stiffness matrix $[K]$ used in the equation of motion (5.7) is that without the contact, i.e. it has the following form:

$$[K] = \begin{bmatrix} k_{disk} & 0 \\ 0 & k_{blade} \end{bmatrix} \tag{5.13}$$

This form of the stiffness matrix has been chosen because the connection between the blade and the disk is made by the contact elements during the calculation of the vector of the non-linear forces. Since blade and disk are separated, to increase the velocity and the stability of the calculation a proper tentative point is defined through the energy balance between the dissipative and the aerodynamic energy as done for the blade-alone analyses.

#### *5.3.2.1 Parameter variation*

The ROM of the bladed disk is used to perform a parameter variation of the flutter response. The parameters that influence the non-linear flutter analysis are:

- aero-damping ($\zeta_{aero}$);
- friction coefficient ($\mu$);
- contact stiffness ($k_t$);

As made for the flutter analyses of the blade-alone configuration, an uniform distribution of the normal pre-load is considered to perform a LCO calculation. The first two parameters analyzed are the negative aero-damping and the friction coefficients.

Figure 5.46 plots the results considering the combination of friction and aero-damping coefficients (the nomenclature used is the same of the case of study with the blade-alone). It is possible to see that, for a given value of friction coefficient, the amplitude of the LCO increases, while the frequency decreases, when the absolute value of the negative aero-damping increases. Also an increase of the friction coefficient produced an increase of amplitude while the LCO frequency decreases for a fixed value of aero-damping coefficient (the blue markers). These results can be considered consistent with expectation because the variation of the energy introduced by flutter on the blade produces the necessary vibration amplitude to dissipate an equivalent amount of energy by friction to achieve the LCO equilibrium. It must be noted that the variation of the LCO frequency by varying the friction coefficient is actually negligible since the highest variation with respect to the nominal point is less than 0.5%.

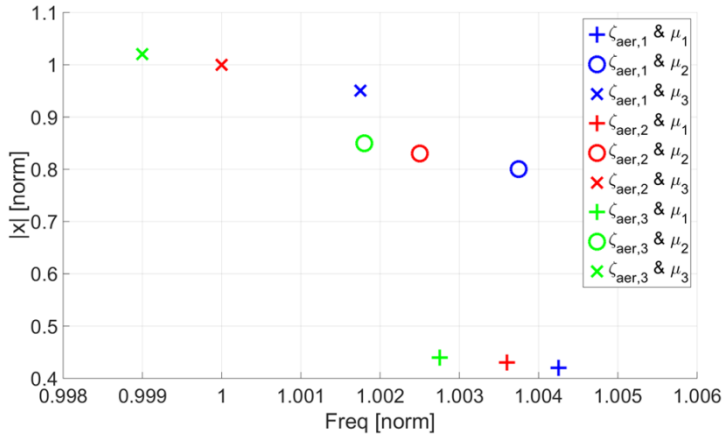


Figure 5.46: LCO amplitude by varying the aero-damping and the friction coefficients

Figure 5.47 compared the real deformation of the bladed disk in flutter condition with the first flap mode of the system. It is possible to note that the two deformations are equal and this is also highlighted by MAC number that has a value equal to 0.99, i.e. the predominant mode, as happens in the blade-alone configuration, is only the unstable mode.

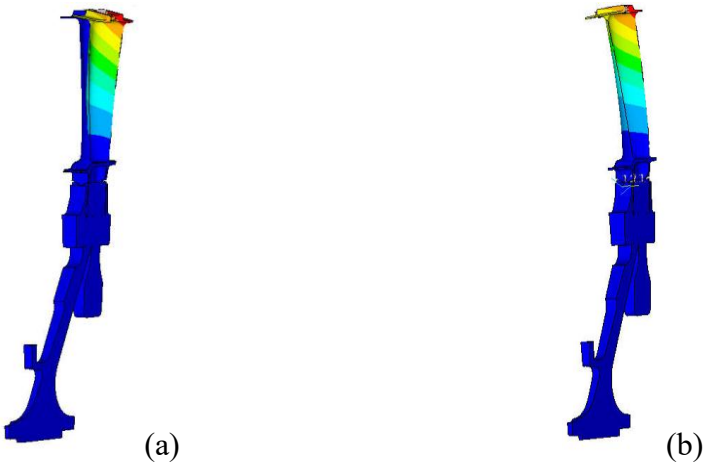


Figure 5.47: deformation of the bladed disk: a) mode shape, b) flutter deformation

Since the contact stiffnesses are parameters difficult to calculate, they are subjected to uncertainty. The used values have been obtained in Ansys software through the Lagrangian methods (see section 5.2) and they can be considered acceptable. However, it is important to evaluate the impact of the variation of the contact stiffnesses on the flutter response.

Since the two analyses performed to calculate the contact stiffnesses have shown the same value of the normal stiffness $k_n$, a Parameter variation was performed varying the value of tangential stiffness $k_t$. Three different values of tangential stiffness have considered: $k_{t,1}$ is the nominal value obtained in the final analysis of section 5.2, $k_{t,2}=k_{t,1}/2$ and $k_{t,3}=k_{t,1}/4$. Figure 5.48 shows that the variation of the tangential stiffness produces a reduction of the LCO frequency, while the amplitude has a slight increase that is minor than 0.5% and consequently can be neglected.

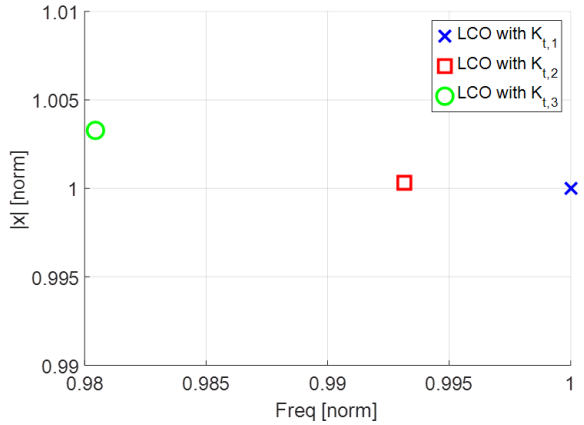


Figure 5.48: LCO calculation by varying the tangential contact stiffness

Figure 5.34 and 5.48 allow to identify other two parameters, beyond the aero-damping and the friction coefficients, that have a great influence on the amplitude and the frequency of the LCO points. In particular the value of normal pre-load acts on the amplitude, while the contact stiffnesses act on the frequency.

## 5.4 Modal Approach

The modal approach for the calculation of the LCO response is based on the modal reduction of the bladed disk. This approach works with the modal coordinates of the system and as a consequence the physical results of the system should be obtained through a modal transformation of equation (3.9).

The modal base $[\Psi]$ has been obtained from a modal analysis performed in Ansys where the effect of pre-stress due to the centrifugal force is considered. The modes have been then extracted from Ansys only on the more important nodes that are the contact nodes of the blade and disk and the 15 accessory nodes on the airfoil.

The equation of motion to solve in the frequency domain is:

$$\left(-(h\omega)^2[m_{mod}]^{(h)} + ih\omega\left([c_{mod}]^{(h)} + \left[c_{aer,mod}\right]^{(h)}\right) + [k_{mod}]^{(h)} + \left[k_{aer,mod}\right]^{(h)}\right)\bar{q}^{(h)} = f_{nl,mod}^{(h)} \tag{5.14}$$

where$[m_{mod}]^{(h)}$, $[c_{mod}]^{(h)}$ and $[k_{mod}]^{(h)}$ are given by equation (3.12), while $\left[c_{aer,mod}\right]^{(h)}$ and $\left[k_{aer,mod}\right]^{(h)}$ are given by equation (4.39).

The modal approach will be applied only to bladed disk. The solution of equation of motion (5.14) with the energy balance allows to calculate the flutter response. To realize this calculation, the non-linear contact forces should be calculated; however, the proposed contact model works only in physical coordinates and in the time domain while the equation are solved in modal coordinates and frequency domain. The change of domain is solved with the Alternate frequency-time method, while for the change of coordinates the equations (3.2) and (3.9) are respectively applied to the displacements and non-linear forces.

The flutter analyses can be now performed. However, no results or incorrect results are obtained. This happens because, at difference of the physical approach where the blade and the disk are modeled separately and the contact elements are used to calculate the non-linear forces and so connect the two components, in the modal approach the blade and the disk must be connected together to have the right modal base. In fact, if blade and disk are separated, the modal base will be not representative of the dynamic behavior of the bladed disk because rigid body motions of the blades are found. These modes do not allow to perform the flutter analysis even if the contact elements are added. The problem is in the definition of the modal matrices of aero-damping and aero-stiffness because the aerodynamic coefficients are calculated on the modes of the bladed disk. If these coefficients are not correct, the self-excited aerodynamic force will be not correct and consequently the LCO calculation will be not possible.

A solution of this problem could be to connect blade and disk in the FEM model through springs equal to the contact stiffnesses and then to extract the modal base. However, in this case the modal base describes the right dynamic behavior of the bladed disk, but the root joint is too rigid, i.e. it is not possible to produce the dissipative energy when the contact is simulate in Matlab environment. Besides, the contact elements are counted twice and this produce an over stiffening of the system. These problems in the physical approach do not appear because the aero-dynamic matrices can be built separately using the modal base of the bladed disk with the contact in stick condition, while the stiffness matrix (5.13) is used in the equation of motion. Finally, the connection is then performed by the vector of non-linear forces.

To solve these problems and allow to calculate the flutter response with the modal approach, the proposed method has been opportunely modified.

### 5.4.1 Application of the fictitious contact force

The applied modification to solve the flutter calculation in modal domain allows to delete the dependence of the contact stiffnesses from the stiffness matrix of the system. However, this variation can be applied both for forced and flutter responses as well as for the equations both in physical and modal domains.

The starting point is the equation of motion:

$$[M]\ddot{x} + [C]\dot{x} + [K_s]x = F_e + F_{nl} \tag{5.15}$$

where the stiffness matrix in stick condition $[K_s]$ is equal to:

$$[K_s] = [K_{bd}] + [K_c] \tag{5.16}$$

$[K_{bd}]$ and $[K_c]$ are respectively the stiffness matrices of the bladed disk and of the contact. If the equation (5.16) is substituted in the equation (5.15), the system will be over stiffened because the contact elements appear twice. To remove the dependence of $[K_c]$, a fictitious contact force $F_{fit}$ should be added to the equation (5.15) to balance the addition of the contact stiffnesses in the stiffness matrix. The equation (5.15) becomes the following:

$$[M]\ddot{x} + [C]\dot{x} + [K_s]x = F_e + F_{nl} - F_{fit} \tag{5.17}$$

The vector of the fictitious contact force $F_{fit}$ describes the reaction forces that are produced on the contact nodes when these are linked together by means of springs, i.e. the contact elements are in stick condition:

$$F_{fit} = -[K_c]x \tag{5.18}$$

If eq. (5.16) and (5.18) are put in the eq. (5.17), it is easy to demonstrate that the additional contact stiffness in $[K_S]$ is perfectly balanced by the fictitious contact force $F_{fit}$.

In similar way the addition of the fictitious contact force can be used in the modal domain. In fact, the eq. (5.17) can be modalized through the modal transformation (3.9) and pre-multiplying the equation of motion by the hermitian of modal base $[\Psi_s]$ with the contact in stick condition. The resulting equation is:

$$[m_{mod}]\ddot{q} + [c_{mod}]\dot{q} + [k_{mod,s}]q = f_{e,mod} + f_{nl,mod} - f_{fit,mod} \tag{5.19}$$

where the different components are:

$$\begin{aligned}
&[m_{mod}] = [I] \\
&[c_{mod}] = 2\zeta[\Omega_S] \\
&\left[k_{mod,s}\right] = [\Omega_s^2] \\
&f_{e,mod} = [\Psi_s]^H F_e \\
&f_{nl,mod} = [\Psi_s]^H F_{nl} \\
&f_{fit,mod} = [\Psi_s]^H F_{fit}
\end{aligned} \tag{5.20}$$

$[\Omega_S]$ and $[\Psi_s]$ are the results of the modal analysis in stick condition, i.e. where the stiffness matrix is equal to eq. (5.16).

This method with a fictitious contact force has been before applied to a lumped parameter model and then applied to a bladed disk with reduced mass and stiffness matrices in physical domain (see Appendices A and B) to study the effects of this method on the forced response and on the flutter response. Since the results on the lumped parameter model and on a bladed disk have shown a good approximation, the same method will be now applied to solve the equation of motions expressed in modal domain. Before, the forced response will be calculated and a comparison with the results obtained in physical domain will be done, then the flutter analyses will be performed.

Figure 5.49 shows the forced response of a bladed disk with the contact in stick condition. It is possible to note that the response obtained through an iterative Newton-Raphson calculation is equal to the linear response (solution of equation of motion without the non-linear term). This result is obtained because the vector

of non-linear force $f_{nl,mod}$ is equal to the vector of the fictitious contact force $f_{fit,mod}$. The comparison of forced responses in modal domain and in physical domain is made in Figure 5.50. The figure shows that the two responses are equal in terms of resonance amplitude and frequency.

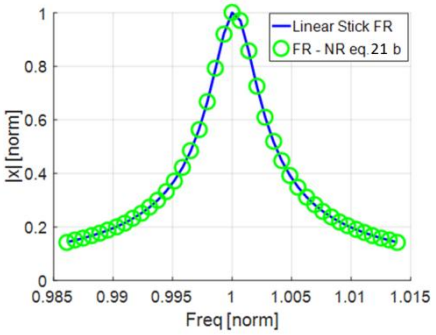


Figure 5.49: modal stick forced response

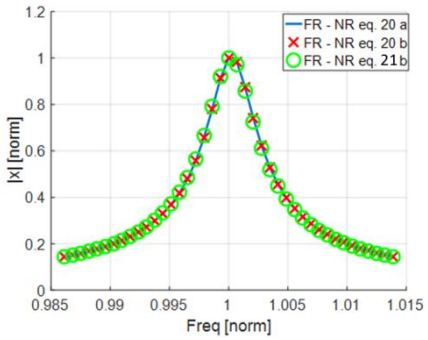


Figure 5.50: comparison between the stick forced responses in the physical domain and in the modal domain

More interesting is the damped forced response in modal domain and it comparison with the same response in physical domain. Figure 5.51 shows the modal damped forced response that can be considered correct because its resonance peak has a minor amplitude and frequency than the resonance peak in stick condition, i.e. the dynamic behavior of the bladed disk is rightly described. Instead, Figure 5.52 shows the comparison of the damped forced responses obtained in the two domains. It is possible to see that the damped forced response in modal domain goes towards the physical response with the increase of number of modes taken into account in the modal reduction. This behavior is correct because the accuracy of the modal response increases with the preserved number of modes in the reduction. Finally, Figure 5.53 shows the variation of damped forced response considering three different values of normal pre-load. Since the trend of resonance peak is correct at increase of normal pre-load (it goes towards the stick condition), the calculation of the forced response with fictitious contact force in modal domain can be considered correct.

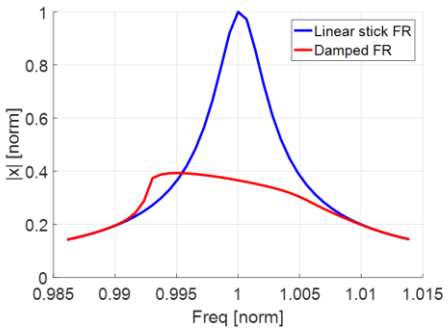


Figure 5.51: modal damped forced response

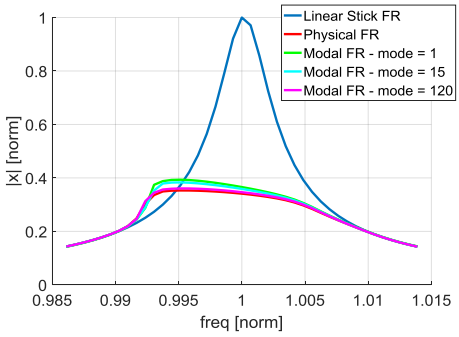


Figure 5.52: comparison between the damped forced responses in the physical domain and in the modal domain

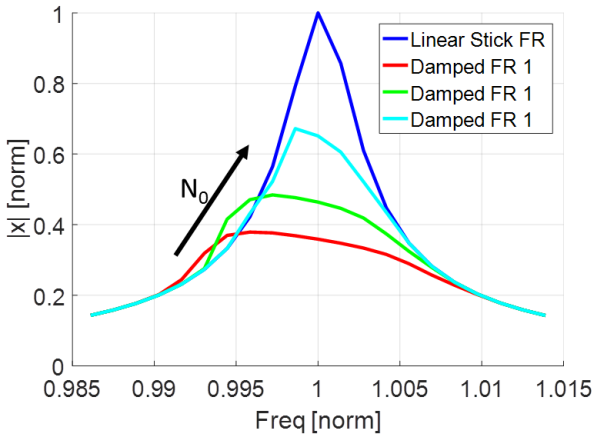


Figure 5.53: trend of the damped forced response

Since the method with a fictitious contact force works well for the calculation of forced responses, it will be now applied for the calculation of flutter response using the following equation:

$$\left(-(h\omega)^2[m_{mod}]^{(h)} + ih\omega\left([c_{mod}]^{(h)} + \left[c_{aer,mod}\right]^{(h)}\right) + [k_{mod}]^{(h)} + \left[k_{aer,mod}\right]^{(h)}\right)\bar{q}^{(h)} = f_{nl,mod}^{(h)} - f_{fit,mod} \tag{5.21}$$

The applied parameters are:

- contact stiffness $k_{t,1}$ and $k_n$ obtained from contact analysis and used in the previous analyses;
- friction contact $\mu_3$;
- aero-damping parameter $\zeta_{aero,2}$.

With these parameters and using the procedure applied in the previous analyses, the flutter analysis is performed. The first passage is a calculation of a starting tentative point to initialize the flutter calculation. However, Figure 5.54 shows that this initial tentative point does not exist; in fact, the aerodynamic energy is always bigger than the dissipative energy at variation of the first modal coordinate. To initialize the flutter calculation a tangential point between a parabola with origin in the axes and the curve of dissipative energy is searched (Figure 5.55). This point has been chosen because it represents the maximum amplitude whereby exists an equilibrium point.

From this initial point the flutter analysis is performed, but the solution obtained is the trivial one. This result can be foreseen because the value of aero-damping associate with the parabola ($\zeta_{aer,par}$) is minor in magnitude than the value of $\zeta_{aer,2}$. Besides, the dissipative energy that the system can produce is limited and linked to the relative displacement developed on the contact surface. However, at difference of the physical approach, the deformation of the bladed disk is closely linked to the mode shapes taken into account in the modal reduction and in particular to the first flap mode because this is the unstable mode at flutter. If modal displacements are not sufficient loose to produce the necessary dissipative energy to balance the aerodynamic energy, the LCO calculation is not possible even if the method with the fictitious contact force is applied.

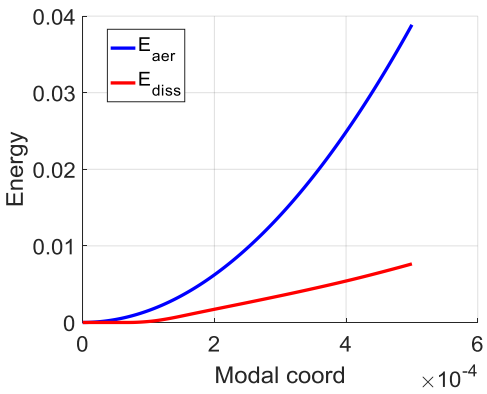


Figure 5.54: energy balance with $k_{t,1}$, $k_n$, $\mu_3$ and

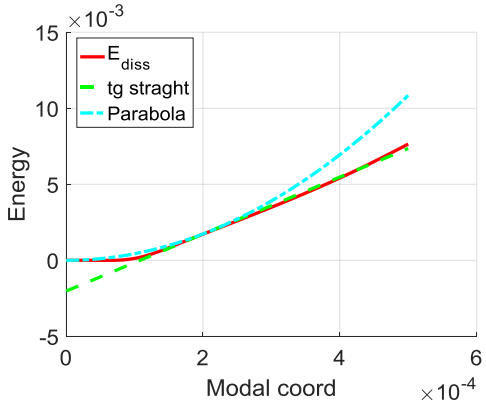


Figure 5.55: tangential point between a

| | |
|---|---|
| $\zeta_{aero,2}$ | parabola with origin in the axes and the curve of dissipative energy |

The LCO calculation is instead possible if the initial energy balance produces a starting tentative point because in this case the dissipative energy is sufficient to balance the aerodynamic energy and the flutter calculation can continue. Two examples are shown in Figure 5.56 and 5.57. Figure 5.56 shows the LCO response with the contact stiffnesses $k_{t,1}$ and $k_n$ at fixed value of aero-damping ($\zeta_{aero,4}=0.46\zeta_{aero,2}$) considering three values of friction coefficient ($\mu_1$, $\mu_2$ and $\mu_3$). Instead, Figure 5.57 shows the LCO response with the contact stiffnesses equal to $k_{t,3}$ and $k_n$, while the values of aero-damping and friction coefficients are those used in the past sensitivity analyses. Both figures show a correct trend at variation of aero-damping and friction coefficients and this happens because the initial tentative point is obtained.

A further check that the LCO response, obtained with the method with a fictitious contact force, is correct if an initial tentative point is predicted, is shown in Figure 5.58. This figure shows a comparison between the LCO point calculated with a physical approach and the LCO responses obtained with the modal approach by varying the number of mode preserved during the modal reduction. It is possible to see that increasing the number of modes in the modal base, the LCO response goes correctly towards the LCO point of physical approach (in the limit case of all modes preserved the two solutions should be equal).

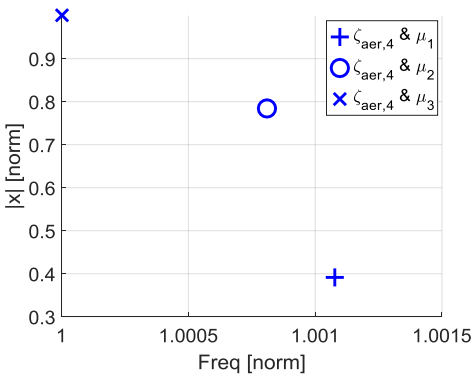


Figure 5.56: LCO points with $\zeta_{aero,4}=0.46\zeta_{aero,2}$ by varying the friction coefficient

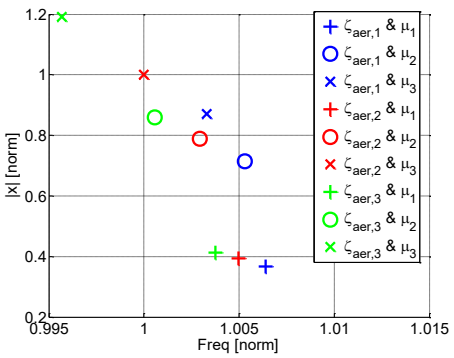


Figure 5.57: LCO points by varying the aero-damping and friction coefficients using the contact stiffnesses equal to $k_{t,3}$ and $k_n$

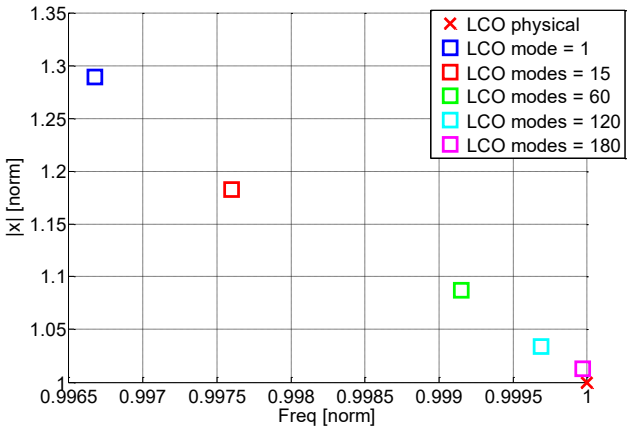


Figure 5.58: LCO points by varying the number of modes in the modal base using the contact stiffnesses equal to $k_{t,3}$ and $k_n$

This method with a fictitious contact force can be applied for the flutter analysis, however it has some limitation that are due to rigidity of the modes. In the past figure, two examples where this method works have been presented. However, for a right analysis of the bladed disk of G2020 project, the values of contact stiffness to use are those obtained from the analysis of the contact, but these do not give results if not the trivial solutions. To solve this problem a compromise is reached, a percentage of the contact stiffnesses is given to the springs that link together blade and disk in the FE model, while the total value of contact stiffnesses is given in the contact elements simulated in MatLab environment. Naturally, the same percentage of stiffness used to link the blade and the disk, it is also used to calculate the fictitious contact force.

This compromise can be considered acceptable because the dynamic behavior of bladed disk with a percentage of the contact stiffness is similar to the dynamic behavior of the bladed disk both with the fixed contact and with the total contact stiffness. These comparisons are made in Figure 5.59-5.61 for the bladed disk with the fixed contact and in Figure 5.62-5.64 for the bladed disk with contact stiffness. It is possible to note that the error in frequency increases if the values of contact stiffness decrease (see error in Figure 5.41 and 5.60); this happens because the blade root joint is less stiff. However, the mode shapes remain the same, especially for the modes at low frequency that are the more important in the flutter analyses because the unstable mode is the first. In particular, this mode has a MAC equal to 1 both in Figure 5.61 and 5.64, i.e. the flap mode shape is not changed.

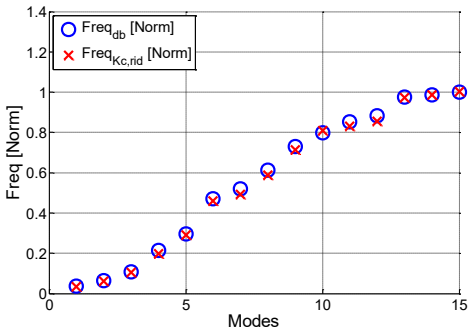


Figure 5.59: comparison of the frequency of the bladed disk with fixed contact and with a percentage of the contact stiffness

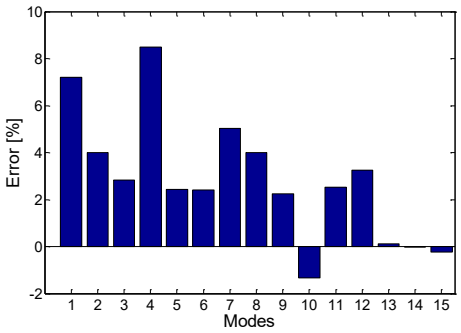


Figure 5.60: error in frequency of the bladed disk with the fixed contact and with a percentage of the contact stiffness

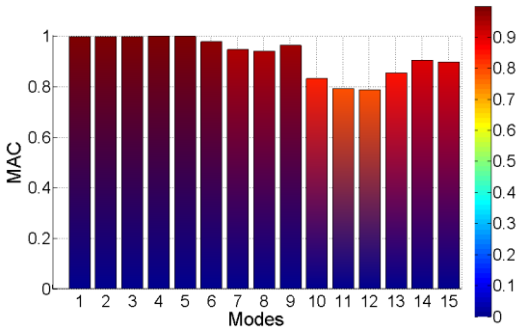


Figure 5.61: MAC between the first 15 modes of the bladed disk with the fixed contact and with a percentage of the contact stiffness

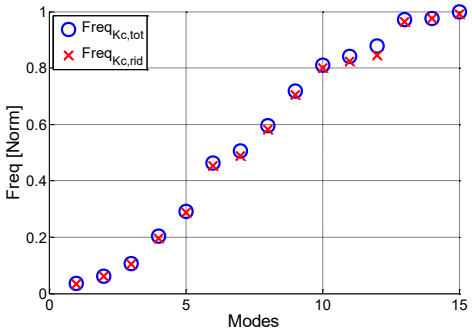


Figure 5.62: comparison of the frequency of the bladed disk with the contact elements at root joint between the total value of the contact stiffness and with a percentage of the contact stiffness

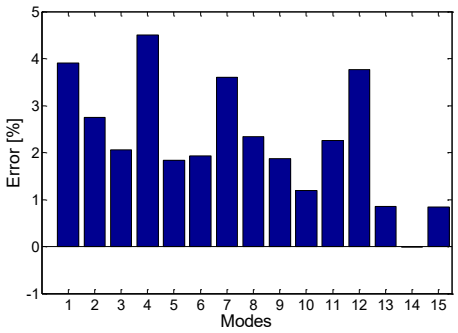


Figure 5.63: error in frequency of the bladed disk with the contact elements at root joint between the total value of the contact stiffness and with a percentage of the contact stiffness

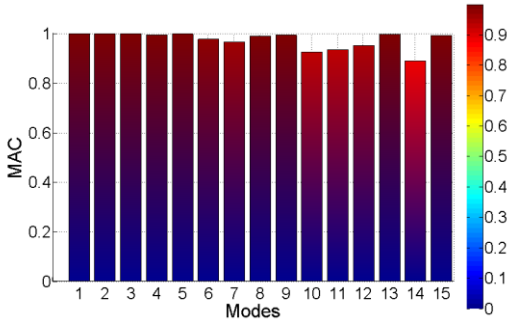


Figure 5.64: MAC between the first 15 modes of the bladed disk with the contact elements at root joint between the total value of the contact stiffness and with a percentage of the contact stiffness

Since the real stick condition of the bladed disk is not represented by the modal base, a forced response should be before performed to obtain the real stick condition of the system. This calculation is performed by increasing the number of modes preserved in the modal reduction. In particular the forced response will be calculated taken into account 1, 15, 120 and 360 modes. The results are shown in Figure 5.65. It is possible to note that the stick frequency goes towards its right value by increasing the number of modes with a significant reduction of the error from the response with one mode to the response with 360 modes.

With the same number of modes preserved in the modal reduction, a LCO analysis has been done (Figure 5.66). How happened for the Figure 5.58 and Figure 5.65, the variation of number of modes produces a more accurate response. In particular, the LCO responses go towards the LCO point obtained with physical approach. If all modes were preserved, the responses of modal and physical approaches would be equal.

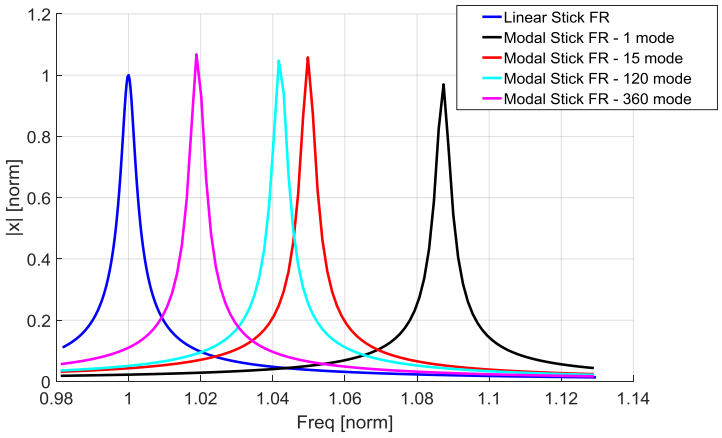


Figure 5.65: modal stick forced response by varying the number of modes

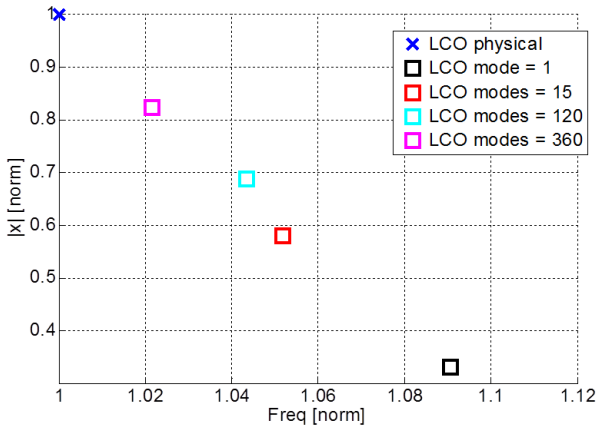


Figure 5.66: LCO calculation by varying the number of modes

The choice of this percentage of contact stiffness is arbitrary and depends on the system analyzed. However, two considerations are made to choose this value. The percentage should be not too big (over the 50%) because the system could be still

rigid and consequently the flutter calculation will be difficult. On the contrary, the percentage should be not too small (less than 10%) because in this case the system will be more loose and consequently a bigger number of modes will be necessary to have a good approximation of the physical results. Besides, a too small percentage of contact stiffness could produce a modal base not representative of the dynamic behavior of the real system.

### 5.4.2 Parameter variation

Finally, a Parameter variation of the bladed disk with the resolution of flutter equations in the modal domain is performed. These analyses will be done considering a modal base extracted from the software Ansys where the contact is simulated my means of springs witch values of stiffness are equal to a percentage of the total value of the contact stiffnesses. The number of modes that form the modal base is 15 (this number has been chosen to have a fast resolution of equations).

The parameters that influence the non-linear flutter analysis are:

- aero-damping ($\zeta_{aero}$);
- aero-stiffness ($\eta_{aero}$);
- friction coefficient ($\mu$);
- value of normal pre-load ($n_0$);
- distribution of normal pre-load ($n_0$);
- mechanical damping ($\zeta_m$).

To begin, an uniform distribution of normal pre-load is initially considered to perform a LCO calculation. The first parameters analyzed are the aero-damping and the friction coefficients. The values used are the same of the previous cases of study. Figure 5.67 shows the results of the flutter modal analysis. It is possible to see that the trend of LCO points is coherent with the results obtained in past analyses. In fact, the variation of aero-damping acts both on the frequency and on the amplitude in opposite mode (if the frequency decreases, the amplitude will increase and vice-versa), while the variation of friction coefficient acts overall on the amplitude. However, a small variation of the frequency is presented, but this can be neglected. Figure 5.68 shows the real deformation of the blade in flutter condition that is equal to the mode shape of the first flap mode. This equality is also highlighted by MAC number that has a value equal to 0.99. This value is also

obtained with a modal base of 360 modes, while if only the first mode is considered in the modal base, the MAC number is exactly 1.

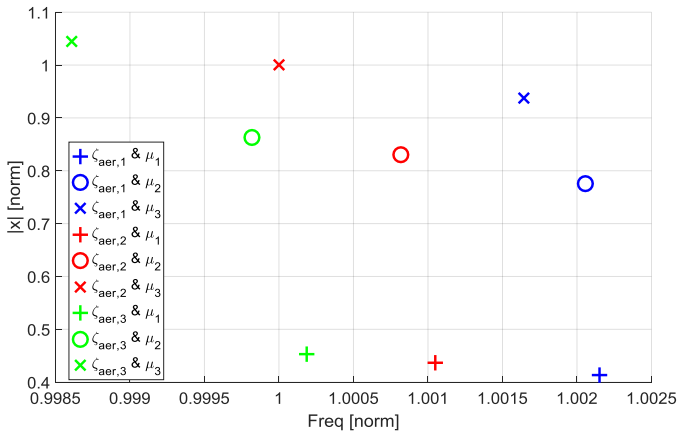


Figure 5.67: LCO calculation with the modal approach by varying the aero-damping and friction coefficients

Figure 5.68: the real deformation of the bladed disk in flutter condition

Figure 5.69 and 5.70 show the flutter responses calculated with the modal equations by varying respectively the value of the normal pre-load ($n_0$) and the aero-stiffness coefficient ($\eta_{aer}$). The trends reported in the figures are coherent with the past analyses. In fact, the variation of the value of the normal pre-load has a linear effect on the flutter amplitude, while the aero-stiffness produces only a slight increase of the LCO frequency.

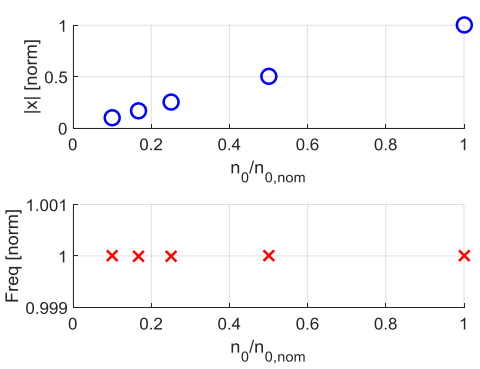


Figure 5.69: linear relationship between the LCO amplitude and frequency, and the normal pre-load in the modal approach

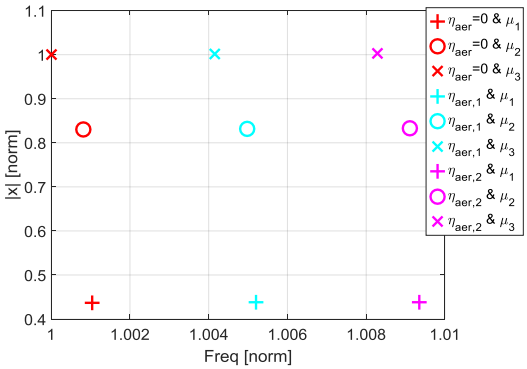


Figure 5.70: LCO response in the modal domain by varying the aero-stiffness parameter for three different friction coefficients.

### *5.4.2.1 Linear load on the blade root attachment*

Until now, the distribution of the normal pre-load has been considered uniform to simplify the calculation and the Parameter variation on the pre-load was performed varying the mean value $n_0$ (eq. 5.8). However, the distribution of the normal pre-load can be different from the uniform one due to the boundary condition of the system. For example, the geometric tolerances of the root joints or the aero-dynamic loads can change the distribution of normal pre-load. The first step in the variation of distribution of normal pre-load is to consider a linear distribution. In this section two types of linear distributions are considered: the first distribution is symmetric on the two contact surfaces (it has a convergent trend towards the center of the blade - see Figure 5.71), the second distribution is asymmetric (it has a parallel trend - see Figure 5.72). For the two linear distributions, three different gradients are considered.

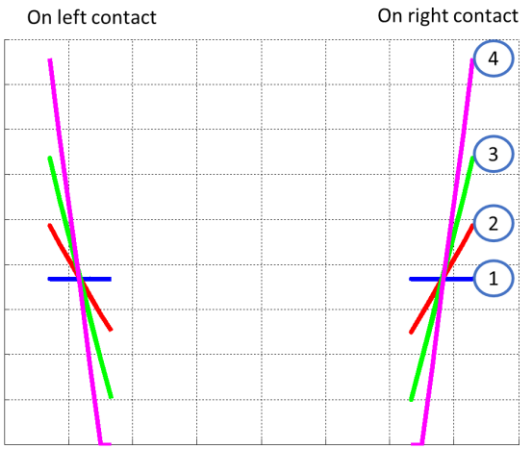


Figure 5.71: symmetric linear distribution


Figure 5.72: asymmetric linear distribution

All the six combinations of the linear distributions of the normal pre-load have the total sum of the forces equal to

$$N_0 = n_{0,u} N_{cont} \tag{5.22}$$

where $n_{0,u}$ is the mean value of the uniform distribution given by equation (5.8), i.e. overall the total normal force acting on the contact surface is equal for every distribution.

The two types of linear distribution have been before used to obtain a forced response of the bladed disk to understand the behavior of the system (see Appendix C). The forced response by varying the linear distributions shows a certain trend that is characterized by a reduction of frequency and an increase of amplitude if the gradient of linear distribution increases for both types of distribution. Now the same linear distributions will be applied to the flutter calculations to obtain the LCO points. The first type of linear distribution analyzed is that of Figure 5.71. To begin, a LCO calculation is performed by varying the gradient with a fixed set of aero-damping and friction coefficients. The result is shown in Figure 5.73, where it is possible to note that LCO response presents a minimum value of amplitude for the gradient 3 while the frequency has a decreasing trend by varying the gradients. The decrease of the LCO frequency by increasing the gradient of the symmetric distribution is due to a less rigid behavior of the contact as happened for the forced response. This condition produced, in these case, also a reduction of the amplitude of vibration because the

contact dissipates more energy, while in forced response the opposite effect happened. These two opposite dynamic behaviors are possible because the two excitation forces are different; in the forced response the external force is imposed in terms of direction and amplitude, while in the flutter response the excitation depends on the displacement. In particular, there is a magnitude order of five times in favor of the external force.

The reduction of the frequency and the increase of the dissipative energy means that in general the contact elements have a slip state more important than the other states, i.e. in a great part of oscillation period blade and disk are in contact and in the slip state. However, if the gradient is so high that some contact elements are always or near in separation state, the amplitude of flutter response will be bigger than the minimum value. This happens because the contact elements are less efficient (in the lift-off state there is no damping), i.e. they produce less dissipative energy. Consequently, to balance the aerodynamic energy, bigger LCO amplitudes are needed because in this way they are traduced in bigger relative displacements at contact that allow to the contact element to enter in contact and so produce dissipative energy.

With the linear distribution 3, a Parameter variation at variation of aero-damping and friction coefficients is made and presented in Figure 5.74. From the figure it is possible to see that the trend of the LCO amplitude is the same obtained with a uniform normal distribution of the normal preload. Instead, the increase of the friction coefficient produces the increase of the LCO amplitude and a slight increase of the corresponding frequency. However, this variation is so small that can be neglected.

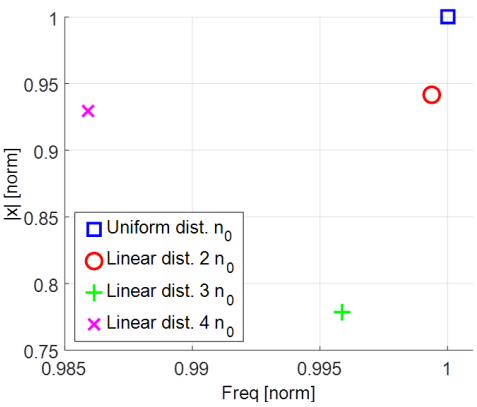


Figure 5.73: Parameter variation by varying the gradient of the first type of linear distribution with a fixed set of aero-damping and friction coefficients

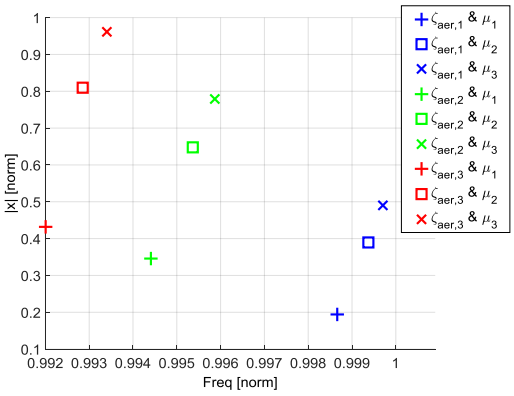


Figure 5.74: Parameter variation by varying the aero-damping and the friction coefficients for the first type of linear distribution with the gradient number 3

Figure 5.75 shows the Parameter variation by varying the gradient of the asymmetric linear distribution (Figure 5.72) with a given set of aero-damping and friction coefficients. At difference of the LCO trend of Figure 5.73, the LCO points do not present a minimum value, but a reduction of frequency with an increase of amplitude by increasing the gradient of the linear distribution. This means that the contact is less efficient because it is sufficient a small gradient to produce a separation on the contact elements with a negative effect. Figure 5.76 shows a Parameter variation by varying the aero-damping and the friction coefficients. It is possible to see that the trend of the LCO solutions is coherent with expectation. The slight reduction of the frequency can be neglected because it is minor than 0.5%.

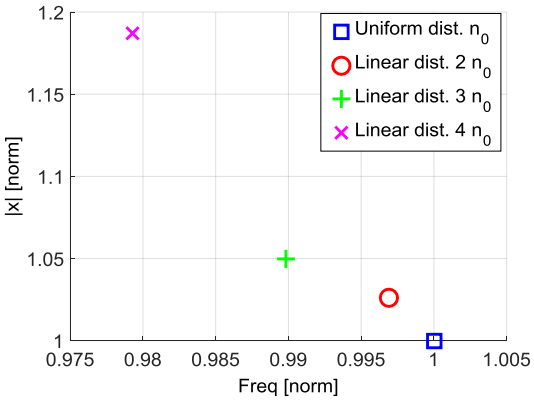


Figure 5.75: Parameter variation by varying the gradient of the second type of linear distribution with a fixed set of aero-damping and friction coefficients

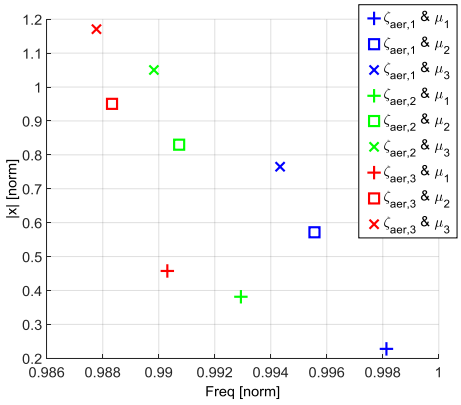


Figure 5.76: Parameter variation by varying the aero-damping and the friction coefficients for the second type of linear distribution with the gradient number 3

For completeness of analysis, the flutter results of an asymmetric linear distribution (Figure 5.77) with a gradient opposite to that of Figure 5.73 are presented in Figure 5.78. It is possible to note that, in this case of analysis, the LCO responses shows a minimum value of amplitude with a reduction of vibration frequency by varying the gradient. This means that this distribution of normal pre-load makes the contact elements more efficient than the distribution shown in Figure 5.73.

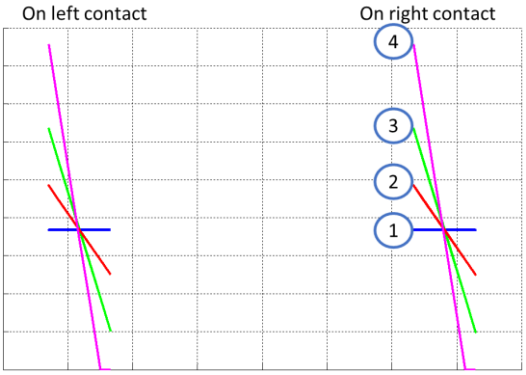


Figure 5.77: asymmetric linear distribution with a gradient opposite to that of Figure 5.87

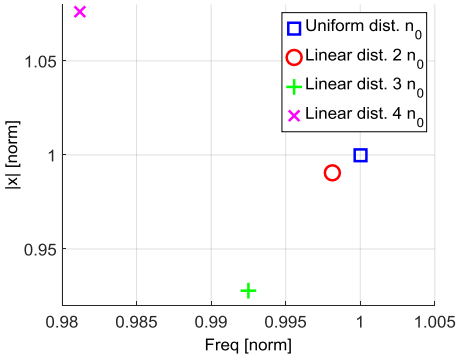


Figure 5.78: Parameter variation by varying the gradient of the third type of linear distribution with a fixed set of aero-damping and friction coefficients

All these distributions are possible because the geometric tolerance of the contact surfaces can produce them. For this reason, a Parameter variation has been performed to understand how the LCO responses can change in according to the distribution of the normal pre-load.

## 5.5 Conclusion

In this chapter, the study of the flutter behavior of a bladed disk have been analyzed using two different approaches: the physical approach and the modal approach. Besides, for the physical approach, the blade-alone configuration have been also studied to understand how analyze system not in cyclic symmetry or the blades in a cascade. Both approaches use a ROM of the bladed disk to reduce the dofs to analyze and so reduce the computation time. For this scope, a resolution of equation of motion, plus the energy balance, is performed in the frequency domain.

The two proposed approaches are both valid and have strong and weak points. The physical approach used the reduced matrices of mass and stiffness obtained by applying the CMS-CB technique plus, if it is necessary, the cyclic symmetry and Tran reductions. Blade and disk are separately reduced and they are linked together through the contact elements that are added in the resolution phase. This allows to reduce only once the system. In this way, the system can be used many times with different values of contact stiffnesses that are subject to a certain level of uncertainty. The sensitivity analyses on the bladed disk show coherent trends with the lumped parameter models by varying the different parameters taken into account. However, the matrices, although reduced, are still big because all master dofs are needed to solve the flutter problem. In fact, the dofs of the contact are used to calculate the dissipative energy, while the accessory nodes, that describe the airfoil, are used to calculate the aerodynamic energy. This involves a long calculation times in the frequency domain even if minor than the DTI. In general, the calculation time in frequency physical domain with only the first harmonic for a bladed disk is around the 12 hours. Naturally, if a MHBM is applied, the calculation time increases considerably.

The modal approach, instead, uses a modal reduction on bladed disk, i.e. this is described by a modal base that represents its dynamic behavior. At difference of the physical approach, the flutter analysis is fast (few minutes) even if many modes are necessary to describe well the system. However, the description of the model requires many attentions; in fact the blade and the disk should be linked

together, but not with a fixed root joint. This is necessary for two reasons: the first is that the modal base should be representative of the dynamic behavior of the system; the second because a fixed root joint does not allow to produce the dissipative energy needed to balance the aerodynamic energy. To satisfy these two requirements for the modal approach, a modification of the proposed method for the flutter analysis has been applied and verified. The verification has been made through calculation of the forced response both in physical and modal domains and through calculation of flutter response in the physical domain. This modification sees the introduction of a fictitious contact force to balance the addiction of stiffness in the modal base. Although the introduction of this force works well in the forced response, some problems arise in the flutter analysis. In fact, if the displacements at contact are not sufficient to produce the necessary dissipative energy the flutter analyses are not possible; on the contrary, if the initial point exists, the LCO point is obtained and the sensitivity analyses show a coherent trends. To perform a flutter response with a more rigid root joint, the modal base has only a percentage of contact stiffnesses, while the total values are given during the flutter calculation. This produces a stiffer behavior of the bladed disk that can be reduced using more modes in modal base (in this way the LCO goes towards the physical point). However, the flutter behavior at variation of the different parameters is right.

Both approaches show coherent trends with the lumped parameter models and allow to identify the parameters that mostly influence the flutter response. In particular the major effects on the LCO points are linked to the contact stiffnesses for the flutter frequency and to the value and distribution of the normal pre-load for the flutter amplitude. In particular, the distribution of the normal pre-load acts both on the frequency and on the amplitude of the flutter response producing a great variation of the LCO points that cannot be identified at priori. For this reason, a possible correct distribution of normal pre-load will be calculated by a non-linear static analysis in the software Ansys where the contact elements are added to the model to allow a numerical-experimental comparison.

# Chapter 6

# Numerical-experimental comparison

In this chapter a numerical-experimental comparison will be illustrated to validate the developed method using the bladed disk of Great 2020 project. The numerical results will be calculated with the modal approach because it is faster than the physical approach and gives an acceptable level of approximation of the LCO for the blade root contact joint. The method with the fictitious contact force is applied and the modal base extracted by FEM has a percentage of the contact stiffness. For these reason 360 modes are retained in the modal reduction to have a good approximation of the physical behavior of the bladed disk.

Experimental data have been obtained by GE Avio Aero facilities and details/values are restricted due to confidentiality reasons. The test article and the cold flow test will be first presented, then the comparison of the numerical results with the experimental data will be made for a selection of operative conditions.

## 6.1 Test article and cold flow test rig

The Test Article (TA) has been developed in order to have, as a fundamental characteristic, a great instability at flutter phenomenon. This choice has been made for different reasons:

- Have a sufficiently high level of instability so that it can be detected and measured more easily;

- Mitigate the risk related to the uncertainty of the value of the mechanical damping;
- Mitigate the risk related to the uncertainty of the sensitivity and reliability of the design tools;
- Test the effect of the alternate mistuning on a highly unstable blade array configuration.

To take into account all these reasons, different configurations of design model have been realized. The starting point was a preliminary configuration that was modified to reach a right compromise between the level of instability and a proper geometry of the blade representing a standard engine configuration (Figure 6.1).

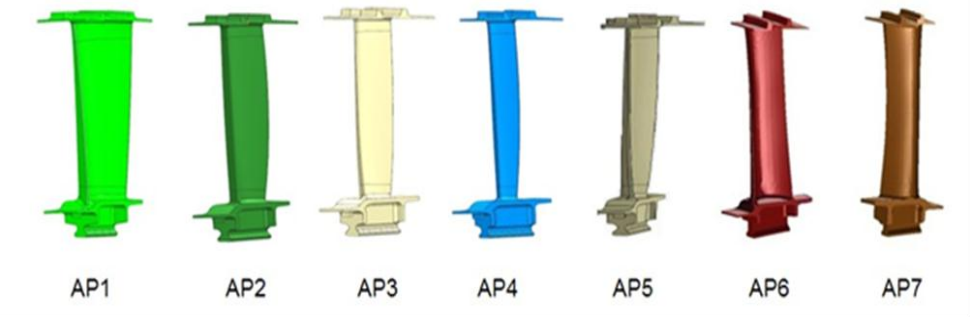


Figure 6.1: Evolution of the preliminary design of test articles

For every configuration of Figure 6.1, the effect of the variation of the geometric variables (for example the axial chord and surface of the airfoil) on the aerodynamic pressure distribution and on the stresses produced by centrifugal force has been studied by varying the radial coordinate of the test article. In Figure 6.2, the comparison between the airfoil area distribution along the airfoil length of two configurations of the blade is reported as example. This figure gives information about the aspect ratio of the blades and as a consequence on their stiffness and stability at flutter (the blade 3 has bigger aspect ratio than blade 1 and as a consequence is more unstable at flutter). Other analyses have been then performed to study the aerodynamic, dynamic and aero-elastic behaviors of each concept design of test article until the final design is obtained.

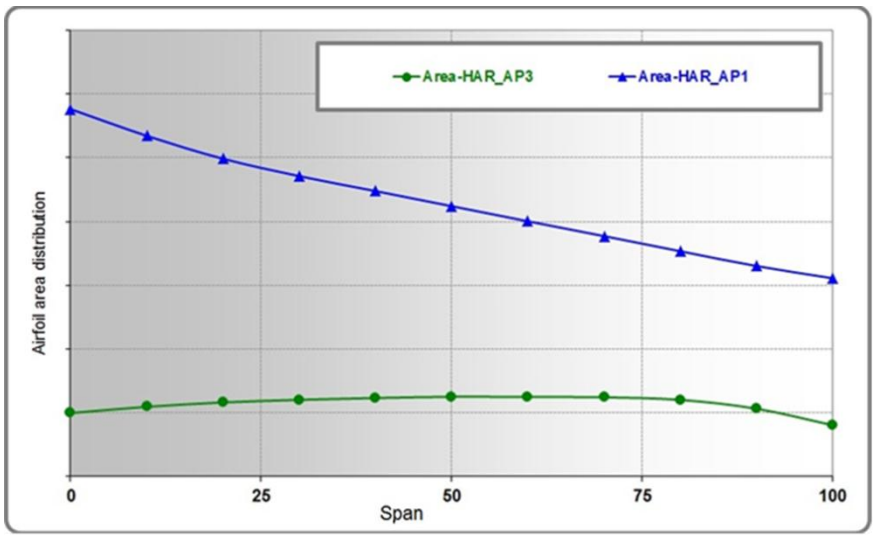


Figure 6.2: Comparison between the airfoil area distribution along the radial coordinate of TA AP3 and TA AP1

The final design represents the best compromise between a high level of instability and a proper geometry of the blade. On this geometry, an interchangeable configuration of interlocking has been studied to allow the addition or removal of the shroud contact to simulate the blade in tight and loose condition, and also in alternate mistuning condition. This is possible through the utilization of two different bars on the tip of the blade: one produces interference at interlocking, the other is an additional mass that changes the natural frequency of the blade without producing interference at the shroud.

The blades of the final configuration of the test article have been instrumented (Figure 6.3) and installed in the cold flow test rig (Figure 6.4). Ten blades have been instrumented with strain gauges (Figure 6.5) to measure the dynamic response of the bladed disk for 2 different modal families and the whole row was measured also with the Blade Tip-Timing measuring technique (beam shutter configuration was used consisting of a sender-receiver probe and a reflecting tape placed on the opposite side of the blade with respect to the probe). The test rig was also instrumented with accelerometers, thermocouple and proximity sensors to monitor additional possible vibration in the operative range.

Figure 6.3: test article bladed disk

Figure 6.4: cold flow test rig

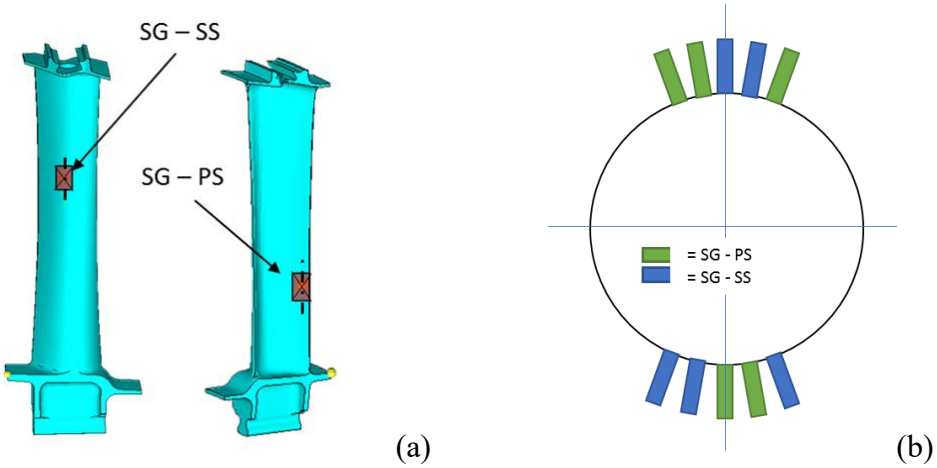


Figure 6.5: description of the position of the strain gauges on the blade (a) and position of the instrumented blades on the bladed disk

The cold flow test has been divided in different phases:

1. *Stair step test*: during the phase of stair step seventeen operative points have been tested starting with low Pressure Ratio and low Mass Flow, that were gradually increased afterwards, in order to define the off-design test point for the real test matrix. In this phase the blades are tuned.
2. *Test matrix tuned*: the points of the test matrix defined before have been tested for the tuned configuration.

3. *Tuned disassembly / mistuned assembly*: the tuned TA has been disassembled and the pattern 010101… of the alternate mistuning has been introduced in the bladed disk.
4. *Test matrix mistuned*: the same points of the tuned configurations have been also tested for the mistuned configuration.

The first two phases are very important because the numerical-experimental comparison has been made for the tuned configuration, and for this reason more details are presented in this study. In the stair step the values of Pressure Ratio and Mass Flow have been continuously increased to test more unstable points at flutter. This approach has been adopted for particular safety reasons in the operability of the rig, since the tests operate in a rotor configuration strongly unstable at flutter. Consequently, it was necessary to gradually increase the level of instability to not incur in dangerous aero-elastic vibrations;

The test matrix has been defined on the basis of the results of stair step and ten Operative Conditions (OC) have been tested using an incremental logic in terms of pressure ratio and mass flow. The results show high vibrational peaks, due to asynchronous vibrations clearly related to flutter LCO. The vibrations have been only measured through the strain gauges because the tip-timing measurements have been stopped giving reliable values only on a limited range of rpm. However, the measurements of tip-timing, showed asynchronous vibration due to the more unstable Nodal Diameter.

Figure 6.6 and 6.7 show respectively the variation of the simulated aero-damping (absolute values?) and the measured experimental data (minimum, maximum and mean values strains) for the ten operative conditions of the test matrix. It is possible to see that, from OC 1 to OC 10, the absolute value of aero-damping has an incremental trend that is linked to an increase of the pressure ratio, mass flow and also angular velocity of the bladed disk. An incremental trend is also shown by the mean value of the experimental measurements with exception of the ninth operative condition. Three operative conditions are analyzed for the numerical-experimental comparison. The chosen operative conditions are OC 6, OC 7 and OC 8. These OC have been taken into account because they have a good level of instability, with a linear trend of the mean value of the experimental data.

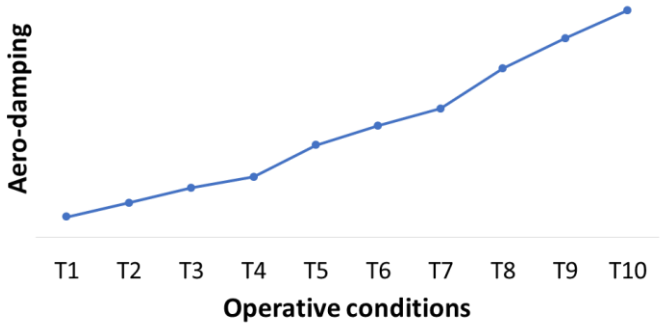


Figure 6.6: Simulated aero-damping coefficient trend by varying the operative conditions

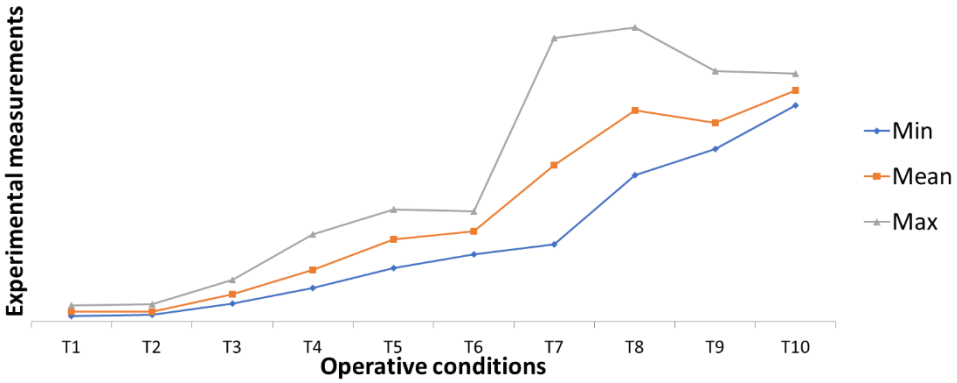


Figure 6.7: experimental measurements of strain gauges at variation of operative conditions (minimum, maximum and mean values)

The normal load distribution was updated in order to correspond to the centrifugal load produced at the rotation speed at which flutter conditions were met for these three OCs. Besides, the aerodynamic static load of the steady pressure distribution on the airfoils has been also considered. The corresponding simulations are shown in the following section.

## 6.2 Non-uniform distribution of the normal pre-load on the blade root attachment

In order to compare the simulations with the experimental results, the numerical results are performed by considering a normal load distribution calculated by means of a non-linear static analysis of the blade pulled by the centrifugal forces

during rotation and constrained to the disk by a layer of node-to-node contact elements. Also the static aerodynamic loads (tangential and axial forces) have applied in the pressure center because these can unbalance the blade and so the contact cannot be symmetrical for the two sides (see Figure 6.8).

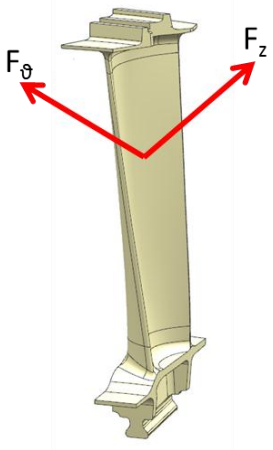


Figure 6.8: application of the static aerodynamic load in the pressure center

The nonlinear analysis is performed with the software FEM Ansys and contact element CONTAC52 is used since this is based on the penalty method where contact stiffnesses and friction coefficient are required. The used contact stiffness are those calculated in the previous chapter in section 5.2, while the value of the friction coefficient is that of $\mu_2$. Two non-linear static analyses are performed: in the first analysis only the centrifugal force is applied, while in the second the steady aerodynamic loads are also considered. The two distributions of the normal pre-load are respectively shown in Figure 6.9 and 6.10. In Figure 6.9a it is possible to note that the application of the centrifugal load produces a distribution of normal forces coherent with the distribution of the contact pressure (see Figure 5.8). In fact, along the principal (tangential) direction of slipping the pressure is concentrated at the borders of the contact surfaces and in this place the nodal normal forces have bigger values, while in the center smaller values are found. The Figure 6.9b shows the distribution of the normal pre-load along the axial direction where it is possible to see a linear distribution with a negative gradient. This happens because the conical disk supporting the blades tends to slightly open in ρ-z plane, i.e. the bladed disk has a radial positive displacement with a positive

rotation around the ϑ-axis (see Figure 6.11). The resulting contact state is locally characterized by a slip state.

The Figure 6.10a shows the distribution of the normal pre-load with both the application of the centrifugal and the steady aerodynamic loads along the tangential direction while Figure 6.10b shows the same distribution along the axial direction. It is possible to note that this distribution has two linear trends in the two directions of contact. In particular, along the tangential direction an asymmetric linear distribution is shown, while along the axial direction a linear distribution with a negative gradient is found. The asymmetric distribution is due to the application of the tangential aerodynamic force that produces an unbalance of the blade and as a consequence the contact is not more perfectly conform. Instead, the application of the axial aerodynamic force produces a linear distribution with a bigger gradient than the case of Figure 9b even if the centrifugal load is two orders of magnitude bigger than the axial force. This is possible because the moment arm of the centrifugal force with respect to the blade root joint is smaller than the arm of the aerodynamic force. However, the bladed disk tends to slightly open in the ρ-z plane. With these applied loads, the resulting contact state is different for the right and left contact surface, in fact the contact is respectively characterized by a slip and a stick state.

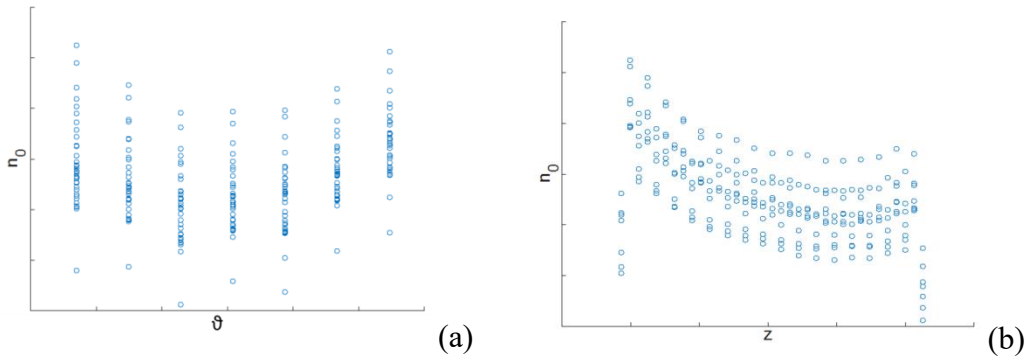


Figure 6.9: distribution of the normal pre-load for one contact side of the blade root joint with the application of the centrifugal force only – (a) tangential direction; (b) axial direction

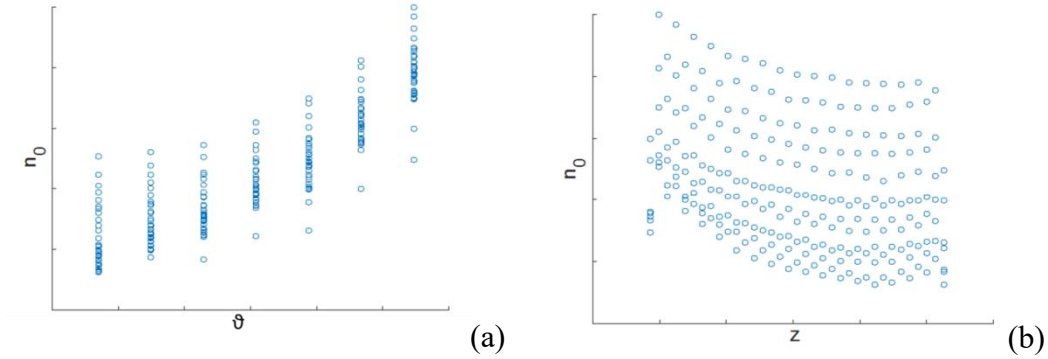


Figure 6.10: distribution of the normal pre-load for one contact side of the blade root joint with the application of the centrifugal and steady aerodynamic forces – (a) tangential direction; (b) axial direction

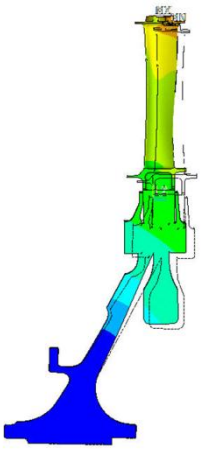

Figure 6.11: static deformation of the bladed disk

For each analyzed operative condition the two distributions of normal pre-loads are calculated and used to determinate the numerical results.

## 6.3 Numerical-experimental comparison

The experimental data that are used for comparison purposes are obtained from the strain gauges placed on ten different blades. The measurements has been post-processed (filtered and averaged) to plot the Campbell diagram. Micro-strain response has been detected at critical points in the Campbell diagram where LCO

occurs close to the mode shape characterized by the highest instability. The value of micro-strains of the strain gauges has been then converted in absolute displacements. The procedure is based on the hypothesis that the linear mode shape calculated by FEM does not change abruptly when the non-linear operative deformed shape is calculated (this hypothesis is verified in the previous chapter – see for example Figure 5.48). Therefore, it is possible to write the following relationship:

$$x : \varepsilon_{sg} = D_{FEM} : \varepsilon_{FEM} \tag{6.1}$$

where $x$ is the tip displacement to compare with simulations, $\varepsilon_{sg}$ is the measured micro-strain, $D_{FEM}$ is the modal tip displacement obtained for the mode shape of interest and $\varepsilon_{FEM}$ is the modal strains of the nodes corresponding to the strain gauges locations.

The numerical results for the comparison with experimental data have been obtained through the application of the corresponding distributions of normal pre-load for the chosen operative conditions. The structural data are those used in Figure 5.85 for the point with $\zeta_{mec,nom}$. The friction coefficient $\mu_2$ was chosen because it represents an intermediate value between the low and the high values of $\mu_1$ and $\mu_3$.

The numerical-experimental comparison with the distribution of normal preload of Figure 6.9 is reported in Figure 6.12, where the blue (circle marker) points are the LCO amplitude and the frequency of the simulation, while the red ones (circle marker) are the mean of the experimental data. In the same figure the measured minimum and maximum values among the ten post-processed measured values from the strain gauges as in equation (6.1) are also reported. The difference between numerical and experimental data (mean value and maximum value) is reported in Table 6.1.

In Figure 6.12, it is possible to see that the numerical amplitudes are bigger than the maximum measured values while the numerical frequencies are smaller than the experimental one. If the errors are considered, it is possible to note that the errors in frequency are near the same for the three operative conditions and they can be considered acceptable because smaller than 5%. Instead, the errors in amplitude are definitely bigger with a range between the 8% and 104% if the maximum measured values are considered, and with a range between the 81% and 148% if the mean values are considered.

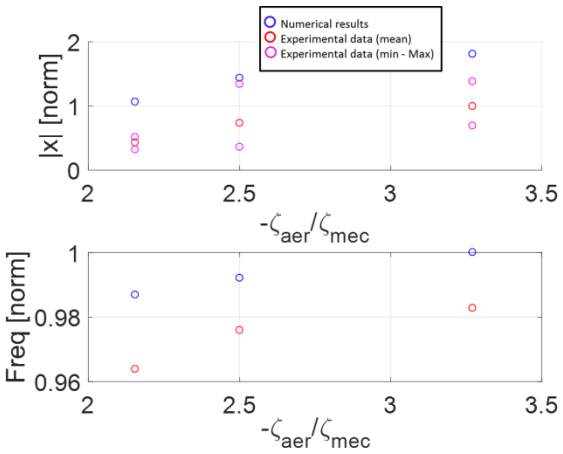


Figure 6.12: comparison of the numerical results (obtained with application of centrifugal force for definition of normal pre-load) with experimental data for three OC

| | Error in Amplitude (mean) | Error in Amplitude (max) | Error in Frequency |
|---|---|---|---|
| OC – 6 | 148% | 104% | 2.3% |
| OC – 7 | 95% | 8% | 1.7% |
| OC – 8 | 81% | 30% | 1.8% |

Table 6.1: LCO percentage difference between numerical results and experimental data (with respect to the mean value and maximum value)

A similar comparison with the experimental data is obtained with the numerical results calculated with the distribution of normal preload of Figure 6.10. Figure 6.13 and table 6.2 show respectively the graphical comparison and the errors in amplitude and frequency. It is possible to see that the errors in amplitude of OC-6 and OC-7 are smaller than the correspondent errors of table 1, while for the OC-8 the errors in amplitude are bigger. This last case is coherent with the results obtained in the previous chapter where the sensitivity analyses with an asymmetric distribution of normal pre-load is performed (see Figure 5.92) because the simulated aero-damping coefficient is the same ($\zeta_{aer,2}$). Instead, the errors in frequency between the two analyses are near the same, with only a small increase as shown in Figure 6.10.

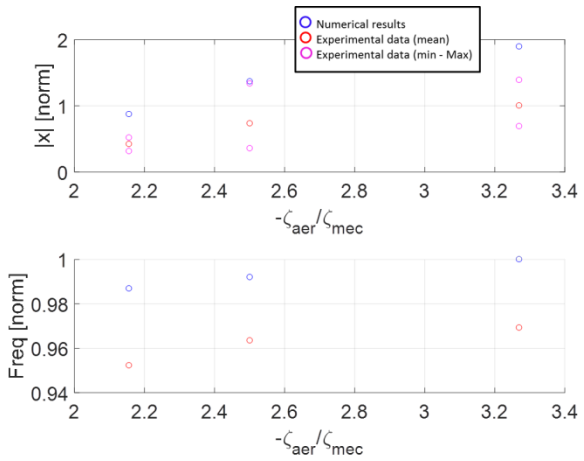


Figure 6.13: comparison of numerical results (obtained with application of centrifugal and aerodynamic static loads for definition of normal pre-load) with experimental data for three OC

| | Error in Amplitude (mean) | Error in Amplitude (max) | Error in Frequency |
|---|---|---|---|
| OC – 6 | 105% | 83% | 2.5% |
| OC – 7 | 85% | 1% | 2.1% |
| OC – 8 | 90% | 37% | 2.1% |

Table 6.2: LCO percentage difference between numerical results and experimental data (with respect to the mean value and maximum value)

The numerical amplitudes, as shown, are bigger than the experimental data with errors that cannot be neglected. These differences between the predicted amplitudes and the measured one could be due to different phenomena that are presented in real bladed disk, but not considered in the modeled system. One of these phenomena, for example, is the natural mistuning that breaks the cyclic symmetry of the bladed disk and could reduce the flutter amplitudes. In fact, the classical flutter is closely related to the IBPA and as a consequence to the cyclic symmetry. Besides, an aspect, that produces natural mistuning and acts on the distribution of normal pre-load, is the geometric manufacturing tolerance of the root joint. In fact, this tolerance could change how the contact between the

surfaces occurs producing a random distribution of normal pre-load. Since the distribution of normal pre-load is a very important parameter that influences the amplitude of the LCO point, the geometric tolerance on the root joint could have a significant impact on the calculated and measured values of the flutter amplitudes.

A not perfect conform contact between the surface of the blade and the disk can be supposed by knowing the value of tolerance through an experimental test. In fact, usually, the value of tolerance is of the order of hundredths of mm, while the value of penetration (allowed by the compression of the penalty stiffness) that gives the mean value of the normal pre-load is usually of the order of magnitude of the roughness. Since these two values are very different, the geometric tolerance can produce a geometric contact that could improve the mitigation of flutter phenomenon but also the contrary. Figure 6.14 shows an experimental test made on a dummy blade (VITAL[1] project). The root joint of the dummy blade of the VITAL project was designed with the tolerances of real blades.


Figure 6.14: experimental test on the root joint of VITAL project

The test was performed in the AERMEC laboratory of the Department of Mechanical and Aerospace Engineering of the Polytechnic of Turin where, on the root joint of a blade, a pressure sensitive film has been applied. The blade was then put in the disk and pushed against the contact surface of disk with a screw that simulates the centrifugal force. Since the applied film is sensible to the pressure, where the bodies are in contact, the film assumes a magenta color while it remains white if the bodies are in lift-off. From the Figure 6.14, it is possible to

1 EnVIronmenTALly Friendly Aero Engine (VITAL), Project ID 12271, Funded under EU FP6-AEROSPACE, From 2005-01-01 to 2010-12-3.

see how the contact at root joint is not perfect and uniform, in fact there are parts of the film that have a strong magenta color surrounded by a white color.

The geometric tolerance of the surface of the root joint is difficult to simulate because, in the value of tolerance, the surface can assume any form. For this reason, the asymmetric distribution of Figure 6.10 is initially taken as a basis and then a variation of this is applied to simulate the tolerance on the root joint. Since it is impossible to know what is the real distribution of the normal pre-load, two linear variations of pre-load along the mainly directions of sliding (tangential and axial directions) have been supposed. An example of these two linear variations are reported in Figure 6.15a and 6.15b, where it is possible to note that positive and negative values exist. This trend is always applied and it has been made this choice to have a constant total value of normal force, i.e.

$$\sum N_{asym} = \sum N_{tot} \tag{6.2}$$

where $N_{asym}$ and $N_{tot}$ are respectively the vector of the asymmetric normal force and the vector of the normal force with the application with application of two linear variations (see eq. 6.4). The extreme values of two linear variations have been chosen as a random percentage of mean value of the asymmetric normal force:

$$\Delta_{var} = \pm p * mean(N_{asym}) \tag{6.3}$$

where $p$ is the percentage variation. In this way the distribution of the normal pre-load can be easily obtained as:

$$N_{tot} = N_{asym} + N_{\vartheta,var} + N_{z,var} \tag{6.4}$$

where $N_{\vartheta,var}$ and $N_{z,var}$ are respectively the vectors of the tangential and the axial variations. Of course, a check on the possible negative values of force acting on the contact nodes is made and if these negative values are presented the nodal normal force is set to zero

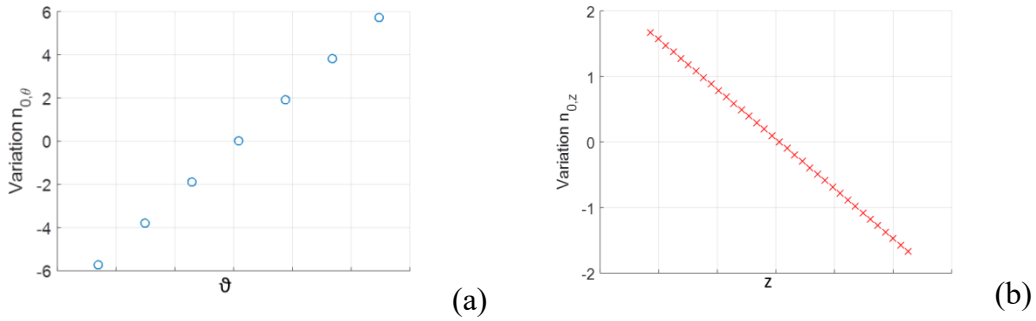


Figure 6.15: linear variations of the pre-load along the mainly directions of sliding - (a) tangential and (b) axial directions

The percentage variation *p* can assume any values in a fixed range [*-a, a*]. The value of *a* parameter was set to 50% and four values of *p* are randomly chosen for each calculation: 2 for the tangential and axial directions on the right root joint and 2 for the tangential and axial directions on the left root joint. In this way, the two contact surfaces have a different and independent distribution of the pre-load.

Figure 6.16 shows the LCO results by varying the normal pre-load where 250 calculation cycles are made for the OC-8. The blue diamond marker represents the base point (no variation is applied to the normal pre-load – this point is equal to the corresponding point of Figure 6.13), while the red 'x' points are the LCO solutions for each random variation of the normal pre-load. It is possible to see a cloud of red 'x' points around the base solution where better solutions exist, but also worse solutions in terms of flutter amplitude (the errors in frequency are always acceptable). The mean values and the standard deviations in frequency and amplitude values of the cloud of points are reported in table 6.3 for the three analyzed operative conditions. The values are normalized with the frequency and the amplitude of the base point (as a ratio). It is possible to note that the mean values are close to the frequency and the amplitude of the base point and this is logic because the starting normal distribution is that of Figure 6.10. Similar results are also obtained for the other two operative conditions. If the maximum and minimum values in amplitude are considered (see Table 6.4), the errors in amplitude considerably change. In particular, the minimum points are closer to the mean values of the experimental data with a maximum error of 53% for the OC-6. Instead, if the OC-7 is considered, it is possible to see a negative error in amplitude compared to the maximum measured value. This means that the minimum numerical result stays inside the range of the measured data, but this is

a lucky case because the range of experimental data in this operative condition is very large.

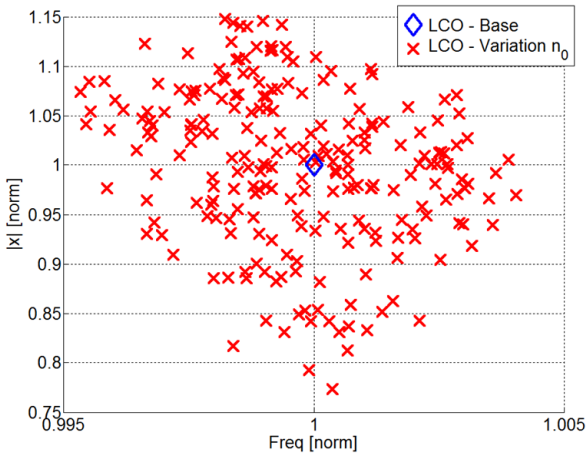


Figure 6.16: LCO points at variation of normal pre-load with 250 calculation cycles for the third operative condition

| | Mean value | | Standard deviation | |
|---|---|---|---|---|
| | Amplitude | Frequency | Amplitude | Frequency |
| OC – 6 | 1.02 | 0.99 | 0.13 | 1.7e-3 |
| OC – 7 | 0.99 | 0.99 | 0.09 | 1.9e-3 |
| OC – 8 | 0.99 | 0.99 | 0.08 | 1.9e-3 |

Table 6.3: normalized mean value and standard deviation of the LCO solutions with the variation of the normal pre-load for the three considered operative conditions

| | Minimum value | | Maximum value | |
|---|---|---|---|---|
| | Error in Amplitude (mean) | Error in Amplitude (max) | Error in Amplitude (mean) | Error in Amplitude (max) |
| OC – 6 | 53% | 26% | 179% | 130% |
| OC – 7 | 39% | -23% | 120% | 22% |
| OC – 8 | 47% | 6% | 119% | 57% |

Table 6.4: error in amplitude of the minimum and maximum LCO solutions for the three considered operative conditions

## 6.4 Conclusion

In this chapter a numerical-experimental comparison has been made to validate the developed method. Three of the ten measured operative conditions have been chosen and the friction coefficient $\mu_2$ and mechanical damping $\zeta_{mec,nom}$ have been set. The LCO calculation was performed with two types of normal distributions: the first obtained only from the application of the centrifugal force while in the second the aerodynamic static load is also applied.

The numerical-experimental comparison shows that the numerical results show in general bigger amplitudes and lower frequencies than the experimental data, with errors that cannot be neglected for the amplitudes. On the contrary, the errors in frequency are around the 2% and they can be considered acceptable.

Since the method has been developed to be implemented in the industrial process, the calculation of numerical amplitude bigger than the experimental one is positive because in this way it is possible to be conservative in the design phase. However, the errors in amplitude are very large, but these can be opportunely explained if the differences between the simulated model and the tested bladed disk are considered. In fact, the model of the bladed disk analyzed is considered tuned, while the real bladed disk has a certain level of natural mistuning. This property acts on the flutter instability with a benefic effect because it breaks the cyclic symmetry that is a fundamental parameter for the flutter onset. Besides, the natural mistuning acts also on the distribution of the normal pre-load that is an

important parameter in the prediction of the flutter amplitude. In this case, an important role is played by the geometric tolerance of the root joint because, in according with the type and shape of the contact, different distributions of normal pre-load could exist. Since it is not possible to predict the real contact surface, for each contact surface two linear variations along the tangential and axial directions of sliding have been considered to take into account the tolerance of the root joint. The results obtained are interesting because they show that the influence of the geometric tolerance on the normal distribution is big; in fact the errors in amplitude show a great reduction (also of the 50%). Of course, next to this reduction, an increase of errors may exist.

Since the general natural mistuning of the bladed disk and the geometric tolerance on the root joint that respectively mitigate the flutter and change the distribution of the pre-load, the calculation methodology can be considered useful to be included for a preliminary check in a design process.

# Chapter 7

# Conclusion

The study of the non-linear aero-elastic behavior of a bladed disk in the presence of friction damping is presented. To perform this study a methodology for the calculation of the LCO of a blade array in a tuned configuration was developed. This methodology is based on the mathematical formulation of the work produced by the airflow on the blade airfoil that induces flutter excitation. Linearization of the fluid-structure coupling in terms of a linearized aerodynamic parameter and linearized friction forces is implemented in a numerical code.

The method for LCO calculation has been before developed and applied to three lumped parameter models, where different properties are studied and fundamental hypotheses are introduced. For all systems taken into account the aero-damping parameter has been fixed a priori and interpreted as a viscous damping with negative sign. Instead, the external force due to the engine order excitation have not been considered, i.e. only the self-excited vibration have been studied. This allowed to use a one-way method based on the resolution of the equations of motion in the frequency domain together with the energy balance to have a well-conditioned problem.

The sensitivity analyses, by varying the aero-damping and friction coefficients, have shown that the fluid-structure interaction at level of the structure does not depend on the type of structure, but from the dynamic behavior of the structure. In fact, the three systems analyzed have the same mode shape unstable at flutter, while the other modes, if presented, are stable and do not give any significant contribution to the solution, the results show similar trend that are in accordance

with those of Griffin and Sinha [58]. In particular, the flutter analysis presents two solutions, one stable at low amplitude and bigger frequency, and one unstable at big amplitude and lower frequency. The Parameter variation shows that the behavior of the contact element has a great influence on the final result because from this depends the quantity of dissipative energy that can balance the aerodynamic energy.

The method developed for the lumped parameter models has been easily extended to study a real model of a blade or a bladed disk since the definition of the aerodynamic matrix depends on the dynamic behavior of the system. Following this method, two different approaches have been developed:

- a physical approach;
- a modal approach.

The first approach is based on the reduced matrices of mass and stiffness obtained by a CMS-CB, cyclic symmetry and Tran reductions; while in the second approach a modal reduction is applied. Both approaches have been used to study the flutter behavior of the bladed disk of the region Piedmont project Great-2020.

The two proposed approaches are both valid and have strong and weak points. For the physical approach blade and disk are reduced separately and linked together by means of the contact elements that are added in the resolution phase. This gives the advantage to reduce once the system that can be then used many time with different values of contact stiffnesses that are subjected to a certain level of uncertainty. However, the reduced matrices are still big because all master dofs should be solved together and iteratively to calculate the LCO response, i.e. it is not possible to divide the non-linear dofs from the linear dofs as it is usually made for the forced response. This involves a calculation time of about 12 hours to obtain only one LCO point, that is considered bigger if compared with the typical calculation time of the modal approach (few minutes), but it is smaller than DTI. Naturally, if the number of harmonics considered in the Fourier series is different from 1, the calculation time has a great increase.

In the modal approach the description of the model requires attention since blade and disk should be linked together, but not with a fixed root joint. The connection between blade and disk in the modeled system is necessary because the modal base should be representative of the dynamic behavior of the system; while a not-fixed root joint allows to produce the dissipative energy needed to balance the

aerodynamic energy. To satisfy these two requirements for the modal approach, this not-fixed connection was performed by means of spring in the FE model and a fictitious contact force has been introduced into the equation of motion to balance the additional stiffness in the modal base. The introduction of this fictitious contact force has been verified through calculation of the forced response both in the physical and modal domains and through calculation of the flutter response in the physical domain. The results show that the equations of motion so structured are able to calculate an exact forced response both in the physical and modal domain, but problems arise in the flutter analysis for the modal approach. In fact, if the displacements at the contact are not sufficient to produce the necessary dissipative energy the flutter analyses are not possible. For this reason, in order to perform a flutter analysis with the modal approach, a looser connection in the FE modal has been implemented by means of a percentage of the contact stiffness instead of the whole value. The same quantity of stiffness of the springs is then balance by the fictitious contact force in the frequency domain, non-linear simulation.

Both approaches show coherent sensitivity analyses with the trends of the lumped parameter models and allow to identify the parameters that mostly influence the flutter response beyond the aero-damping and friction coefficients. These parameters are the contact stiffnesses and the value and distribution of the normal pre-load. In particular great attention should be paid in the definition of the contact stiffnesses because they do not only influence the frequency of the system but also the distribution of the normal pre-load. For these reason, an opportune calculation of the contact stiffness was performed on the basis of the geometry of the dovetail attachment using lagriangian method that allows to determinate the states of the contact without the knowledge of the stiffness itself.

Since the distribution of the normal pre-load acts on the flutter amplitude, this has been calculated through a non-linear static analysis by FEM where two different load conditions are applied; in the first case only the centrifugal force is applied, while in the second case also the steady aerodynamic loads are considered. These distributions have been used to determinate the numerical results to compare with the experimental data obtained in a cold flow rig. Three operative conditions, with different values of aero-damping and centrifugal force, were analyzed and compared to experimental data in terms of errors in amplitude and in frequency. The results show a good comparison for the vibration frequencies (the general errors is about 2%), while in amplitude the errors are bigger. The usual numerical response compared to the mean value of the experimental data is twice this value.

This difference between the numerical results and the experimental data is due to difference between the modeled and real bladed disks. In fact, the model of the bladed disk analyzed by this method is considered perfectly tuned, while the real bladed disk has a certain level of mistuning. This property acts on the classical flutter with a beneficial effect because it breaks the cyclic symmetry that is a fundamental parameter for flutter appearance. A source of natural mistuning that has a great effect on the amplitude of the flutter response is the geometric tolerance of the root joint because, according to the type and shape of the contact, different distributions of the normal pre-load could exist and as a consequence LCO point can have different values. The effect of geometric tolerances, even if difficult to simulate because the contact surfaces can assume any form inside the value of geometrical tolerance, has been introduced in the method by considering two linear variations of the distribution of normal pre-load along the tangential and axial directions of sliding. The results show a significant influence of the geometric tolerance on the LCO amplitude; in fact for each random variation of the pre-load, a different solution has been obtained that can be better or worse in amplitude than the LCO point calculated with the starting distribution of normal force. In particular, the best points of the three operative conditions analyzed present a reduction of the error in amplitude of about 50%.

For these reasons, the general natural mistuning of the bladed disk and the geometric tolerance on the root joint that respectively mitigate the flutter and change the distribution of the pre-load, the errors in amplitude, even if bigger, can be considered acceptable.

## 7.1 Industrial impact

The introduction of the developed method in the industrial process may have a positive effect since it will be possible to change the current design process. From a design process of the blades based on the limit of instability that restricts the possibility of innovative solutions, the blades could be designed according to design guidelines related to HCF since the instability could be quantified in terms of amplitude and frequency of vibration and so new design solutions could be possible.

For this purpose, the presented method shows the possibility to calculate the vibration amplitudes in the flutter conditions through a numerical-experimental comparison. Instead, the sensitivity analyses for the calculation of the flutter response show the importance of the blade root joint in the generation of the non-

linear contact forces when no other friction damper is presented. Besides, the importance of the blade root joint is not closely related to the flutter calculation, but it has a great effect on the resonance peak. In fact, the results show how a suitable distribution of the normal pre-load can reduce the resonance peaks or the flutter amplitudes and as a consequence an optimization process of the dovetail attachment may be thought to have the best dynamic behavior.

## 7.2 Future developments

Future possible extension of the friction flutter method may concern two main field: the inclusion of more unstable nodal diameters and the inclusion of this methodology in the non-linear aerodynamic analysis.

With the inclusion of more than one nodal diameter associated to a negative aero-damping coefficient, a more accurate dynamic behavior of the bladed disk is simulated. The great problem is due to the calculation of the contact forces when more unstable mode shapes exist since the ND associated to the unstable modes are not commensurable. This yields a quasi-periodic oscillation of the blades in the frequency domain resolution of the equation of motion. The calculation of the non-linear response is difficult to solve in this case since the hysteresis loop of the contact model is open and as a consequence the simple FFT approximation is not accurate.

With the inclusion of the developed method in the non-linear aerodynamic analysis, a two-way coupled method is necessary. The purpose of a two-way coupled method is to foresee and determinate the flutter in non-linear condition as in the transonic flutter.

Since the definition of the contact stiffnesses is essential to calculate the response of the bladed disk, both for the forced response and flutter, since they influence the distribution of the normal pre-load, a more accurate and general calculation of these parameters may be developed to have more accurate results.

# Appendix A

## Fictitious contact force applied on a lumped parameter model

The method presented in the section 5.4.1 has been initially applied to a lumped parameter model of 12 sectors that was reduced in cyclic symmetry considering ND=1. The model is described in Figure A.1.

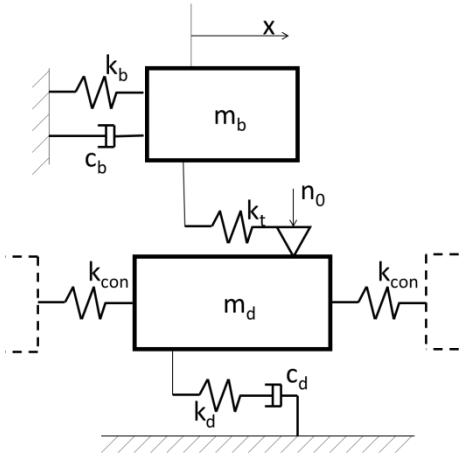


Figure A.1: lumped parameter model for the application of the fictitious contact force

The method with the application of a fictitious contact force has been applied both for the forced and flutter responses. For the two analyses, the calculations have been performed considering only the first harmonic both in the physical and modal domains. The physical equations used for the forced response are:

$$[M]\ddot{x} + [C]\dot{x} + [K_{bd}]x = F_e + F_{nl} \quad \text{(EqA.1 a)}$$

$$[M]\ddot{x} + [C]\dot{x} + [K_{bd} + K_c]x = F_e + F_{nl} - F_{fit} \quad \text{(EqA.1 b)}$$

while the equations in modal domain are:

$$[m_{mod}]\ddot{q} + [c_{mod}]\dot{q} + [k_{mod}]q = f_{e,mod} + f_{nl,mod} \quad \text{(EqA.2 a)}$$

$$[m_{mod}]\ddot{q} + [c_{mod}]\dot{q} + [k_{mod,s}]q = f_{e,mod} + f_{nl,mod} - f_{fit,mod} \quad \text{(EqA.2 b)}$$

Figure A.2 shows the forced response of the system solving the equations (EqA.1). The forced response was calculated with the contact in stick condition and it is possible to see that the linear response, the solution of eq. (EqA.1a) and the solution of eq. (EqA.2b), where the fictitious force is used, are perfectly overlapped. The same thing happens with the resolution of equation EqA.2 (see Figure A.3).

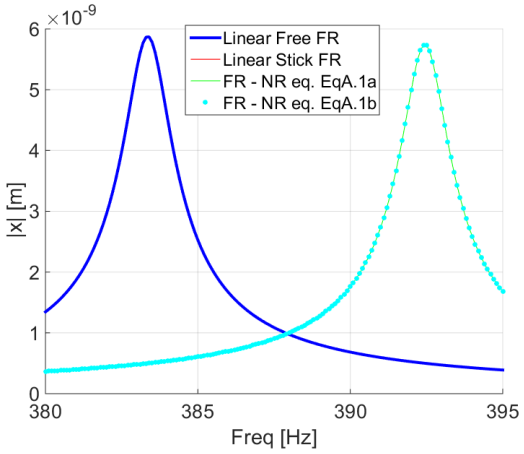


Figure A.2: forced response of a lumped parameter model with the solution of the equations in the physical domain: blue line – linear free response; red line – linear stick response; green line – Newton-Raphson resolution of eq. (EqA.1a) in stick condition - Newton-Raphson resolution of eq. (EqA.1b) in stick condition

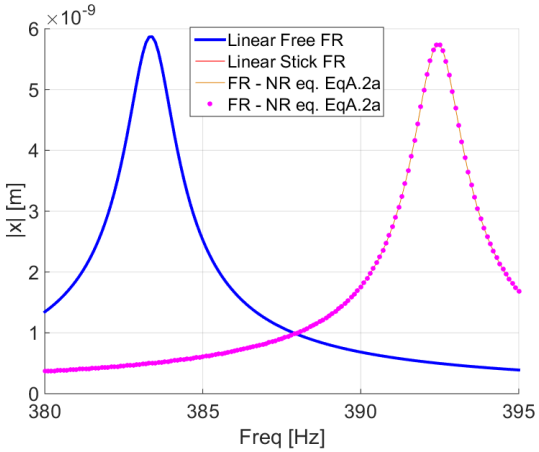


Figure A.3: forced response of a lumped parameter model with the solution of the equation in the modal domain: blue line – linear free response; red line – linear stick response; green line – Newton-Raphson resolution of eq. (EqA.2a) in stick condition - Newton-Raphson resolution of eq. (EqA.2b) in stick condition

The solution of the equation of motions (EqA.1) and (EqA.2) with the contact in stick condition is easy because the behavior of the system in this case is linear. More complex is the calculation of forced response if the contact can slip. Figure A.4 shows the damped forced responses of lumped parameter model in the physical domain for three values of normal pre-load ($N_1$=100 N, $N_2$=200N and $N_3$=500N). It is possible to note that the solutions of eq. (EqA.1a) and (EqA.1b) are exactly the same for three values of normal pre-load and also the trend of the forced responses are right. In fact, the resonance peak goes from the free condition to the stick condition passing for a minimum value of resonance amplitude. Similar solutions are obtained from the solution of eq. (EqA.2a) and (EqA.2b). The comparison of the four solutions (2 in physical domain and 2 in modal domain) is shown in Figure A.5 for the normal pre-load $N_2$.

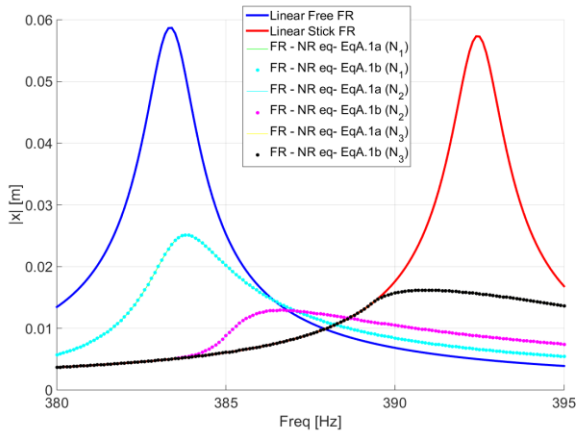


Figure A.4: damped forced responses obtained by solution of eq. (EqA.1a) and (EqA.1b) for three different values of normal pre-load (N1=100 N, N2=200N and N3=500N)

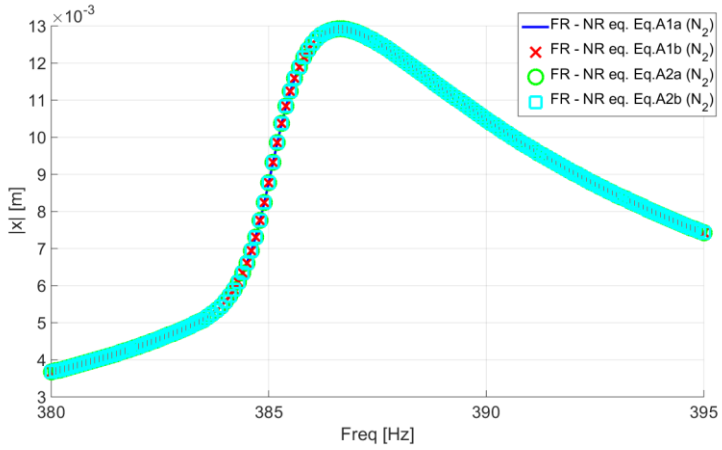


Figure A.5: comparison of damped forced responses with normal pre-load $N_2$ obtained by resolution of eqs. (EqA.1a), (EqA.1b), (EqA.2a) and (EqA.2b)

The equation of motions (EqA.1) and (EqA.2) for the forced response can be easily modified for the calculation of the flutter response. In fact it is sufficient to remove the external synchronous force $F_e$ and to add the aero-damping and the aero-stiffness matrices. In this way the equation of motions for the flutter analyses are:

$$[M]\ddot{x} + [C]\dot{x} + [C_{aer}]\dot{x} + [K_{bd}]x + [K_{aer}]x = F_{nl} \quad \text{(EqA.3a)}$$

$$[M]\ddot{x} + [C]\dot{x} + [C_{aer}]\dot{x} + [K_{bd} + K_c]x + [K_{aer}]x = F_{nl} - F_{fit} \quad \text{(EqA.3b)}$$

in physical domain, while in modal domain the equations are:

$$[m_{mod}]\ddot{q} + [c_{mod}]\dot{q} + [c_{aer,mod}]\dot{q} + [k_{mod}]q + [k_{aer,mod}]q = f_{nl,mod} \quad \text{(EqA.4a)}$$

$$[m_{mod}]\ddot{q} + [c_{mod}]\dot{q} + [c_{aer,mod}]\dot{q} + [k_{mod,s}]q + [k_{aer,mod}]q = f_{nl,mod} - f_{fit,mod} \quad \text{(EqA.4b)}$$

Figure A.6 and A.7 show the flutter responses of the lumped parameter model respectively in physical domain and in modal domain. From these two figures it is possible to see that the flutter responses of eq. (EqA.3a) and (EqA.3b), and (EqA.4a) and (EqA.4b) are practically the same.

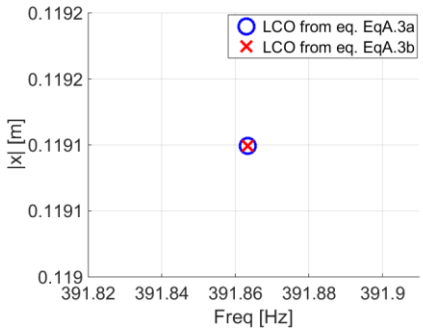


Figure A.6: LCO calculation in the physical domain obtained from the solution of eq. (EqA.3a) and (EqA.3b)

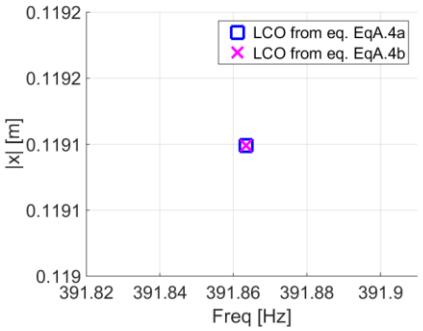


Figure A.7: LCO calculation in the modal domain obtained from the solution of eq. (EqA.4a) and (EqA.4b)

The results obtained for a lumped parameter model are very important because show adding a fictitious contact force to balance a stiffness matrix in stick condition is possible to obtain the right dynamic behavior of the system using both the physical and the modal domains. These results are used as starting point to apply this method to FE model such as the model of Great-2020 blade.

# Appendix B

## Physical approach with a fictitious contact force applied on a bladed disk

In the Appendix A, the fictitious contact force has been applied to a lumped parameter model showing good results. In this section, the same method is applied to FE model of the bladed disk of G2020 project using physical matrices.

The calculation of the forced and flutter response of a bladed disk with a physical approach can be easily done using the equation of motions (Eq.A1a) and (Eq.A3a) because the blade and the disk can be separately modeled and then linked together with the contact elements. However, to demonstrate the potentiality and correctness of the method with the fictitious contact force, the equations (Eq.A1b) and (Eq.A3b) will be now applied.

The forced responses in physical domain are reported in Figure B.1 and B.2. Figure B.1 shows the forced response in stick condition, while the Figure B.2 shows the damped forced response. Both figures show that the solution of eq. (Eq.A1b) gives the same results of eq. (Eq.A1a), i.e. the two methods are interchangeable for the calculation of the forced response.

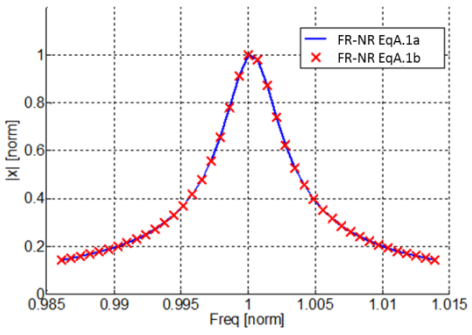


Figure B.1: stick forced response in the physical domain

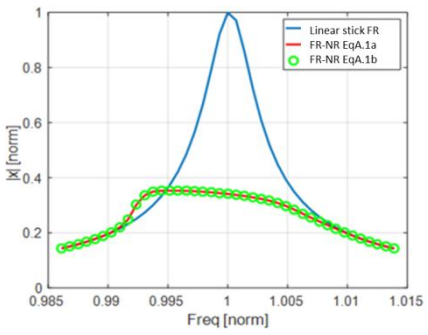


Figure B.2: damped forced response in the physical domain

Figure B.3 shows instead the flutter response using the equation (Eq.A3a) and (Eq.A3b) by varying the friction and the aero-damping coefficients. The results with the fictitious contact force have the correct trend at variation of the two parameters, but more important the results obtained from the two equation of motions are the same.

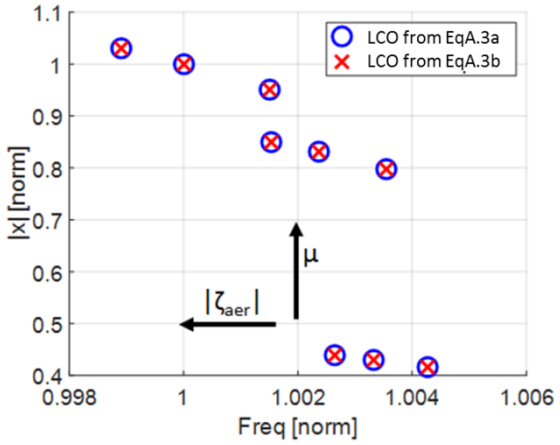


Figure B.3: LCO calculation in the physical domain using the eq. (Eq.A3a) and (Eq.A3b)

# Appendix C

## Forced response with a linear distribution

The two linear distribution of Figure 5.71and 5.72 are used in this appendix to calculate the forced response of the system. This is made to understand the effect of linear distribution in a simpler and well-known case such as the forced response. Figure C.1 shows the forced responses where the linear distributions of Figure 5.71 are applied. It is possible to note that the forced response with uniform distribution has the minor amplitude of resonance, while with the increase of the gradient the resonance peak presents a reduction of the frequency and an increase of the amplitude. This dynamic behavior of bladed disk is due to the efficiency of the contact elements. In fact, with the increase of the gradient of the symmetric distribution there is a reduction of stiffening effect of the contact elements and consequently the resonance frequency decreases; while the resonance amplitude increases because the contact loses effectiveness. For example, the increase of gradient produces a hysteresis loop of the contact elements with lift-off state more important than the slip state and consequently the contact produces less dissipative energy. Similar forced responses are shown in Figure C.2 where the asymmetric linear distributions of Figure 5.72 are applied. Also in this figure, the minimum value of resonance amplitude is reached for the uniform distribution, while the increase of the gradient produces a reduction of the frequency and an increase of the amplitude.

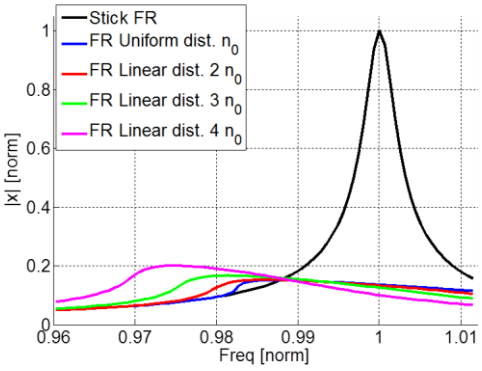


Figure C.1: forced responses with the symmetric

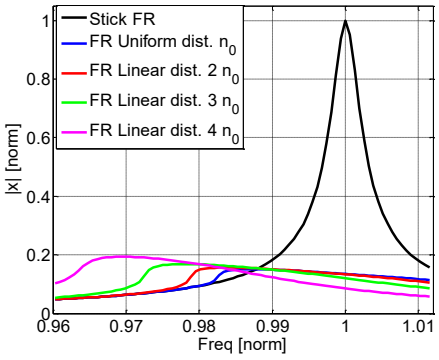


Figure C.2: forced responses with the

linear distributions asymmetric linear distributions

Both Figure C.1 and C.2 show that the uniform distribution represents the optimal condition to reduce the amplitude of vibration of the system. This involves that a variation of the distribution of the normal pre-load produces an increase of amplitude vibration. Figures C.3 and C.4 show instead the damped forced response of the bladed disk where the uniform distribution produces a response of the system out of the optimal condition (blue line). This response has been obtained considering a mean value of the normal distribution four times bigger than the mean value used in Figure C.1 (or C.2). From the uniform distribution, six linear distribution (three symmetric and three asymmetric) has been calculated with the same gradients of Figure 5.71 and 5.72 and then applied to calculated the damped forced responses. The obtained results are very interesting and show a reduction of the resonance frequency by increasing the gradient of the linear distribution. This is due to a reduction of stiffening effect of the contact elements that has a benevolent effect on the resonance frequency.

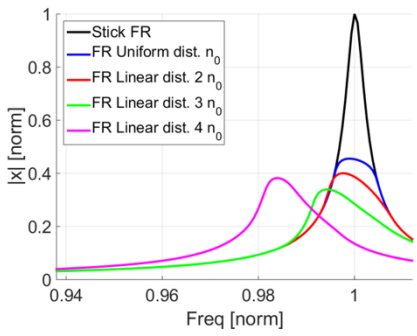


Figure C.3: off-optimal forced responses with the symmetric linear distributions

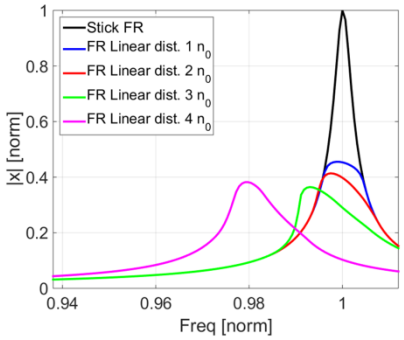


Figure C.4: off-optimal forced responses with the asymmetric linear distributions

# References

[1] A.R. Collar. The expanding domain of aeroelasticity. The Royal Aeronautical Society, pages 613{636, 1946.

[2]Petrov E.P., Ewins D.J. (2004). “State-of-the-art dynamic analysis for non-linear gas turbine structures”, J Aerospace Eng. In: Proceedings of the IMechE, Part G, vol 218, pp 199-211

[3]Ewins D.J. (2010). “Control of vibration and resonance in aero engines and rotating machinery – An overview”, International Journal of Pressure Vessels and Piping, vol 87, pp 504-510

[4] W. Campbell. The protection of steam turbine disc wheels from axial vibrations. Transactions of the ASME, (23), 1924. New York, USA.

[5] W. Campbell. Tangential vibration of steam turbine buckets. Transactions of the ASME, (33), 1925. New York, USA.

[6] A.I. Sayma, M. Vahdati, and M. Imregun. Turbine forced response prediction using an integrated non-linear analysis. Proc Instn Mech Engrs, 214, 2000. Part K.

[7] M.B. Giles. Calculation of unsteady wake/rotor interaction. AIAA Journal of Propulsion and Power, 4(4):356{362, July/August 1988.

[8] A.M. Cargill. Aspects of the generation of low engine order forced vibration due to non-uniform nozzle guide vanes. Rolls-Royce plc, Report No. TSG0602, 1992.

[9] A.I. Sayma. Low engine order excitation mechanisms in turbine blades. VUTC/C/97023, 1997.

[10] T.H. Fransson. Basic introduction to aeroelasticity. VKI LS on Aeroelasticity in Axial Flow Turbomachines (1999).

[11] E.H. Dowel, H.C.Jr. Curtiss, R.H. Scanlan, and F. Sisto. A modern course on aeroelasticity (second ed.). Kluwer Academic Publishers.

[12] J.A. Ekaterinaris and M.F. Platzer. Progress in the analysis of blade stall °utter. Unsteady Aerodynamics and Aeroelasticity of Turbomachines, pages 287-302, 1995. edited by Y.Tanida and M.Namba, Elsevier, Amsterdam.

[13] A.V. Srinivasan. Flutter and Resonant Vibration Characteristics of Engine Blades. IGTI Scholar Paper, Journal of Engineering for Gas Turbines and Power (1997), Vol. 119, 741-775.

[14] M.F. Platzer and F.O. Carta edited in 1988 by AGARD, "Manual on Aero-elasticity in Axial-Flow turbomachines, Vol. 2 – Structural dynamics and aero-elasticity"

[15] Kielb, R.E. and Kaza, K.R.V., 1984, "Effects of Structural Coupling on Mistuned Cascade Flutter and Response", Trans. ASME J. Eng. Gas Turbines and Power, Vol. 106, pp. 17-24

[16] Hoyniak, D. and Fleeter, S., 1986, "The effect of circumferential aerodynamic detuning on coupled bending-torsional unstalled supersonic flutter", Trans. ASME: J. of Turbomachinery, Vol.108, pp.253-260

[17] Martel, C., Corral, R. and Llorens, J.M., 2008, "Stability increase of aerodynamically unstable rotors using intentional mistuning" Trans. ASME: J. for Turbomachinery, Vol.130, 011006-1-011006-10

[18] Marshall, J. and Imregun, M., 1996, "A review of aeroelasticity methods with emphasis on turbomachinery applications", Journal of Fluids and Structures, Vol:10, Pages:237-267

[19] Srinivasan, A., 1997, ''Flutter and Resonant Vibration Characteristics of Engine Blades,'' ASME J. Eng. Gas Turbines Power, 119, pp. 742–775.

[20] Hall, K., Kielb, R., Ekici, K. and Thomas, J., 2005, "Recent advancements in turbomachinery aeroelastic analysis" , Proc. 43rd AIAA Aerospace Sciences Meeting and Exhibit, Reno, Nevada, AIAA 2055-0014

[21] Sayma, A., Vahdati, M., Green, J. and Imregun, M., 1998, "Whole-assembly flutter analysis of a low-pressure turbine blade", Aeronautical Journal, v.102, pp. 459-463

[22] Nowinski, M. and Panovsky, J., 2000, “Flutter Mechanisms in Low Pressure Turbine Blades,” Journal of Engineering for Gas Turbines and Power, Vol. 122, pp. 89–98

[23] Vahdati, M., Simpson, J. and Imregun, M., 2009, “Mechanisms for wide-chord fan blade flutter” Proc. Of ASME Turbo Expo, Orlando, USA, GT2009-60098

[24] Rice, T., Bell, D. and Singh, G., 2009, “Identification of the stability margin between safe operation and the onset of blade flutter”, Trans. ASME: J. of Turbomachinery, Vol.131, pp.011009-1-011011-10

[25] Verdon, J., 1987. “Linearized unsteady aerodynamic theory”. In AGARD Manual on Aeroelasticity in Axial Flow in Turbomachines, AGARD-AG-298.

[26] Whitehead, D., 1987. “Classical two-dimensionnal methods”. In AGARD Manual on Aeroelasticity in Axial Flow in Turbomachines, AGARD-AG-298.

[27] Hall, K. & Clark, W. Linearized Euler predictions of unsteady aerodynamic loads in cascades. AIAA Journal 31, 540–550 (1993).

[28] Hall, K. & Lorence, C. Calculation of three-dimensional unsteady flows in turbomachinery using the linearized harmonic Euler equations. Transactions of the ASME, Journal of turbomachinery 115, 800–809 (1993).

[29] Arnone, A., Poli, F. & Schipani, C. A method to assess flutter stability of complex modes. In 10th International Symposium on Unsteady Aerodynamics, Aeroacoustics and Aeroelasticity of Turbomachines (ISUAAAT) (2003). September 7–11, Durham, NC, USA.

[30] Poli, F., Gambini, E., Arnone, A. & Schipani, C. A 3D time-linearized method for turbomachinery blade flutter analysis. In 11th International Symposium on Unsteady Aerodynamics, Aeroacoustics and Aeroelasticity of Turbomachines (ISUAAAT) (2006). September 4–8, Moscow, Russia.

[31] Corral, R., Escribano, A., Gisbert, F., Serrano, A., and Vasco, C., “Validation of a Linear Multigrid Accelerated Unstructured Navier-Stokes Solver for the Computation of Turbine Blades on Hybrid Grids,” AIAA Paper 2003-

3326, 9th AIAA/CEAS Aeroacoustics Conference, Hilton Mead, South Carolina, May 2003

[32] K.C. Hall, J.P. Thomas, W.S. Clark, 'Computation of unsteady nonlinear flows in cascades using a harmonic balance tecnique', AIAA Journal, Vol. 40, No. 5,May 2002

[33] C. Frey and H.-P. Kersken, "A hybrid mesh linear harmonic solver for the aeroelastic analysis of turbomachinery," in 6th European Conference on Computational Fluid Dynamics (ECFD VI), 2014.

[34] G. Ashcroft, C. Frey, and H.-P. Kersken, "On the development of a harmonic balance method for aeroelastic analysis," in 6th European Conference on Computational Fluid Dynamics (ECFD VI), 2014.

[35] McBean, I., Liu, F., Hourigan, K. & Thompson, M. Simulations of aeroelasticity in an annular cascade using a parallel 3-dimensional Navier-Stokes solver. In IGTI ASME Turbo Expo (2002). June 3–6, Amsterdam, The Netherlands, ASME paper GT2002-30366.

[36] F. Poli, L. Pinelli, A. Arnone, 'Aeroelastic stability analysis of a non rotating annular turbne test rig: a comparison between a linearized and non-linear computational method', The 22° International Congress on Sound nad Vibration, Florence, Italy, 12-16 July 2015

[37] Chassaing, J. & Gerolymos, G. Compressor flutter analysis using time-nonlinear and time-linearized 3-d navier-stokes methods. In 9th International Symposium on Unsteady Aerodynamics, Aeroacoustics and Aeroelasticity of Turbomachines (ISUAAAT) (2000). September 4–8, Lyon, France.

[38] Cinnella, P. & Palma, P. D. A numerical method for turbomachinery aeroelasticity. Transactions of the ASME, Journal of turbomachinery 126, 310–316 (2004).

[39] Pinelli, L., Poli, F., Arnone, A. & Schipani, C. A time-accurate 3D method for turbomachinery blade flutter analysis. In 12th International Symposium on Unsteady Aerodynamics, Aeroacoustics and Aeroelasticity of Turbomachines (ISUAAAT) (2009). September 1–4, London, UK, paper I12-S8-3.

[40] Corral, R., Crespo, J., and Gisbert, F., “Parallel Multigrid Unstructured Method for the Solution of the Navier-Stokes Equations,” AIAA Paper 2004-0761, 42nd AIAA Aerospace Sciences Meeting and Exhibit, Reno, Nevada, January 2004.

[41] Carstens, Kemme, Schmitt, ‘Coupled simulation of flow-structure interaction in turbomachinery’, Aerospace Science and Technology 7 (2003) 298–306

[42] Sadeghi, Liuy, ‘Coupled fluid-structure simulation for turbomachinery blade rows’, 43rd AIAA Aerospace Sciences Meeting and Exhibit, 10 - 13 Jan 2005, Reno, NV

[43] Whitehead D.S., “Effect of Mistuning on the Vibration of Turbomachine Blades Induced by Wakes”, in Journal of Mechanical Engineering Science, v. 8, n. 1, p. 15-21, 1966.

[44] Ewins D.J., “The Effect of Detuning Upon the Forced Vibration of Bladed Disk”, in Journal of Sound and Vibration, v. 9, n. 1, p. 65-79, 1969.

[45] Feiner D.M., Griffin J.H., “Mistuning Identification of Bladed Disks Using a Fundamental Mistuning Model – Part I, Part II”, in Proceedings of the ASME TURBO EXPO 2003, 2003-GT-38952, 2003-GT-38953, 2003.

[46] Martel C., Corral R., “Asymptotic Description of Maximum Mistuning Amplification of Bladed Disk Forced Response”, in Journal of Engineering for Gas Turbines and Power, v. 131 / 022506, 2009.

[47] Griffin J.H., Hoosac T.M., “Model Development and Statistical Investigation of Turbine Blade Mistuning”, in ASME Journal of Vibration, Acoustic, Stress and Reliability in Design, v. 106, p. 204-210, 1984.

[48] Sinha A., “Statistics of the Peak Maximum Amplitude of the Forced Response of a Mistuned Bladed Disk”, in Proceedings of the ASME TURBO EXPO 2005, 2005-GT-69070, 2005.

[49] Kielb R.E., Feiner D.M., Miyakozawa T., Griffin J.H., “Flutter of Mistuned Bladed Disk and Blisks with Aerodynamic and FMM Structural Coupling”, in Proceedings of the ASME TURBO EXPO 2004, 2004-GT-54315, 2004.

[50] Martel C., Corral R., Llorens J. M., “Stability Increase of Aerodynamically Unstable Rotors Using Intentional Mistuning”, in Journal of Turbomachinery, v. 130 /011006, 2008.

[51] Kielb, R.E. and Kaza, K.R.V., 1984, “Effects of Structural Coupling on Mistuned Cascade Flutter and Response”, Trans. ASME J. Eng. Gas Turbines and Power, Vol. 106, pp. 17-24

[52] Hoyniak, D. and Fleeter, S., 1986, “The effect of circumferential aerodynamic detuning on coupled bending-torsional unstalled supersonic flutter”, Trans. ASME: J. of Turbomachinery, Vol.108, pp.253-260

[53] Petrov E.P. & Ewins D.J. (2006). “Effects of damping and varying contact area at blade-disc joints in forced response analysis of bladed disk assemblies”, Journal of Turbomachinery, Vol.128, No.2, (April 2006), pp. 403-410, ISSN 0889-504X

[54] Zucca, S. , Firrone, C.M. , Gola, M.M., “Numerical assessment of friction damping at turbine blade root joints by simultaneous calculation of the static and dynamic contact loads”, Nonlinear Dynamics Volume 67, Issue 3, February 2012, Pages 1943-1955.

[55] Petrov E.P. & Ewins D.J. (2003). “Analytical formulation of friction interface elements for analysis of nonlinear multiharmonic vibrations of bladed discs”, Transactions of ASME Journal of Turbomachinery, Vol.125, No.2, (April 2003), pp.364-371, ISSN 0889-504X

[56] Firrone C.M.; Zucca S. & Gola M.M. (2011). “The effect of underplatform dampers on the forced response of bladed disks by a coupled static/dynamic harmonic balance method”, International Journal of Non-Linear Mechanics, Vol.46, No.2, (March 2011), pp.363-375, ISSN 0020-7462

[57] Firrone, C.M. “Measurement of the kinematics of two underplatform dampers with different geometry and comparison with numerical simulation” Journal of Sound and Vibration Volume 323, Issue 1-2, 5 June 2009, Pages 313-333

[58] Sinha, A. and Griffin J., 1983, “Friction damping of flutter in gas turbine engine airfoils”, J. of 544 Aircraft, v.20, No.4, pp.372-376 545

[59] Sinha, A. and Griffin J., 1985, “Effects of friction dampers on aerodynamically unstable rotor 546 stages”, AIAA J., v.23, No.2, pp.262-270

[60] Petrov, E.P., 2011, “Analysis of flutter-induced limit cycle oscillations in gas-turbine structures 551 with friction, gap and other nonlinear contact interfaces”, Proceedings of ASME Turbo Expo 2011, 552 June 6-10, 2011, Vancouver, British Columbia, Canada, GT2011-46188

[61] Corral, Gallardo, ‘A methodology for the vibration amplitude prediction of self-excited rotors based on dimensional analysis’, Proceedings of ASME Turbo Expo 2006: Power for Land, Sea and Air, May 8-11, 2006, Barcelona, Spain

[62] Corral, Martel, ‘Flutter amplitude saturation by nonlinear friction forces: an asymptotic approach’, Proceedings of ASME Turbo Expo 2013: Turbine Technical Conference and Exposition, June 3-7, 2013, San Antonio, Texas, USA

[63] Corral, Gallardo, Ivaturi, ‘Conceptual analysis of the non-linear forced response of aerodynamically unstable bladed-discs’, Proceedings of ASME Turbo Expo 2013: Turbine Technical Conference and Exposition

[64] Corral, Gallardo, ‘Verification of the vibration amplitude prediction of self-excited lpt rotor blades using a fully coupled time-domain non-linear method and experimental data’, Proceedings of ASME Turbo Expo 2008: Power for Land, Sea and Air

[65] Corral, Gallardo, ‘Non-linear dynamics of multi-mode unstable bladed-disks: part i - description of a canonical model and phenomenological results’, Proceedings of ASME Turbo Expo 2011, June 6-10, 2011, Vancouver, British Columbia, Canada

[66] Krack M, Panning-von Scheidt L, Wallaschek, J: On the Interaction of Multiple Traveling Wave 594 Modes in the Flutter Vibrations of Friction-Damped Tuned Bladed Disks 595

[67] Krack M., Salles L., Thouverez F.: Vibration Prediction of Bladed Disks Coupled by Friction 596 Joints

[68] Tran D.M.; “Reduced models of multi-stage cyclic structures using cyclic symmetry reduction and component mode synthesis”, Journal of Sound and Vibration, Volume 333, Issue 21, 13 October 2014, Pages 5443–5463

[69] Guyan R.J., “Reduction of stiffness and mass matrices”, AIAA Journal, Vol. 3 (2), 1965, pp. 380.

[70] Tran D.M., “Component mode synthesis methods using interface modes. Application to structures with cyclic symmetry”, Computers and Structures, Vol. 79, 2001, pp. 209-222

[71] Siewert C., Panning L., Wallaschek J. and Richter C., 2009, “Multi-harmonic forced response analysis of a turbine blading coupled by nonlinear contact forces”, Proceedings of ASME Turbo Expo 2009: Power for Land, Sea and Air, June 8-12, Orlando, Florida, USA

[72] Lavella M., 2016, “Contact Properties and Wear Behaviour of Nickel Based Superalloy René 80” Metals, Vol. 6 (7), 159, ISSN 2075-4701, CODEN: MBSEC7. doi: http://dx.doi.org/10.3390/met6070159

[73] Lavella M., Botto D., Gola M.M., 2013, “Design of a high-precision, flat-on-flat fretting test apparatus with high temperature capability”, WEAR, Vol. 302 pp. 1073–1081, ISSN: 0043-1648, doi: http://dx.doi.org/10.1016/j.wear.2013.01.066

[74] Botto, D. and Lavella, M., 2015, “A numerical method to solve the normal and tangential contact problem of elastic bodies”, Wear, Vol. 330-331, pp. 629-635

[75] Allara, M., 2009, “A model for the characterization of friction contacts in turbine blades”, Journal of Sound and Vibration, Volume 320, Issue 3, Pages 527-544.

[76] Wang, D., Xu, C., 2014, “A tangential stick-slip friction model for rough interface”, Jixie Gongcheng Xuebao/Journal of Mechanical Engineering, Volume 50, Issue 13, Pages 129-134

[77] Cardona, A.; Lerusse, A. and Geradin, M., 1998. “Fast Fourier Nonlinear Vibration Analysis”, Computational Mechanics, Vol.22, No.2, pp. 128-142, ISSN 0178-7675

[78] Griffin J.H., 1980. “Friction damping of resonant stresses in gas turbine engine airfoils”, Journal of Engineering for Power, Vol.102, No.2, pp.329-333, ISSN 0022-0825

[79] Petrov E.P. and Ewins D.J., 2003. “Analytical formulation of friction interface elements for analysis of nonlinear multiharmonic vibrations of bladed discs”, Transactions of ASME Journal of Turbomachinery, Vol.125, No.2, pp.364-371, ISSN 0889-504X

[80] Siewert C., Panning L., Wallaschek J. and Richter C., 2009, “Multi-harmonic forced response analysis of a turbine blading coupled by nonlinear contact forces”, Proceedings of ASME Turbo Expo 2009: Power for Land, Sea and Air, June 8-12, Orlando, Florida, USA

[81] Cameron, T. M. and Griffin, J. H., 1989, “An Alternating Frequency/Time Domain Method for Calculating the Steady-State Response of Nonlinear Systems”, Journal of Applied Mechanics, Vol. 56, pp. 149-154

[82] Poudou, O. and Pierre, C., 2003, “Frequency-Time Domain Methods for the Analysis of Complex Structural Systems with Friction Damping”, Collection of Technical Papers - AIAA / ASME / ASCE / AHS / ASC Structural Dynamics and Materials Conference, Norfolk (USA), Vol. 1, pp. 111-124

[83] Firrone, C.M., 2006, “Dynamics of the underplatform damper for aeronautical turbo engines”, PhD Thesis, April 2006

[84] Kielb R.E., Feiner D.M., Griffin J.H., Miyakozawa T., 2004, “Flutter of Mistuned Bladed Disks and Blisks With Aerodynamic and FMM Structural Coupling”, ASME Turbo Expo: Power for Land, Sea, and Air, Volume 6 pp. 573-579.

[85] Siewert C, Panning L, Schmidt-Fellner A, Kayser A, 2006, “The Estimation of the Contact Stiffness for Directly and Indirectly Coupled Turbine Blading”, ASME Turbo Expo 2006, Volume 5, pp. 841-853

[86] Thomas D.L, 1979, “Dynamics of rotationally periodic structures”, International journal for numerical methods in engineering, Vol. 14, pp. 81-102

[87] Mead D.J., 1973, “A general theory of harmonic wave propagation in linear periodic system with multiple coupling”, Journal of sound and Vibration, Vol. 27, pp. 235-260

[88] Wildheim S.J., 1979, “Excitation of rotationally periodic structures”, Transactions of the ASME, Vol. 46

[89] Wildheim S.J., 1981, “Vibrations of rotating circumferentially periodic structures”, The Quarterly Journal of Mechanics and Applied Mathematics, Vol. 34, Issue 2, pp. 213–229